Contents

1 Introduction **8**

2 Stroboscopic Observational Method **12**
2.1 Chopper System 12
2.2 Stroboscopic Images 16
2.3 Pulsar Timing and Phase-Correction 18
2.4 Pulse Phase Profile 21
2.5 Testing of the Equipment 24

3 Observations and Analysis **29**
3.1 Old Data Results 30
3.2 Data Overview 32
3.3 Periodic Variability Search in the Data with the Lomb Periodogram (Fourier)Method 35
3.4 Cross-Correlations of Pairs of Lomb Periodograms 48
3.5 Periodicity Search by the Epoch-Folding Technique 61
3.6 Does the Pulsar Magnitude Contain Enhanced Noise? 73

4 Conclusion **81**

Bibliography **84**

A Variation of Seeing Over a Night **89**

B L-Statistic Probability Estimation **93**

C Cross-Correlation Functions **95**

D Extended abstract in Slovene (Razširjeni povzetek v slovenščini) **114**
D.1 Uvod 114
D.2 Opazovanja in rezultati 116

D.2.1 Stroboskopska opazovalna metoda 116
D.2.2 Predstavitev in analiza podatkov 120
D.2.3 Rezultati 127
D.3 Zaključek 128

Chapter 1

Introduction

Crab pulsar (PSR(B)0531+21, J0534+2200) is a compact supernova remnant. The parent supernova has appeared in 1054. It was observed and recorded by Chinese and Japanese (Guidoboni 1993 [23]). In modern astronomy, Crab nebula was first observed by J. Bevis in 1731. The association of Crab nebula to the ancient supernova explosion is due to Duyvendak (Lyne&Graham-Smith 1998 [39] and references therein). The suggestion that the prominent star near the Crab nebula center is connected to the nebula, and therefore to the supernova, goes to Baade (Glendenning 1997 [24] and references therein).

Crab pulsar is a young pulsar and has a relatively short pulsation period of about 33ms. Optical pulsations of Crab pulsar were discovered by Wilstrop in 1969 in Cambridge (Glendenning 1997 [24]). Not much earlier, the pulsar was discovered in radio by Staelin&Reifenstein in 1968 at Green Bank (Lyne&Graham-Smith 1998 [39]). Usually, the discovery of optical pulsations is attributed to Cocke, Disney and Taylor (Steward Observatory, Arizona) since the Cambridge observations were analyzed off-line at a later time. Two other American groups also observed it in January 1969, at McDonald Observatory and Kitt Peak Observatory. Later, a new television technique was applied at the 120-inch telescope at the Lick Observatory, showing two exposures made at pulse maximum and minimum. Surprisingly, no further stroboscopic observations are reported in literature.

The majority of pulsars emit at radio frequencies. Crab pulsar is one of the few that can be observed over a wide range of electromagnetic spectrum: from the low-frequency radio waves, through optical, and to the high energy γ rays (Smith 1977 [50]). Pulsar pulses are well known for their regular periodicity and accurate arriving (Lyne et al. 1993 [38]), which make pulsar clocks comparable to the atomic clock standards (Foster 1996 [18]). On the other hand, neutron star's rotation which generates the regular periodicity

of pulses, also exhibits some peculiarities. Among those, *glitches*—sudden accelerations of the pulsar rotation rate—are the most famous (Lyne et al. 1993 [38]).

Since Crab's discovery, a lot of observing time has been devoted to pulsar timing and to the examination of the pulsar flux stability and/or its modulation, particularly in radio (Huguenin et al. 1973 [28]; Helfland&Fowler 1977 [27]; Jones 1988 [29]). Recently, pulsations temporal-stability has been studied at high energies (Ulmer et al 1994 [58]; Agrinier et al. 1990 [1]; Carramiñana et al. 1994 [9]; Thompson et al. 1993 [55]). In optical and IR, the pulse shape of PSR0531+21 has been studied in detail (Nelson et al. 1970 [40]; Smith et al. 1978 [51]; Jones et al. 1980 [29]; Eikenberry et al. 1997 [16]). The reasons for pulsations' modulation can be divided into two groups: the *outer* and the *inner*. The outer appear as a consequence of physical processes which influence the pulses while they travel through the space between the pulsar emission region and the observer. The inner are due to physical processes within the emission region itself or the neutron star's internal characteristics. One of the latter is free precession. One would expect that pulsars—rotating neutron stars—free-precess, just like the Earth does[1]. The Earth is flattened, it has a solid crust and a molten interior (Goldreich 1970 [22]; Pines&Shaham 1974 [42]); roughly, the structure of a neutron star in terms of solid/liquid components is similar. The first estimates of neutron star free-precessional periods (Shaham 1986 [49]) were followed by an extended theoretical work which considered the relations among individual neutron star structure components (solid, fluid, superfluid matter), and the life-time of free precessional movement (Alpar&Ögelman 1987 [3]; Alpar 1989 [4]). The free-precessional motion should damp in about one thousand years (Alpar et al. 1984 [2]). Therefore, young pulsars such as PSR0531+21 are the most promising candidates for the (free) precessional modulation search. The neutron star matter is very dense (typically 10^{18} kg/m^3) and consequently its gravitational field is very strong. Still, in the case of slowly rotating neutron stars,[2] free precession can be considered nonrelativistically (Thorne&Gürsel 1983 [56]). Classical relation for the free-precessional frequency of a flattened spheroid is given by Goldstein (1980 [21]). Considering the pulsar as a droplet of rotating liquid, its flattening can be obtained by Maclaurin formula (Lang 1978 [33]). In this way Crab's free-precessional period is es-

[1]The Earth's free precession is observed, and the estimated value of its free-precessional period (Goldstein 1980 [21]) coincides well with the measured value (Pines&Shaham 1973 [42]).

[2]Criterium $\Omega L/c << 1$, where Ω is the rotational angular frequency, L is the typical stellar dimension ($\backsim$ pulsar radius), and c is the speed of light. For Crab, $\Omega L/c \approx 7.5 \cdot 10^{-3}$.

timated to be about 100 seconds[3]. The free-precessional period depends on neutron star matter (equation of state) which means that measuring of the precessional frequency would narrow down the list of theoretical neutron star models (Lipunov 1992 [37]), and select the most probable equation of state for the neutron star matter.

During the previous years, many observers were trying to explain long-(quasi)periodic modulations of pulsars' energy fluxes. In radio, modulations with periods ranging from 1 to 150 days were reported for several pulsars (Huguenin et al. 1973 [28]; Helfand&Fowler 1977 [27]). For the Crab pulsar, a period of 77 days based on radio observations has been reported (Richards 1970 [47]), while in the high-energy region (observations by satellite telescopes COMPTEL, OSSE, EGRET), periods of more than 10 years have been indicated (Thompson et al. 1993 [55]). However, more recent observations mainly report on constant radio fluxes for a few tens of pulsars (Stindebring 1990 [54]) and (long-term) intensity modulation is commonly explained as due to refractive interstellar scintillations (Gupta et al. 1993 [25]; Stindebring 1990 [54]; LaBrecque et al. 1994 [32]). Also, according to the recent high-energy observations, there are no significant variations of pulsar PSR0531+21 light-output on time-scales from hours to years (Ulmer et al 1994 [58]). γ-ray Crab's pulse shape is temporary stable (analysis of five several days long observations over a two months span; Carramiñana et al. 1994 [9]).

A more detailed literature overview on neutron stars' free-precession, and on observed (quasi)periodic variabilities in pulsars' flux is given in Galičič 1995 [20].

In optical, pulsar PSR0531+21 is a relatively weak object with the average visual magnitude of 16.5 (Kristian 1971 [31]). On time-scales from ten minutes to several hours, its optical pulsations intensity is constant to the level of 5% (Kristian 1971 [31]). Also, its intensity "noise" on time-scales from a nanosecond to 30 microseconds has the statistical nature (Hegyi 1971 [26]). Later, precise observations were mainly aimed towards a detailed study of the pulse shape and the shape's temporal stability (Smith et al. 1978 [51]; Jones

[3]This estimate, along with the relevant literature overview, is given in Galičič 1995 [20]. Briefly, it is obtained using the relation $\Omega_p = \frac{J_3 - J_1}{J_1}\Omega$, where Ω_p is the free-precessional angular frequency, Ω is neutron star rotational angular frequency, and J_3, J_1 are inertial moments of the star along and perpendicular to the axis of rotation. The ratio $\frac{J_3}{J_1}$ can be obtained from the stellar flattening $e = \sqrt{1 - (\frac{J_3}{J_1})}$, which is obtained from the Maclaurin formula (Lang 1978 [33]). For rotators satisfying the condition $\Omega < \sqrt{2\pi G\rho}$, where G is gravitational constant and ρ is the neutron star matter density, Maclaurin formula can be simplified into the expression $\frac{\Omega^2}{2\pi G\rho} = \frac{4}{15}e^2$.

et al. 1980 [29]). An overview of the literature shows that Crab's optical pulsations have not been particularly observed in order to search for minute time-scales variations. Our stroboscopic system (stroboscope–a metal wheel with radial out-cuts; CCD camera; reference clock) seems to be, according to our knowledge, the first apparatus constructed for this purpose. It is a CCD based, and not a (high-speed) photometer based device as one might have expected. CCD cameras can not be compared to (high-speed) photometers as far as time resolution is concerned, but they do have several other advantages, e.g. they are very appropriate for Earth-based observations since other field stars enable to calibrate stellar magnitude for atmospheric variations.

The previous analyses of observations obtained by the stroboscopic system and the 1.82m Italian telescope in 1994 and 1995, and observations obtained by the fast photometer aboard Hubble Space Telescope in 1991, consistently show the presence of a weak periodic modulation of Crab pulsar's optical pulsations. Its period is 60 seconds, and its amplitude is 0.0065 magnitude (Galičič 1995 [20]). Our idea was, first, to obtain new data with higher signal-to-noise ratio, to confirm the modulation with a higher degree of probability (in analysis described in Galičič 1995 [20], the 60s-periodicity signal-to-noise ratio was ≈ 3). Second, we were tempted to show that this periodicity could be explained as a free-precessional motion (Čadež and Galičič 1996 [11], Čadež and Galičič 1996 [12]). The crucial argument would be the continuous temporal changing of the measured period value, and its possible regular dependence on pulsar rotational period.

In the second chapter of the thesis, the stroboscopic observing method and the evolution of the stroboscopic system for optical observation of pulsars is described. In the third chapter, the pulsar PSR0531+21 observations obtained during the last few years by the stroboscopic system and the 1.82m and 1.22m telescopes of the Asiago observatory in Italy, and by the 2.12m telescope of the Mexican observatory "Guillermo Haro" in Cananea are presented and analyzed. Each data set is searched for possible periodicities, and the statistical significances of indicated periodicities are assesed. The fourth chapter sums up the thesis achievements, and suggests further possibilities to apply the stroboscopic observational method in pulsar astronomy. In Appendices A and B, a discussion of seeing over the observing night, and L-statistic probability estimation are given, respectively. In Appendix C, cross-correlation graphs are shown, and in Apendix D, the extended abstract in Slovene language is given.

Chapter 2

Stroboscopic Observational Method

In this chapter, stroboscopic observational set-up, and in particular its fundamental part, the chopper, are described. Advantages of stroboscopic observation of Crab pulsar compared to an observation without a chopper are presented. Two stroboscopic images are shown, the first one displaying Crab pulsar at its maximum brightness, and the second one showing it when pulsations are "switched off" by the chopper. Pulsar timing is briefly introduced, and the reasons for changing of pulsar frequency measured at an observatory are given. The procedure which we use to compensate for the pulsar frequency changing is described. The term pulse phase profile is introduced, and the measured Crab pulse phase profile is compared to its simulated counterpart. Finally, testings of stroboscopic devices timing accuracy are presented along with their results.

2.1 Chopper System

The stroboscopic (television) technique was used in 1968 when Crab pulsar was first detected in optical (Lyne&Graham-Smith 1998 [39]). Nevertheless, according to our knowledge, it was not used for further observations. We thought that the potentials of the method are far from being exhausted, particularly with the advent of CCD cameras. With a CCD camera, we have accurately detected Crab optical pulsations, measured the pulsar rotational frequency, and searched for a possible pulsations modulation.

In 1991, we made the first simple chopper which enabled us to measure the Crab pulsar frequency with the relative accuracy of $6 \cdot 10^{-6}$ (Galičič 1991 [19]). A small stroboscopic wheel was run with an electro-motor pulsed by a

pulse generator. The 25-cm automatic telescope of the AGO (Astronomical-Geophysical Observatory Golovec, University of Ljubljana) was used for these observations.

In the following years, we redesigned the chopper and were gradually improving the observing system and method. In November 1993, we made the first trial observations at the Italian 1.82m telescope in Asiago with the redesigned chopper. A few very important improvements were made before the December 1994 observation in Asiago. Function Generator HP3325A was externally controlled by the clock HP5342A Counter, to achieve better timing accuracy. We applied for the first time the on-line phase correcting, to account for the Earth rotation Doppler shift, and other effects which influence the value of detected pulsar frequency (see section 2.3). Finally, we used AGO's CCD chip (Wright Instruments Peltier cooled CCD camera EEVP86231 385x578 pixel, thinned, back illuminated, quantum efficiency 65% [10]), which has a user friendly manipulating software, which, for example, enables to take a set of consecutive images with equal exposure times. In the autumn of 1995, the clock HP5342A Counter was replaced by a GPS receiver clock.

Currently, the stroboscopic system consists of several devices which are schematically shown in Figure 2.1.

The chopper itself is basically a metal wheel which rotates with a frequency equal to the pulsar's rotational frequency. In fact, the wheel (circular in shape) has four outcuts, as shown in Figure 2.1, of 9^0 at every 90^0, to compensate for the stepper motor limited speed potentials. The 10% width of the outcut corresponds to the width of the Crab's pulse (see Figure 2.4). The metal wheel is mounted in front of the CCD chip so that the light-beam from the telescope is cut before it falls onto the chip in such a way, that the camera is effectively closed for the 90% of the Crab's pulse period. Therefore, photons are collected only during 10% of time during each exposure, that is only during the brightest part of each main pulse.

The chopper wheel is driven by the frequency generator (Hewlett-Packard Function Generator HP3325A) which is externally controlled by a GPS receiver clock (TrueTime, model XL-DC 151-600-110)[1]. To achieve its specified accuracy, we switch the GPS Receiver and HP3325A on one day before the observation starts, and leave them running during all the consecutive days of observation. To compensate for pulsar frequency changes, stroboscope rotational phase angle is automatically changed in appropriate time inter-

[1]XL-DC timing and frequency specifications are: Frequency Output Accuracy $< 3 \cdot 10^{-12}$; Frequency/Timing Stability: $3 \cdot 10^{-10}$ @ 100 sec, $3 \cdot 10^{-12}$ @ 1 day. Oscillator stability: $2 \cdot 10^{-6}$ over 0^0C to 50^0C when not tracking satellites [57].

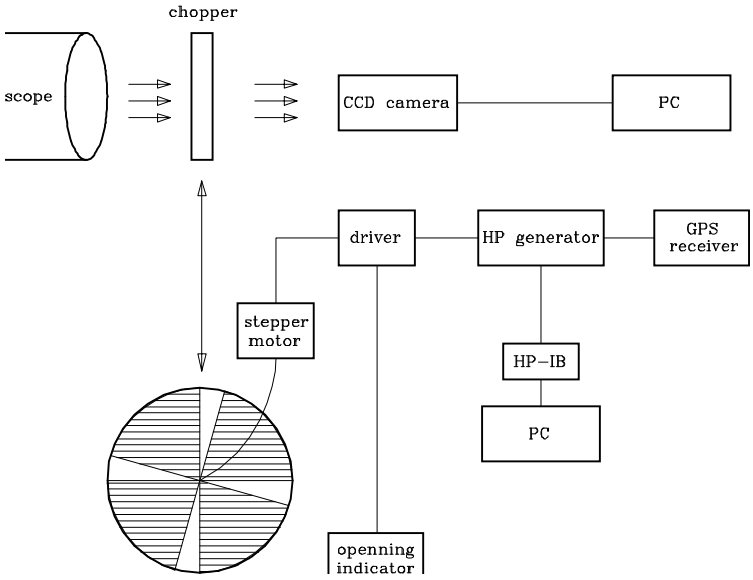

Figure 2.1: The schematic drawing of the state-of-art stroboscopic observational set-up. Before the light beam from the telescope falls onto the CCD chip, it is cut by the rotating chopper wheel. The chopper wheel is run by a stepper motor. Its electronics (driver) is pulsed by a function generator (Hewlett-Packard HP3325A) which is stabilized by a GPS clock (True Time GPS Receiver). Phase corrections (see text and section 2.3) are introduced with a computer (PC) via the HP-IB interface. CCD images are stored on the hard disc of another computer (PC). The opening indicator enables us to electronically stop the chopper wheel in such a position that its opening is centered over the center of the CCD chip.

vals with a PC computer and the interface HP-IB. (A detailed description is given below in section 2.3). The corrections are calculated beforehand by the adapted computer program Bartim which is also described in section 2.3.

The main advantages of the stroboscopic method of observation are:

1. By using such a method, we can actually *see* the pulsations.

When chopper rotates with pulsar's frequency, we can "switch" the pulsar "on" or "off" by changing the chopper phase angle (see Figures 2.2 and 2.3). This is a method which can successfully be used for identification of the pulsar among stars in the telescope's field of view.

2. It enables us to observe possible amplitude and phase modulation of pulsations.

Sensitivity to phase and amplitude modulation depends on the phase between the chopper and the pulsar. The amplitude modulation sensitivity is highest on the main peak, while the phase modulation sensitivity is highest on the steepest part of the main peak intensity curve. In every observation, we tried to observe with such a chopper-pulsar phase difference that pulsar was the brightest, which means that we covered the main peak with the chopper window.

3. Pulsar signal is enhanced compared to the surrounding background.

The shape of the chopper wheel enables us to collect photons only during the 10% of each pulse period when the pulse intensity is greatest. This means that during the remaining 90% of each pulse period we also do not collect the background (sky) photons. In this way, the signal-to-noise ratio is improved as compared to a direct observation (without a chopper). The most important issue introduced by such an observing method in the case of Crab pulsar is the enhancement of pulsar's signal as compared to the background noise which is generated by the Crab nebula. In stroboscopic observations, also the nebula photons are collected during only 10% of time while in a non-stroboscopic observation, background photons are counted continuously, that is also during the major part of the pulse where pulsations intensity is smaller than over the main pulse region, or even equals zero.

Consider the following example. The signal to noise ratio for a star in a CCD image can be estimated with the formula (see also Stetson 1994 [52] and Galičič 1995 [20])

$$\frac{S}{N} = \frac{zP}{\sqrt{((z+2n)+(rn^2))P}} \tag{2.1}$$

where zP is the number of star's photons, P is the number of pixels covered by the stellar profile, n is a typical sky value per pixel, and rn is the read-out-

noise per pixel. In a typical image from 1995 observation in Asiago, pulsar's signal to noise ratio according to eq. (2.1) is $\frac{S}{N} = 90$. If we take in account that chopper is opened for 10% of time, we may estimate that without a chopper, n would be 10 times larger than it is on the considered CCD image. With this new value for n, and other variables from eq. (2.1) held fixed, the estimate for the signal-to-noise ratio for an observation without the chopper is 40. Comparing the two $\frac{S}{N}$'s, we can see that in an observation with the chopper, the pulsar signal-to-noise ratio on a CCD image is about 2.2-times larger than in an observation without the chopper.

More details on the stroboscopic observing system method, and on the observing set-up components, are given in Galičič 1995 [20].

2.2 Stroboscopic Images

Figure 2.2 shows an image with pulsar "on" which means that chopper's frequency is equal to the pulsar's frequency, and the chopper-pulsar phase difference is zero. Pulsar is the brightest star in the upper right corner of the Figure. Next to it, a bit downwards and to the right, is a star we call the next-to-pulsar star. The bright star at the bottom of the Figure is the second brightest star in the image. In Figure 2.3, pulsar is "off". Comparing the position of the next-to-pulsar star, the second brightest star, and the triangle of the feeble stars on the left side of the image in both Figures, we can note the absence of pulsar in the upper right corner of the second image. Images shown in Figure 2.2 and 2.3 were taken on 23/24 January 1998 with the 2.12m telescope in Cananea. Exposure time was 30 seconds.

In both images, we can see a similar pattern of greyish background—the so called *sky*, which is not as flat as it should have been in an average stellar field. This is due to the fact that pulsar is surrounded by the patchy Crab nebula whose surface brightness differs from point to point.

Here we can illustrate point **3.** of the previous section in another way. We compare the pulsar brightness to the next-to-pulsar star's brightness. Without a chopper, Crab pulsar is 0.5 magnitude fainter than the star next to it (V_{Crab}=16.5, V_{star}=16.0, Burnham 1987 [8]). In an image taken with a chopper, as the one shown in Figure 2.2, pulsar is almost a magnitude (0.9 magnitude) brighter than the star next to it.

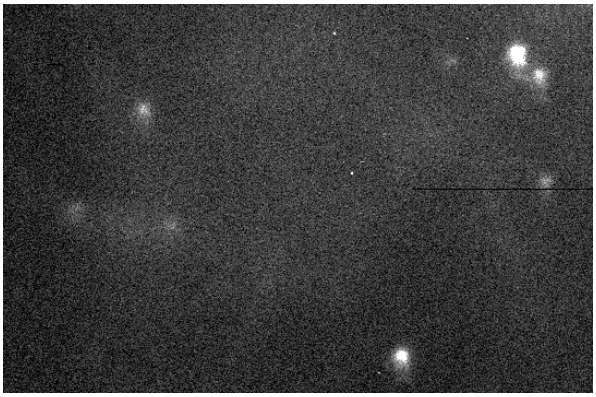

Figure 2.2: Pulsar is "on" (the brightest star in the Figure, upper right corner). The image was taken on 23/24 January 1998 in Cananea. Exposure time was 30 seconds. The image size is 1.8' x 1.2'.

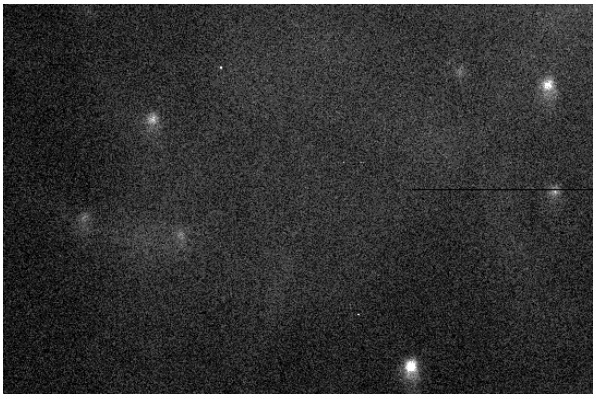

Figure 2.3: Pulsar is "off" (compare the upper right corner of the Figure with Figure 2.2). The image was taken on 23/24 January 1998 in Cananea. Exposure time was 30 seconds. The image size is 1.8' x 1.2'.

2.3 Pulsar Timing and Phase-Correction

The clock we use at pulsar observations must be extremely precise in order to match the precise pulsar's internal clock based on its rotation. To follow pulsar frequency by the stroboscope, all the phenomena that influence pulsar frequency must be taken in account. Those phenomena include: Earth's rotation around the Sun and Earth's rotation about its body axis (Doppler shifts $\sim 10^{-4}$ and $\sim 10^{-6}$, respectively); pulsar slowdown which is described by a time series for the period P (or frequency ν) at any instant of time t if we know its value P_0 at an earlier instant t_0, $P(t) = P_0 + \dot{P}(t-t_0) + \frac{1}{2}\ddot{P}(t-t_0)^2 + ...$, where $\dot{P}$ and $\ddot{P}$ are the period's first and second time derivatives, respectively ($\dot{\nu} = 36ns/day$, so that in every hour, pulsar's period lengthens for 1.5ns); and the relativistic delay of light in the solar gravitational field (Bell 1997 [5]). During the stroboscopic observation, the pulsar frequency changing due to the above listed phenomena is compensated by a computer-run introduction of small phase shifts to the chopper. We call this on-line procedure the *phase-correction*. The procedure is described in the second paragraph below.

First we will briefly explain the need and principles of pulsar timing. Pulsar timing measurements are mainly done at radio frequencies. That is understandable since the majority of pulsars were discovered, and are observed at radio frequencies. With the very first pulsar observations, it was realized that the arrivals of individual pulses depend on several factors. A subscience developed in pulsar astronomy, *pulsar timing*, which deals with accurate measurement and prediction of pulse arrival times with respect to Earth observatories. To predict those with high accuracy, extended observations are required. For example, the Crab pulsar is regularly observed at Jodrell Bank, which provides Crab's Monthly Ephemeris. They include the Crab's rotational frequency ν at 00UT on the 15^{th} of each month, as well as the first frequency derivative $\dot{\nu}$ (the second derivative can be calculated with ν and $\dot{\nu}$), and a few other pulsar parameters. The reference values are given for the solar system barycentre. Pulsar timing not only serves as a tool to obtain pulsar rotation parameters, but can also provide the value of pulsar distance, and some characteristics of the interstellar medium in direction to the pulsar. For the phase-correction procedure, we get the reference values of ν and $\dot{\nu}$ from the Jodrell Bank Crab Pulsar Ephemeris (Lyne et al. 1994-1997 [17]). Observations of the Crab pulsar at different wavelengths show that the pulse shape is very much alike at any frequency, and the period is the same (Smith 1977 [50], Lyne 1998 [39]). IR timing observations have shown that near-to-optical timing results (J, H and K IR bands) agree with the radio timing results over the same time span within the measuring uncertainties (Eikenberry et al. 1997 [16]). We therefore believe that the radio measured

reference values are suitable for our purposes.

By the term phase-correction, we denote the procedure composed of two parts. First, we calculate the pulsar frequency at a certain moment with respect to the observatory, using the solar system barycentre values. We set the chopper frequency to this calculated value. Second, we compensate the change of observatory pulsar frequency value at a later instant of time by a phase shift, fed to chopper (through HP3325A and HP82335 HP-IB) via computer. In this way, we want to keep the starting chosen phase diference between the chopper and the pulsar constant during the whole observation. For the calculation of phase shifts, a standard pulsar observers' computer program Bartim is used. We got a copy of the fortran routine in 1993 from our colleagues (G. Fazio and S. Eikenberry, private communication). This MIT code (original: D. Richards, 1970; improvements: J. F. Chandler, 1984) is based on MIT Lunar and Planetary Ephemeris PEP740X (covering Julian Date 2440001 to 2451181). Its input datum is the time of arrival of a certain pulse to solar system barycentre, and its output is the time of arrival of this pulse to an observatory on the Earth. We translated the original fortran program into pascal and adapted it to our specific demands, so that its input data are the planned observation's beginning and end time, and its output is the starting chopper frequency, and a file of phase corrections (e.g. calculated at every 10s) for the planned duration of the observation. For every observation, phase corrections are calculated in advance and saved to a file. This file is read during the observation by an IBASIC routine, which communicates with HP3325A through HP-IB, so that the chopper phase is corrected at every instant of time for which the correction is written in the file.

The phase-correction procedure was applied for the first time in December 1994 observations. We set the chopper frequency to the value calculated by Bartim and manually adjusted the desired chopper-pulsar phase difference (close to 0, so that pulsar was very bright). Inspite of running of phase-correction, we lost the starting pulsar-chopper phase difference in 3/4 of an hour. We designate such an interval of time in which we lost the desired phase difference by t_E. We stopped the observation and manually changed the chopper frequency for the measured amount $\Delta\nu_m$, which we obtained in the following way. We manually introduced such a phase shift $\Delta\phi$ to the chopper that pulsar become equally bright as it had been at the beginning of the observation, this is before time t_E. Then we calculated the necessary chopper frequency change $\Delta\nu_m$ as $\Delta\nu_m = \frac{\Delta\phi}{2\pi t_E}$. After we had set the starting chopper frequency in this way, we switched on the phase-correction and the almost constant pulsar-chopper phase difference was kept for the next two

hours[2]. In this time interval, the pulsar magnitude change was $\frac{\Delta m}{\Delta t} = 5.5 \cdot 10^{-5} mag/s$, or expressed as the temporal phase-drifting, approximately $\frac{\Delta \Phi}{\Delta t} = 5.9 \cdot 10^{-4\,0}/s$. We saw a possible cause for the starting discrepancy between the two frequencies in vibrations to which the reference clock crystal was exposed during the car transportation from Ljubljana to Asiago.

Our next observation in December 1995 used the GPS Receiver clock instead of the previousely used Counter. Again, after some time observing, like at the 1994 observation, we had to introduce a manual correction to the starting chopper frequency, calculated by Bartim. After that, the chopper-pulsar phase-difference was kept constant for 2.2 hours[3]. The pulsar magnitude changing with time was 20 times better than a year ago: $\frac{\Delta m}{\Delta t} = 2.5 \cdot 10^{-6} mag/s$, or approximately $\frac{\Delta \Phi}{\Delta t} = 2.7 \cdot 10^{-5\,0}/s$. When we analyzed the possible reasons for the starting discrepancy of pulsar and chopper frequencies afterwards, we found an error in the Crab Ephemeris. The reference Julian Date for August 15, 1995 was 2449934 instead of the correct value 2449944. The difference in Doppler frequency shifts corresponding to both Julian dates is of the same magnitude as the manual correction we had to introduce at the beginning of this observation. We, therefore, believed to have solved the problem, and that our phase-correction procedure worked properly.

Unfortunately, problems with the correct chopper frequency calculation remained through the December 1996 and February 1997 observation. Before the December 1997 observation, Bartim was carefully examined but we did not find any inaccuracies or 'bugs' that could have caused the problems with incorrect frequency calculation. The problems went on to observations December 1997, and January 1998. After we had manually corrected the chopper frequency and switch on the phase correction, the starting phase-difference was lost in 0.5 to 2 hours. Whenever we observed this (pulsar was getting fainter in comparison to the star next to it), we stopped the observation, manually corrected the chopper frequency by the measured amount, and started the observation again. In a night with favourable weather conditions, this repeated a few times. For that reason, the pulsar magnitude curves of the last two groups of observations are cut into short pieces (see Figure 3.3).

Luckily, the phase-losing problem seems to be solved at the latest Crab stroboscopic observations in Mexico (A. Čadež, A. Carramiñana, T. Zwitter; Cananea December 1998) with an introduction of a 0.5 Julian Date in the pulsar frequency calculation procedure of program Bartim.

[2] We then had to stop the observation because the weather has worsened.

[3] As long as the weather conditions allowed us to observe.

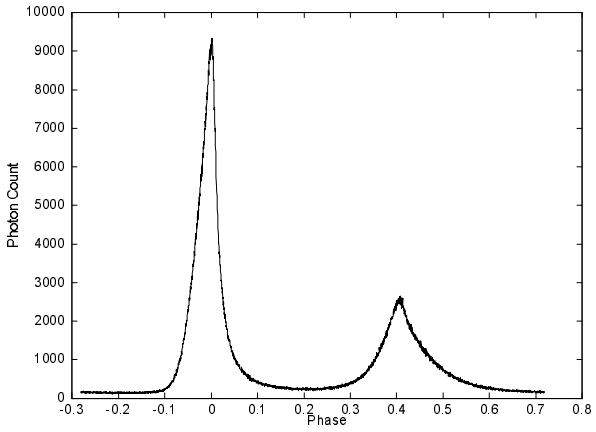

Figure 2.4: The optical pulse profile of Crab pulsar, obtained as an average of approximately two hours of observations with the high speed photometer (V filter) of the Hubble Space Telescope in October 1991 (Percival et al. 1993 [41]).

2.4 Pulse Phase Profile

We define the *pulse phase profile* as a curve which shows the change in the pulsar's magnitude according to the phase difference between the chopper and the pulsar when the two rotate with the same angular frequency. We say that the phase difference equals zero when pulsar is brightest. This means that the chopper outcut covers the brightest 10% of Crab's main pulse.

The ratio between the chopper opening and its closed part was chosen according to the actual Crab pulsar pulse shape which is well known. In Figure 2.4, Crab's pulse profile measured by the Hubble Space Telescope (Percival et al. 1993 [41]) is shown. The Crab's pulse has a distinctive main peak, and a lower and wider secondary peak. They are $0.42 \cdot 2\pi$ appart. We will designate the discrete function shown in Figure 2.4 as $p(\phi_i)$, where ϕ_i is the phase angle in degrees of arc, or in fractions of 2π as labelled on the x axis in Figures 2.4 and 2.5. Phase zero in Figure 2.4 corresponds to the maximum of the main peak. Individual points of the measured curve $p(\phi_i)$ are separated by 0.115^o.

The chopper transmission function is a simple window function $w(\phi_i)$ shown schematically in Figure 2.5. The chopper window is opened for 10% of the period (value "1" in Figure 2.5) and closed for the remaining 90%. Knowing both $p(\phi_i)$ and $w(\phi_i)$, one can calculate the expected shape of the (pulse) phase profile by convolving the two functions[4]. By letting the window

[4]Further on in this section, we call this curve the calculated phase profile, but the word

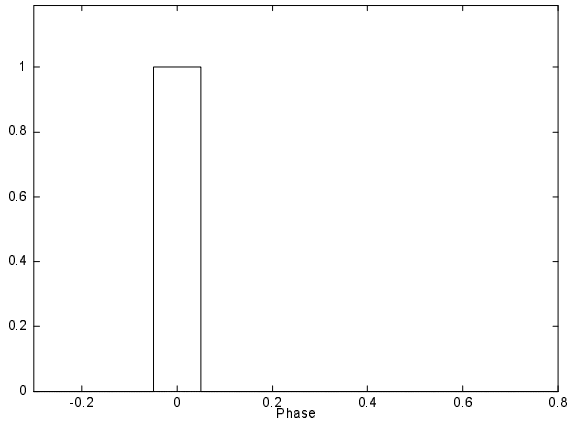

Figure 2.5: The chopper window function. Here, the 10% of the chopper wheel outcut is represented by the value "1", while the remaining 90% of the period when chopper blade closes the light-beam path to the CCD camera is represented by the value "0".

$w(\phi_i)$ slide by one point in $p(\phi_i)$ in every step, the pulse signal was summed over the window opening at each step. The result, $\int_0^{2\pi} p(\phi')w(\phi - \phi')d\phi'$, is shown as a continuous curve in Figure 2.6. One can note that the pulsar is about 0.9 magnitude brighter when the window covers the main peak (the two deepest minima in Figure 2.6) than when it covers the secondary peak (local minimum between the two deepest minima). The phase difference between the two deepest minima in the Figure corresponds to a full cycle, i.e. 2π.

In practice, phase profile can be measured with a set of images where two consecutive images differ by a certain amount in chopper-pulsar phase difference. We obtained a full phase profile in Cananea in the night 23/24 January 1998. It is shown in Figure 2.6 with errorbarred diamond dots. The measurement lasted 45 minutes while individual images are 40 seconds apart, and the exposure time of each image is 30 seconds. The main-peak part of the phase profile was again scanned twice in the night 24/25 January 1998.This measurement is shown with squares in Figure 2.6. The magnitude of the next-to-pulsar star is shown with crosses. We can notice here[5], that the errorbars calculated by Daophot, according to eq. (2.1), σ_D, are obviousely too short to account for the star's magnitude statistical variation σ_{stat}. The ratio of both variances for this star, σ_{stat}/σ_D, is almost 3. Therefore, the

'calculated' refers here only to the mathematical procedure (convolution) by which we obtained it from the two discrete curves shown in Figures 2.4 and 2.5.

[5]We can observe this for all the other stars in all observations, see also section 3.6.

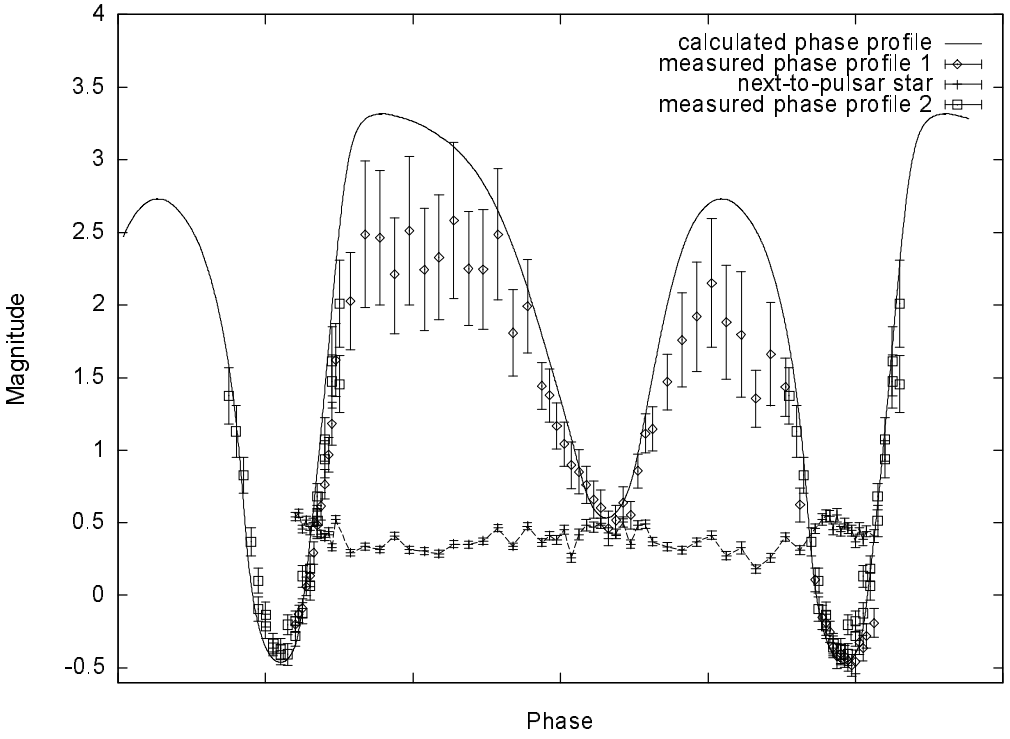

Figure 2.6: Calculated (continuous line) and measured (diamond dots) Crab's pulse phase profile (see the legend in the upper right corner of the Figure). The phase in the calculated phase profile goes backwards with respect to the Crab optical pulse profile shown in Figure 2.4, to match the measured phase profile. Crab's phase profile was measured on 23/24 January 1998. Additionally, the main peak was scanned twice on 24/25 January. This measurement (squares) is attached over both of the phase profile minima (note that the magnitude is labelled on the y-axis, therefore the curve minimum corresponds to the Crab pulse main peak).The next-to-pulsar star magnitude is also shown (see the Figure legend). The phase difference between the two deepest minima in the Figure, or the main peak to main peak phase difference, corresponds to a full cycle, i.e. 2π.

plotted errorbars for the pulsar magnitude are correspondingly larger than the calculated values σ_D. Both magnitude maxima (pulse signal minima!) in Figure 2.6 (corresponding to the regions between the main peak and the secondary peak, and between the secondary peak and the main peak) are deeper in the calculated than in the measured curve. This is expected since HST's sky background is darker than its ground-based observations counterpart. On images where the pulsar is effectively "off", the values of its magnitude are close to the sky brightness, so they are almost background noise limits[6]. At the chopper-pulsar zero phase difference, pulsar is almost a magnitude brighter than at the phase difference corresponding to the secondary peak, just the same as can be observed in the calculated curve. We can conclude that within measurement errors, the measured phase profile can be well fitted by the phase profile obtained by convolution of the Crab pulse and the window function.

In the measured phase profile, the phase difference between the consecutive two main peaks (between the two curve's minima in Figure 2.6) was actually larger than 2π. The extra phase difference was due to the Earth motion Doppler shift which was not compensated since the phase correction was switched off during the phase-profile measurement. The calculation of the Doppler shift which has accumulated during the phase profile measurement accounts accurately for the observed excess.

2.5 Testing of the Equipment

The equipment has to be tested for two main reasons. First, in order to measure the system timing accuracy, and second, to check whether some accidental minute time-scale periodicities detected in the pulsar signal might have originated in the equipment. The stroboscopic equipment was tested three times during the last four years of Crab observations.

System clock timing accuracy

The system clock timing accuracy was measured before the 1994 December observation in the laboratory *Hermes Plus*[7] in Ljubljana. The overall

[6] In practice, the number of pulsar's photons is always above the sky value on our CCD images, even when the pulsar should be effectively off. There is no chance that this enhancement is due to the thermal emission of neutron star's surface since the black body brightness of Crab would have magnitude of over 25 (compare also http://oposite.stsci.edu/pubinfo/captions/97-32.txt). A remaining possible explanation is that there may be a brighter nebula knot beyond or very close to the direction to Crab pulsar.

[7] The Hewlett-Packard representative company in Slovenia.

timing accuracy of the system HP 3325A - HP 5342A (timing standard HP Counter that served as a reference clock in 1994 observations) at the frequency $10 MHz$ was 10^{-9} of the selected frequency[8].

Testing the chopper system timing accuracy I

With this testing we intended to determine the chopper system timing accuracy, and to check for the possibility of artificially generated minute time-scale periodicities inside the chopper system. The measurement was again performed at the *Hermes Plus* laboratory after the 1995 December observation. The chopper was run in the same way as during observations, that is with the HP 3325A - GPS Receiver clock. The artificial pulsar was generated with an LED pulsed by another HP 3325A with the HP atomic clock as its timing reference. The LED signal was detected by a photo transistor and recorded with computer via an AD converter. The Fourier spectrum of a measurement which lasted 4000 seconds in shown in Figure 2.7 with the solid line. The peak at period 60s (dotted curve in Figure 2.7) is the Fourier spectrum of a sine signal, generated at the measurement points. The sine period is 60.0s and its amplitude is 0.0001 magnitude. We can see that in the 4000s-measurement, no periodicity was detected around the period 60s at the level of about 10^{-5} magnitude. This is far below the 0.0065-magnitude modulation which we had detected with 1994 and 1995 observations.

For the other test, the chopper's and the artificial pulsar's frequencies were set to values $30 Hz$ and $(30 + 1/40) Hz$, respectively. In the Fourier spectrum of the resulting beating, no other peaks but the one at 40 seconds, and its multiples, are present.

Testing the chopper system timing accuracy II

The third testing was performed in the summer 1998 in our laboratory. The same equipment and software as at the most recent (1996-1998) pulsar observations was used to run the chopper. An artificial pulsar was simulated by an LED which was pulsed by the HP 3335A[9]. The CCD camera system was used to collect the images, and the data reduction was done with the Daophot software, in the same way as the pulsar images were reduced. Three types of tests were carried out.

In the first one, the chopper and the artificial pulsar frequency were set to equal values, 30Hz. Both function generators were externally controlled by the GPS receiver clock. As an example, the Fourier spectrum of a half an hour

[8] See (Galičič 1995 [20]).

[9] The device was kindly lent for a few days of measurements in May and June 1998, by J. Lužnik and J. Pirnat of Prof. Dr. Z. Trontelj's laboratory at the Institute of Mathematics, Physics and Mechanics at Faculty of Mathematics and Physics, University of Ljubljana.

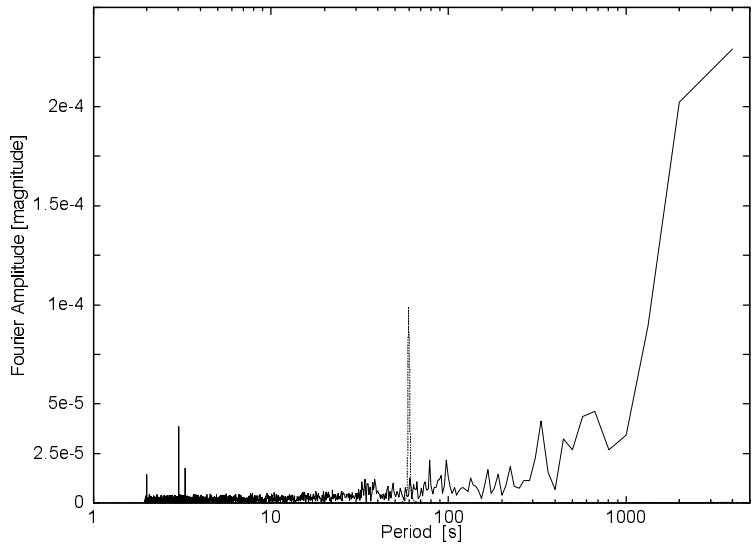

Figure 2.7: Fourier spectra of the 4000s-measurement with equal frequencies of chopper and of artificial pulsar, and of a sine signal with period 60s and amplitude 0.00001 magnitude.

long measurement is shown in Figure 2.8 together with a transform of a sine signal with the amplitude 0.0065-magnitude, at the chosen frequency (dotted curve), which serves for the amplitude calibration. We can see that the highest noise-originating peaks are less than 0.002 magnitude high, while the average noise level is around 0.0009 magnitude. No periodicity with a signal-to-noise ratio >2 can be observed in the spectrum. Another half an hour measurement shows very similar results. Adding together normalized power spectra of the two measurements reveals no enhancement at any frequency over the period range 24s to 30 minutes.

For the second test, the artificial pulsar frequency and the chopper frequency were set to values $30Hz$ and $(30 + 1/300)Hz$, respectively, so that a 300-second beating should have resulted. The Fourier spectrum of a 2.2-hour measurement is shown below in Figure 2.9. We can see the 300-second peak, and a peak at the three times shorter period, as expected. No other periodicities, or irregularities, are present.

The third test checks the possible (quasi-periodic) noise which might be introduced with the phase-correction procedure described above (see section 2.3). In the measurement which lasted 0.45 hours, phase increments of 0.1^0 were fed to the chopper every 25s, with the same software and hardware as during observations. Consecutive images follow every 10.5 seconds. The

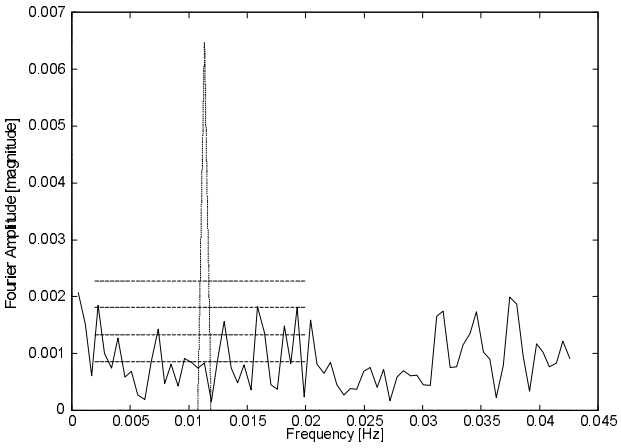

Figure 2.8: The Fourier spectra of a half an hour measurement where artificial pulsar and chopper frequencies were set to the same value (30Hz). Images follow each other at every 11.8 seconds. The dotted curve is the Fourier transform of a sine signal with the amplitude of 0.0065 magnitude, generated at times of measurement points. Parallel vertical lines show the average amplitude and three consecutive $+1\sigma$ levels. Statistical parameters were calculated using all spectral amplitudes.

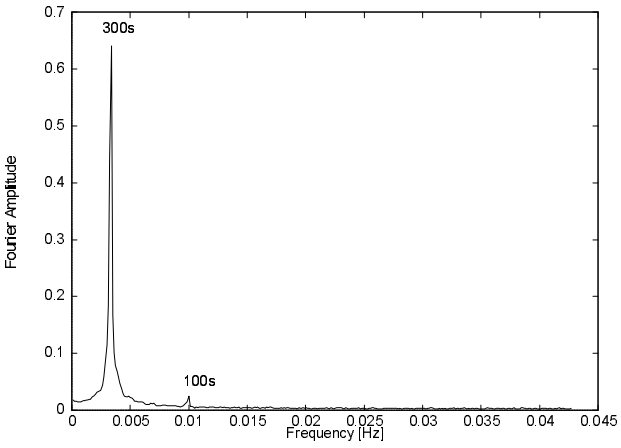

Figure 2.9: Fourier spectrum of the 2.2-hour measurement of beating between the artificial pulsar and the chopper. The peaks at the beating period 300 seconds, and at the period 100s can be observed.

resulting magnitude curve shows a constant growth. In 0.45h, the total phase difference fed to the chopper was 6.5^0. The artificial pulsar magnitude changed for 0.12. To the size of order, this change can be estimated on the basis of the beating curve considered in the previous paragraph, where a 2.13-magnitude change corresponds to a phase difference of π.

All the above presented tests did not reveal any hardware shortcomings. We therefore conclude that as far as we are able to verify, no periodicities or phase drifting were entered into the measured pulsar signal by devices that we used for stroboscopic observations.

Chapter 3

Observations and Analysis

Since the observing season 1995/96, we have been using the complete stroboscopic observing set-up as described in section 2.1. All stroboscopic observations are presented in section 3.2 below. The *new data* (obtained from 1996 to 1998) and the *old data* (obtained from 1994 to 1995, and HST data from 1991) are analyzed below. Slightly less consideration is given to the old data which have been extensively examined before. Their analysis is summarized below in section 3.1.

The Asiago 1994 and 1995 data, and the Hubble Space Telescope data, obtained by the high speed photometer in 1991, together give the following result: Crab's optical pulsations are modulated at the modulation frequency of about 1/60s, the modulation amplitude is about 0.0065 magnitude. We call this periodicity the *60s-periodicity*. We were tempted to try to explain this periodicity as the free-precessional modulation of Crab pulsations (Čadež, Galičič and Calvani 1997 [12]).

Since the detected modulation is weak, and the modulation signal-to-noise ratio hardly exceeds 3 in any individual old data set, we hoped to obtain lower noise data to find further evidence for the periodicity with a greater confidence level. Unfortunately, the noise levels in the new data obtained from 1996 to 1998 are even higher than in the old data.

To examine data for possible periodicities, we here perform two independent analyses on data sets shown in Figure 3.3 and listed in Table 2. The first one is a modification of the Fourier transform method and uses the so called Lomb algorithm. The second one is based on the phase-folding technique. Both methods enable us to determine the probability that the revealed peak does (or does not) originate from chance. The analyses' results are shown and discussed in sections 3.3 and 3.5 below. In section 3.4, cross-correlations of individual Lomb periodograms are considered. In section 3.6, pulsar's light curve is compared to other field stars' light curves, in order to check whether

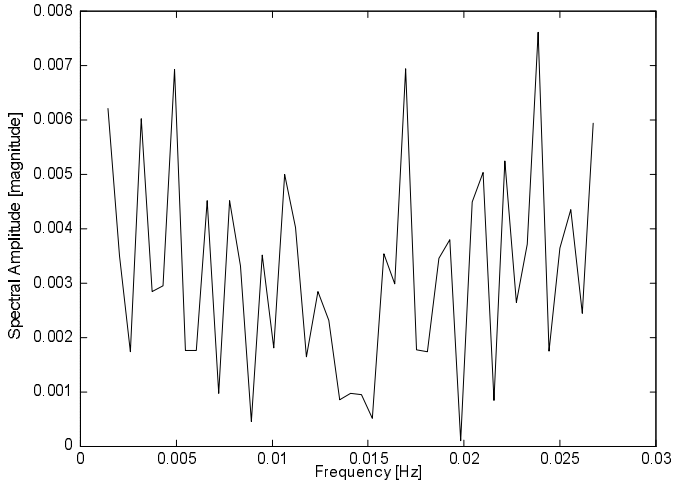

Figure 3.1: Spectrum of HST data (for details, see Čadež and Galičič 1995 [13]). The 1/60s peak (at frequency 0.01695Hz) has the amplitude 0.007 magnitude.

the noise in pulsar's light curve is consistent with noise in the light curves of other field stars.

3.1 Old Data Results

A short resume of results which were obtained with the Fourier analysis of the old data is given in this paragraph. The data and their analysis (Fourier transform method) are described in details in (Galičič 1995 [20]) and published in (Čadež and Galičič 1996 [11]). We have also analyzed the *Hubble Space Telescope (HST)* data which were obtained in October 1991 with the HST instrument High Speed Photometer (Percival et al. 1993 [41]). The analysis of these data, and results which agree with the stroboscopic observations results, are included in ([20]) and in ([11]), as well as in (Čadež and Galičič 1995 [13]) and in (Čadež and Galičič 1996 [14]).

The results of the spectral analysis of the two lowest-noise HST data sets (for the analysis details see ([14]) and ([20])) are shown in Figure 3.1. Briefly, the spectrum shown in Figure 3.1 was obtained in the following way. Each HST data set consists of pairs: photon arrival time, t_i, and the number of photons detected at this time, n_i. We represent the signal as $H(t) = \sum_i n_i \delta(t - t_i)$, with $\delta(t - t_i)$ being the Dirac delta function. Thus the Fourier transform of $H(t)$ is $F_H(\omega) = \sum_i n_i e^{i\omega t_i}$. The function $F_H(\omega)$ has peaks at $\omega_k = k\frac{2\pi}{P}$, were k is an integer and P is pulsar's period. Phase or

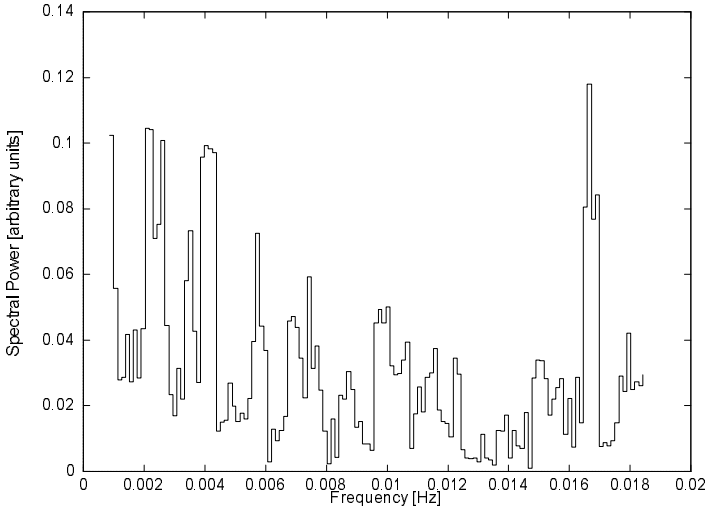

Figure 3.2: Average power spectrum: The sum of Asiago 94, Asiago 95 and HST data Fourier spectral powers. The peak at 1/60s (on the right side of the Figure) is 5 σ above the curve's noise level.

frequency modulation with frequency ω_m would show as two side-bands at frequencies $\omega_k \pm \omega_m$. We added the side-band spectra for the first ten peaks (amplitudes at higher frequencies get smaller) for the two lowest noise data sets, and summed the two spectra together. Then we folded the obtained spectrum, so that symmetrical peaks would amplify. Figure 3.1 shows this folded spectrum.

We then produced the average modulation power spectrum which is shown in Figure 3.2. It was obtained by adding together the three normalized power spectra (squares of Fourier amplitudes, where each amplitude is divided by the amplitude variance, $f(\nu)$ = amplitude/variance), where the three spectra (of data Asiago 94 and 95, and of HST data), were considered as continuous functions. For each of the three spectra ($j = 1, 2, 3$), the value of Fourier amplitude for a chosen spectral frequency ν is $f_j(\nu) = f_j(\nu_i)$, if $\nu_i - \Delta\nu_j/2 < \nu < \nu_i + \Delta\nu_j/2$, where $\Delta\nu_j$ is the width of the frequency bin of spectrum number j. The spectral power shown in Figure 3.2 is thus $F(\nu) = \sum_{j=1}^{3} f_j^2(\nu)$. The power spectrum is drawn only on the range of frequencies where all three spectra overlap. The peak at the frequency $\frac{1}{60s}$ sharpens out clearly. It rises approximately 5 σ above the average value (the noise level) in Figure 3.2, where the average value and the average value variance σ are calculated over frequencies >0.005Hz. The lower-edge frequency cut was done due to the observed 1/frequency shape of Fourier spectra of all

field stars magnitudes[1].

3.2 Data Overview

Crab stroboscopic data were obtained during a four years span, from 1994 to 1998. Observations are presented in Table 1, where also a numbering—labelling of observations—is introduced which will be used through the whole Chapter 3. In Figure 3.3, observations are presented as pulsar magnitude against time during each observing night. We can immediately notice the difference in terms of magnitude variation between the two groups of data: the bottom three curves, and the remaining ten curves. The former (except of curve No. 3) belong to the old data, while the latter (plus the curve No. 3) belong to the new data.

Table 1 gives the following information. The list of observational nights with double dates is given in the second column. The integer numbers labelling of observations is given in the first column. Any particular observation, or a subset of consecutive images will be refered to with labels as 5, or 3_1, 3_2 etc. This will, correspondingly, mean "data set No. 5", or "the first part of data set No. 3", "the second part of data set No. 3", etc. These parts are consecutive sets of one-night images which are not too noisy and not too short (see Figure 3.3), so that they are considered as input data sets for the Lomb algorithm analysis. They typically contain a few hundred images, and stretch over 0.5 to 3.2 hours. They are described in Table 2. As we can see from Figure 3.3, data obtained on 21/22 February 1997 could not be used for the analysis, and therefore data set No. 4 is not included in the following Tables. Along with the date of observation and the observatory site in the second and the third columns of Table 1, the telescope primary mirror diameter is given in the fourth column, the exposure time of images in the fifth (the exposure time is constant during each night), and an estimation of the average seeing (in arcseconds) during the night in the sixth column. For the seeing estimation, the average value of stellar image profile width parameters (σ_x, σ_y of the fitted Gausian curve) is taken. The diameter of the seeing disk given in Table 1 is thus $2\sigma_x \approx 2\sigma_y$. Seeing is not given for observations No. 4 to 9. (See footnote number 3 on page 34.) A more detailed consideration of seeing determination, and variation of $\sigma_{x(y)}$ during the night, is given in Appendix A.

[1] A detailed consideration of this subject is given in (Galičič 1995 [20]).

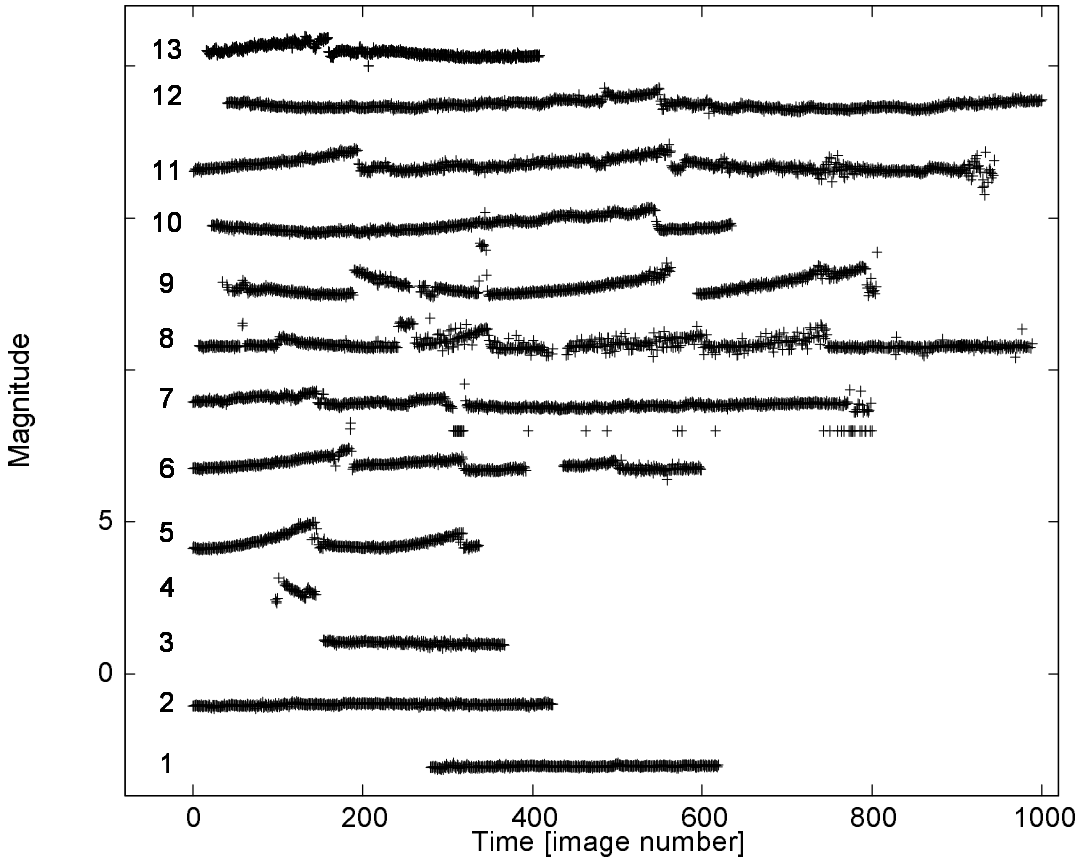

Figure 3.3: Pulsar magnitudes for observations 1 to 13 from Table 1. Curves were shifted for appropriate constant values to be shown all in one Figure. Time is measured in image numbers. Therefore, durations of individual observations can be compared in number of images, and not exactly in time. A 200 images interval would typically correspond to some 5000 seconds of observations. Exposure times are listed in Table 1 while the average intervals among successive images are listed in Table 2.

No.	Date of observation	Observatory	$D[m]$	$T_{exp}[s]$	Seeing["]
1	12/13 December 1994	Asiago(CE)	1.82	12	2.8
2	19/20 December 1995	Asiago(CE)	1.82	15	3.0
3	17/18 December 1996	Asiago(CE)	1.82	14.5	3.1
4	21/22 February 1997	Asiago	1.22	30	
5	22/23 February 1997	Asiago	1.22	15	
6	26/27 February 1997	Asiago	1.22	14.5	
7	27/28 February 1997	Asiago	1.22	14.5	
8	6/7 December 1997	Asiago	1.22	15	
9	7/8 December 1997	Asiago	1.22	15	
10	22/23 January 1998	Cananea	2.12	15.5	2.4
11	23/24 January 1998	Cananea	2.12	12.5	2.3
12	24/25 January 1998	Cananea	2.12	13.9	2.3
13	25/26 January 1998	Cananea	2.12	16.1	2.2

Table 1. Data Overview.

At the Italian Astronomical Observatory Asiago, observations from 1994 to 1996 were obtained at the 1.82m telescope (this telescope is located atop Cima Ekar, which is indicated by a "(CE)" added to "Asiago" in the third column of Table 1), while observations in 1997 were obtained at the 1.22m telescope[2]. These observations (No. 4 to No. 9) suffer from many problems[3]. Therefore we have to be aware that the results we get from their analysis have to be considered with particular caution. Observations at the Mexican Astronomical Observatory Guillermo Haro in Cananea were obtained at the 2.12m telescope.

Figure 3.3 shows the pulsar magnitude versus time for observations 1 to 13 listed in Table 1. CCD images were reduced with the Daophot software package (Stetson 1994 [52]). Pulsar magnitude is calibrated with the sum of the constant stars' signals for every image. All the data obtained in one night

[2]During the maternity leave of M. Galičič, observations were carried out by A. Čadež and A. Gomboc in December 1996, and by A. Čadež and B. Dintinjana in February 1997.

[3]The 1.22m telescope is located just above the town of Asiago and the observing conditions (seeing, light polution etc) are not excellent. Besides, due to some problems with the primary mirror, the diffraction pattern is occasionally disturbed so that stellar images substantially differ from the Gaussian shape. It is therefore not possible to estimate the average seeing from the average (Gaussian) stellar profile shape during the night. Often, pulsar and the star next to it can not be separated in the image, which means that Daophot considers them both as one star, while in some other cases it does separate them. Therefore we believe that additional noise is introduced in this way and that quite some of the virtually strong (quasi)periodicities in those data are due to mixing of pulsar's and next-to-pulsar star's photons. One could expect that with such 'corrupted' data, the weak 60s-periodicity could not be detected.

are shown for each night, but not all the data of each night are included in the Fourier analysis. We can notice in Figure 3.3 that individual observations exhibit different noise levels, and that the noise content also changes during one observation. Magnitude curves are consecutively shifted upwards by a constant value so that they can clearly be presented in one Figure. Therefore, the absolute value of the magnitude on the y-axis has no meaning, the labels "0" and "5" are marked on the y-axis to keep a possibility to estimate a 1-magnitude difference in an individual magnitude curve. The sharp sudden jumps towards smaller magnitudes in the majority of curves are due to the manual phase corrections which we introduced when we had noticed that pulsar was going substantially dimmer. The problem is discussed in section 2.3.

3.3 Periodic Variability Search in the Data with the Lomb Periodogram (Fourier) Method

Astronomical data are usually unevenly sampled. In our case, the unevenness results from the CCD camera and software limitations. The *Lomb (or Lomb-Scargle) periodogram* method (Press 1989 [44]) was made to be used for Fourier spectral analysis in cases when data are unevenly sampled. We analyze all the stroboscopic data (see Table 2) with this method. Spectra are shown as spectral amplitude depending on frequency. The presence of a peak at the frequency 1/60s is examined in every individual spectrum. Probabilities that these peaks do not originate from noise are estimated with the error function (Gauss probability integral). Theoretical details of discrete Fourier analysis, and of statistic stohastic processes, are given in (Galičič 1995 [20]).

We have N data points m_i given at times t_i, $i = 1...N$ (pulsar magnitudes[4] in our case) with the average value $\overline{m} = \frac{1}{N}\sum_i m_i$, and variance $\sigma^2 = \frac{1}{N-1}\sum_i (m_i - \overline{m})^2$. The result of spectral analysis with the *Lomb algorithm* (Press et al. 1992 [45]) is a periodogram—spectral power $P_N(\omega)$

[4]We consider magnitudes instead of fluxes, and the reasons for that are given in (Galičič 1995 [20]). We will present them only briefly here. Before the Fourier transform is calculated, data are always averaged and the average is subtracted from them, m_i-$\overline{m}$ = δm_i. Now the flux (or the number of detected photons during the exposure time) is $f(t_i) = \overline{f}10^{-0.4\delta m_i}$, where $\overline{f}$ is the average flux. Magnitudes δm_i are typically very small (a few thousandths), therefore we may understand them as relative deviations of flux from its average value, $f(t_i) \approx \overline{f}(1 - 0.92\delta m_i)$. The Fourier amplitudes given in magnitudes are then understood as relative deviations of the detected number of photons from the average value.

against frequency $\omega = 2\pi\nu, \nu > 0$,

$$P_N(\omega) \equiv \frac{1}{2}\left(\frac{[\sum_i (m_i - \overline{m})\cos\omega(t_i - \tau)]^2}{\sum_i \cos^2\omega(t_i - \tau)} + \frac{[\sum_i (m_i - \overline{m})\sin\omega(t_i - \tau)]^2}{\sum_i \sin^2\omega(t_i - \tau)}\right) \tag{3.1}$$

The constant τ is defined by the relation

$$\tan(2\omega\tau) = \frac{\sum_i \sin(2\omega t_i)}{\sum_i \cos(2\omega t_i)} \tag{3.2}$$

It is an offset that makes $P_N(\omega)$ completely independent of shifting all the t_i's by any constant (Press et al. 1992 [45]). Lomb has shown that the offset chosen as in eq. (3.2) makes equation (3.1) identical to the equation that one would obtain if one estimated the harmonic content of a data set, at a given frequency, by linear least-squares fitting to the model $h(t) = A\cos\omega t + B\sin\omega t$.

On the y-axis of spectra shown below, the spectral amplitude

$$A(\omega) = \sqrt{P_N(\omega)}$$

with P_N given in eq. (3.1) is given in magnitudes.The spectral amplitude calibration uses the Lomb periodogram transform of a sine wave $f_S(t_i) = A_0 \sin(2\pi\frac{k}{T}t_i)$ generated at data points times t_i for each data set (T is the duration of the data set in seconds, k is an integer, so that k/T is one of the spectral frequencies; A_0 is the sine amplitude in magnitudes). The normalizing factor F_0 is defined so that in the spectrum of $f_S(t_i)$, the spectral amplitude at frequency $\frac{k}{T}$ is equal to A_0. In the *normalized* amplitude data spectrum, amplitudes $A(\omega)$ are thus multiplied by $\frac{A_0}{F_0}$.

Table 2 describes the stroboscopic data sets which were analyzed with the Lomb algorithm. The columns of Table 2 are: **1** number/label of the data set, **2** limits of spectrum's images intervals, **3** number of images, N, **4** number of images of the set which were used for the Lomb peridogram, i.e. with magnitudes $m \leqq \overline{m} + 2\sigma$, N_{incl}, **5** average time interval between two successive images, ΔT, **6** duration of the whole data set, T, **7** average Fourier amplitude of the spectrum, $\langle A_{FT}\rangle$. The last column is the average noise level in the considered data set, and therefore a direct measure for the "data quality".

In Figures 3.4 and 3.5, only spectra corresponding to data sets listed in Table 2 which have noise levels $\leqq 0.004$ magnitude are shown. With this criterium, 13 selected spectra are shown altogether, the first 7 fullfilling the criterium, from the top to the bottom of Table 2 in Figure 3.4, and the next 6 in Figure 3.5. The 0.004 magnitude noise level limit was chosen on

the basis of previous 60s-periodicity search results which are cited in the introduction to Chapter 3 and in section 3.1. With a noise level of ∼0.004 magnitude, the 0.006 magnitude peak would be $\sim 1\sigma$ above the average if $\sigma \sim 0.002$ magnitude. The noise levels in column 7 of Table 2 are defined as the average spectral amplitude over spectral frequencies $\geqq 0.003Hz$. We excluded frequencies lower than $0.003Hz$ because in these parts of spectra, the $1/f$-noise component is typically the most prominent. The main noise contributions in photometric data, and the assumption of the 1/f-noise due to atmospheric scintillation, are considered in (Galičič 1995 [20]). At frequencies $\approx 0.003Hz$, the $1/f$-shape predominantly ceases in any field star's spectrum (see also Fourier spectra of other field stars in section 3.6).

1	2	3	4	5	6	7
No.	Images interval	N	N_{incl}	$\Delta T[s]$	$T[s]$	$\langle A_{FT} \rangle [mag]$
1	305-619	305	292	22.7	6981	0.0019
2	0-424	425	403	26.7	11423	0.0021
3	154-247,300-367	162	161	22.1	4706	0.0019
5	0-312	279	264	24.9	7770	0.0023
6_1	0-165	166	159	24.4	4026	0.0033
6_2	189-316	128	121		3100	0.0040
6_3	319-389	71	69		1709	0.0065
7_1	0-146	147	140	24.4	3564	0.0050
7_2	155-297	143	136		3468	0.0050
7_3	298-772	449	430		11599	0.0025
8_1	101-241	135	129	26.6	3591	0.0042
8_2	748-981	220	213		5852	0.0037
9_1	66-189	124	117	26.6	3278	0.0050
9_2	348-528	181	175		4801	0.0039
9_3	594-720	127	119		3368	0.0057
10_1	22-190	169	162	25.4	4262	0.0034
10_2	210-450	241	227		6089	0.0030
10_3	557-633	77	76		1935	0.0040
11_1	1-192	191	182	22.3	4270	0.0042
11_2	232-330	99	94		2192	0.0080
11_3	331-470	140	133		3117	0.0055
11_4	471-563	93	86		2065	0.0090
12_1	40-460	421	401	23.8	9988	0.0024
12_2	630-930	301	289		7163	0.0031
13	16-139	124	119	26.1	3203	0.0064

Table 2. Spectra statistics.

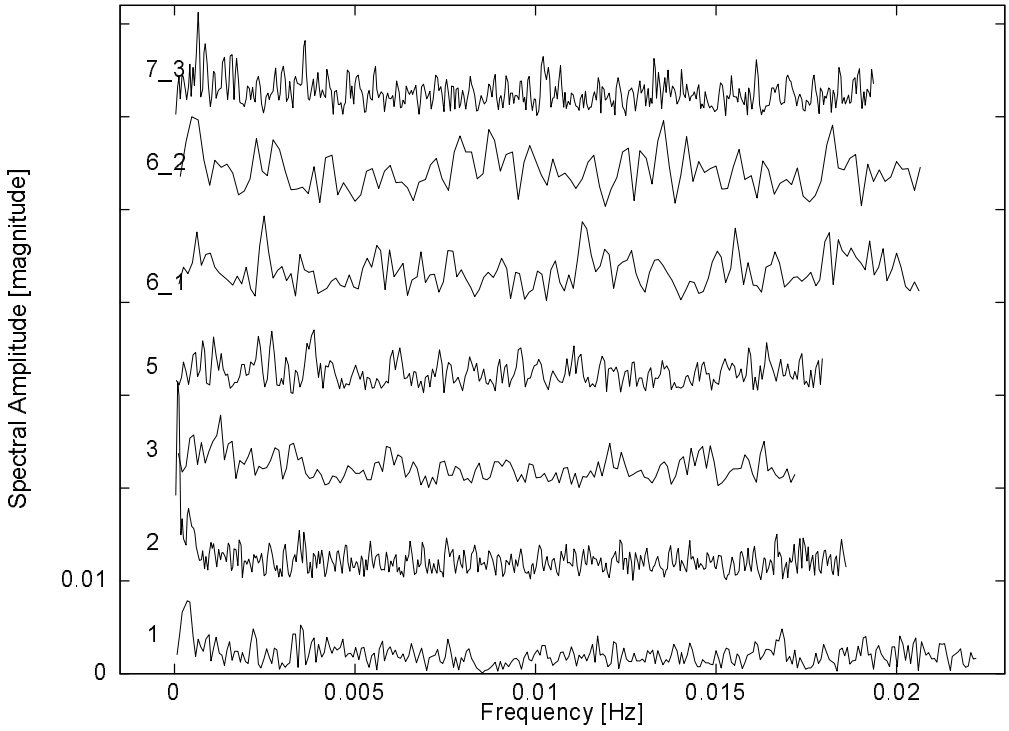

Figure 3.4: Lomb peridograms of those first seven data sets listed in Table 2, which have noise levels $\leqq 0.004$ magnitude (see the labelling of corresponding data sets on the left side of the Figure and in Table 2). Fourier amplitude is shown in magnitudes. In order to fit them in one Figure, each spectrum is shifted by approximately 0.01 magnitude. Only values "0" and "0.01" are written at corresponding tics on the y-axis to indicate the scale.

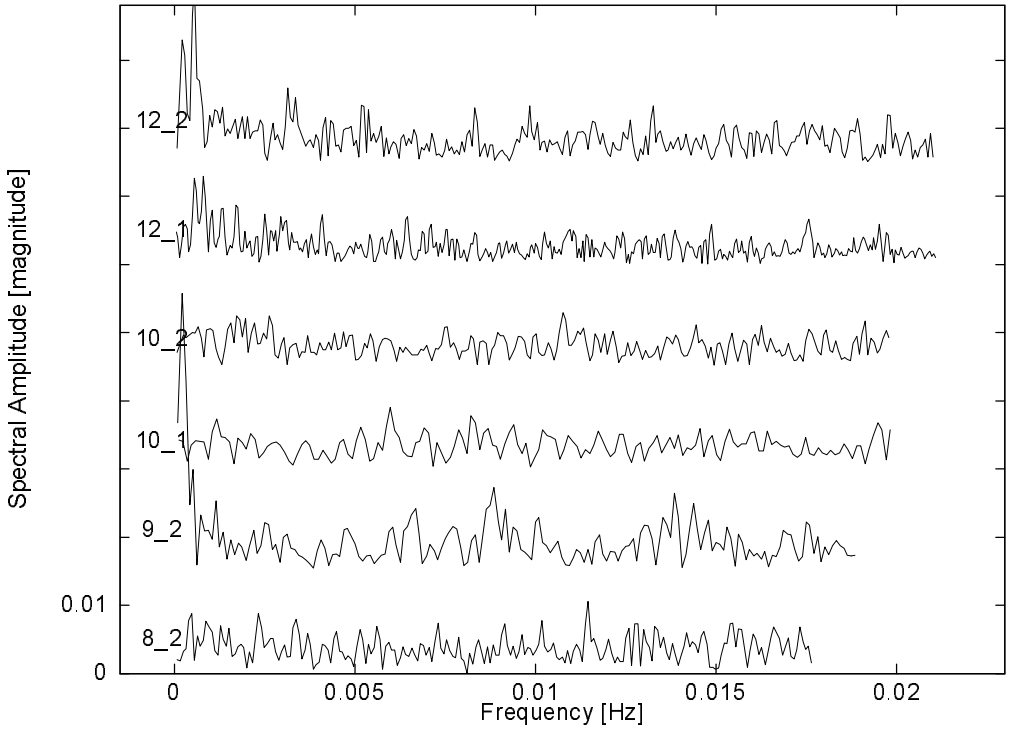

Figure 3.5: Lomb peridograms of the next six data sets listed in Table 2, which have noise levels $\leqq 0.004$ magnitude (see the labelling of corresponding data sets on the left side of the Figure and in Table 2). Fourier amplitude is shown in magnitudes. In order to fit them in one Figure, each spectrum is shifted by approximately 0.01 magnitude. Only values "0" and "0.01" are written at corresponding tics on the y-axis to indicate the scale.

As we have indicated in the introduction to this Chapter, we want to search for the presence of the 60s-periodicity in the new data. The results listed in Table 3 shows no significant peak at this frequency in the Lomb periodograms of the new data. In Table 3 below, the statistical significances of the 1/60s peak, if discernible, for spectra shown in Figures 3.4 and 3.5 are given. In the last line of Table 3, the HST spectra shown in Figure 3.1 is considered. For all the spectra considered in Table 2, we searched for any significant peak on the frequency range $0.01625Hz$ to $0.01760Hz$. Those spectra where a peak was found in the considered range are included in Table 3. The first column of Table 3 gives numbers of data sets as labelled in Table 2, the second and the third columns give the peak frequency and its amplitude. The frequency error in the third column $\Delta\nu$ is half the spectral frequency bin, and the amplitude accuracy is $\sigma_{FT} = \sqrt{\langle A_{FT}^2\rangle - \langle A_{FT}\rangle^2}$, the variance of spectral amplitudes A_{FT}. Column "PH" is the peak height expressed as the ratio $\frac{A_{Peak}-\langle A_{FT}\rangle}{\sigma_{FT}}$. As in (Galičič 1995 [20]), the statistical significance of the peak is estimated with the error function (Bronštejn and Semendljajev 1980 [7]), based on the assumption that peak amplitudes are normally distributed. The probability that the peak is not due to noise is given in the fifth column of Table 3.

Data Set	Frequency [Hz]	Amplitude [mag]	PH	Probability
1	**0.01678**±0.00007	**0.0047**±0.0010	**2.9**	**0.96**
2	**0.01670**±0.00004	**0.0050**±0.0010	**3.0**	**0.97**
3	0.0163±0.0001	0.0050±0.0011	2.7	0.94
5	0.01641±0.00006	0.0056±0.0013	2.6	0.93
6_1	0.01664±0.0001*	0.0054±0.0018	1.2	<2/3
7_3	0.01698±0.00004*	0.0045±0.0013	1.5	<2/3
10_2	0.01757±0.00008*	0.0055±0.0015	1.7	0.77
12_1	0.01757±0.00005	0.0066±0.0014	3.0	0.97
12_2	0.01668±0.00007*	0.0058±0.0019	1.4	<2/3
HST	**0.01695**±0.0003	**0.007**±0.003	**1.95**	**0.83**

Table 3: Summary of the Lomb spectra and significances of the 1/60s peak.

A few values in Table 3 are flagged with an asterisk (*) which means that there are other (usually more than one) higher peaks in the neighbourhood, but the cited peak is the closest to 1/60s and can be noticed since it is wider and/or slightly higher than the peaks in its immediate neighbourhood.

Lomb periodograms show clear peaks at 1/60s only for data sets No. 1 and 2, which belong to the old data group. The probabilities that the two do not originate from chance are 96%[5] and 97%, respectively. Data No. 3 have

[5]Discrete Fourier analysis (not a Lomb periodogram) gave a slightly higher PH (3.3)

a peak of 94% probability at frequency 1/61s. Among the 1.22m telescope data, only No. 5 shows a peak at 1/61s (93% probability). Among the 2.12m telescope data, a significant peak (97% probability) is found in data set No. 12_1 at 1/57s, and a less significant peak (77% probability) in data set No. 10_2 at the same frequency. However, this period does not overlap with the 60s-period (see Figure 3.6). For the HST data, values in the last row in Table 3 refer to the spectrum shown in Figure 3.1. The peak at 1/59s has 83% probability.

The results presented in Table 3 are graphically shown in Figure 3.6. We can see that three data sets, 1, 2, and HST (in Table 3, the corresponding lines are written in bold) have overlapping results. The resulting frequency ν_r is

$$\nu_r = (0.01679 \pm 0.00016) Hz \tag{3.3}$$

The mean frequency is calculated as a weighted mean of the three frequencies, $\overline{\nu} = \frac{\sum \nu_i p_i}{\sum p_i}$, $i = 1, 2, 3$, where the weight is the probability from the last column of Table 3. The frequency accuracy is determined as $\Delta\nu = \sqrt{\frac{\sum \Delta\nu_i^2 p_i^2}{\sum p_i^2}}$. The mean frequency and its errorbar belts are shown in Figure 3.6 as dotted vertical lines.

The average modulation amplitude, calculated in a similar way as the resulting frequency above, i.e. with amplitudes from the third column in the first two and the last row of Table 3, and probabilities from the last column of Table 3 as weights, is

$$A_{mod} = (0.0055 \pm 0.0015)\ magnitude \tag{3.4}$$

In conclusion, we have to stress again that only the old data contribute significantly to these results, the 60s-periodicity frequency and amplitude given in eqs. (3.3) and (3.4). Lomb spectra corresponding to data sets from the new data group, as we can see from Table 3 and in Figures 3.4, 3.5 and 3.6, do not contribute to the confirmation of the 60s-periodicity in Crab optical pulsations.

We next consider the distribution of spectral amplitudes since our assumption above was that they are normally distributed. In the case of white noise, one would expect that the two dimensional probability distribution $w(x, y)$ of real and imaginary parts x and y of Fourier transform is Gaussian

$$w(x, y) = \frac{1}{2\pi\sigma} \exp(-\frac{x^2 + y^2}{2\sigma^2}) \tag{3.5}$$

for data set No. 1, and a correspondingly higher probability, 98% (Galičič 1995 [20]).

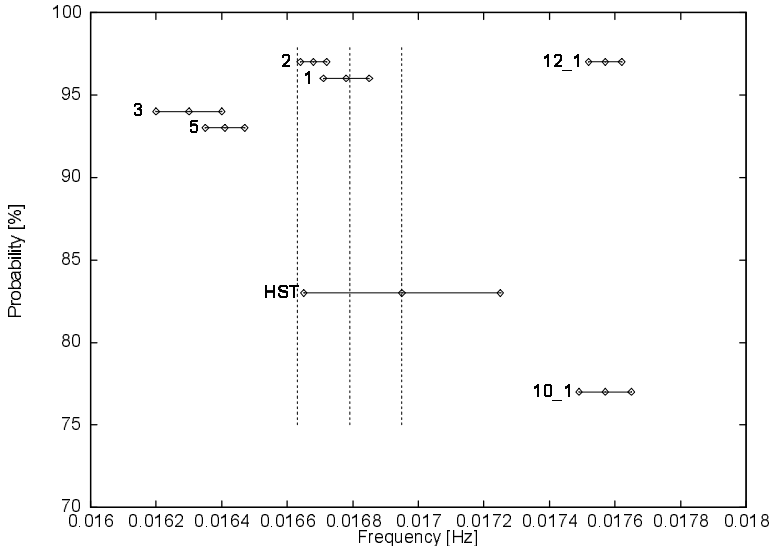

Figure 3.6: Graphical presentation of results given in Table 3. Probability (in %) is given for every spectral frequency at which a significant peak was found for the data listed in Table 3, on the frequency range 0.01625Hz to 0.0176Hz.The errorbar $\Delta\nu$ is half the spectral frequency bin for every spectrum.

Accordingly, the expression for the amplitude distribution ($A = \sqrt{x^2 + y^2}$) is

$$w(A) = \frac{A}{\sigma} \exp(-\frac{A^2}{2\sigma^2}) \tag{3.6}$$

In pairs of Figures (3.7, 3.8), and (3.9, 3.10), the distribution of spectral amplitudes for all spectra shown in Figures 3.4 and 3.5, and for the lowest noise data, No. 1, 2, 3 and 5, are shown, respectively. For the first measured distribution in each Figures pair, all spectral amplitudes were taken in account, while for the second measured distribution, amplitudes at spectral frequencies $< 0.003Hz$ were excluded. On the x-axis, the spectral amplitude is labelled in magnitudes, and on the y-axis, the number of amplitudes that fall into every magnitude interval (0.0003 magnitude step) is labelled as the number of hits. In each Figure, the measured distribution and its fit according to eq. (3.6), are drawn. We can see that in all Figures, points in the distributions tails are above the values of fitted curves. In both Figures pairs, the effect is slightly stronger if all spectral amplitudes are included in the distribution. This justifies the exclusion of the 1/f-spectral region for the $\langle A_{FT} \rangle$ and σ_{FT} calculation[6]. The interesting point is that even if we cut

[6]If we compare the values of the distribution width (σ) which is written in captions of

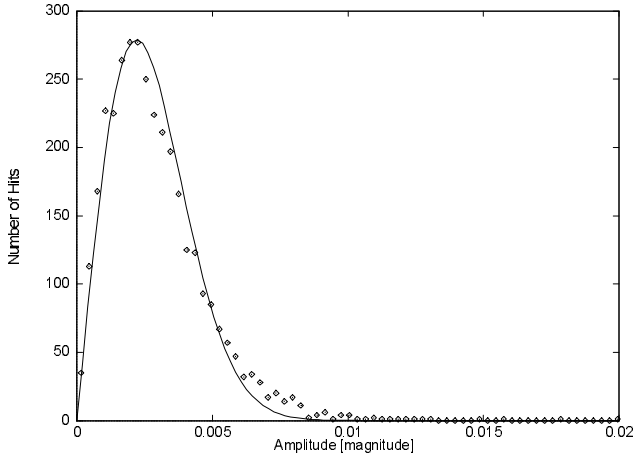

Figure 3.7: Distribution of spectral amplitudes for all spectra shown in Figures 3.4 and 3.5. All spectral amplitudes were included in the measured distribution. The fitted curve (solid line) has $\sigma = 0.0022$ magnitude.

away the 1/f-dominated spectral parts, there is still a non-Gaussian excess in the distribution tails. This leads us to conclude that a non-white component is present in the pulsar signal, which may not originate (only) in the atmospheric variations.

We can see no significant features if we compare the first pair of Figures. In the second pair, where only the lowest-noise spectra amplitudes were taken into account, we can see the (small) excesses at amplitudes 0.005 and 0.007 amplitude in Figure 3.9. While the second one is not present in Figure 3.10, the excess at the amplitude 0.005 remains here as well. The amplitude 0.005 magnitude is the typical size of the 1/60s-peak amplitude (see Table 3). Unfortunately, we do not have enough spectra to build the probability distribution at any chosen frequency. If this were the case, we could directly compare the distribution at frequency 1/60s, to distributions at other spectral frequencies, and check whether the excess at the amplitude 0.005 magnitude has to do with the 60s-periodicity. Instead, we assumed that the probability distributions at any frequency behave in the same way on average, and have therefore built a single distribution with all spectral amplitudes taken together. We therefore can not conclude that the excess in the amplitude distribution at 0.005 magnitude is due to spectral amplitudes at 1/60s, but can only conclude that spectral amplitudes do not seem to be

Figures 3.7 to 3.10, we can also see, as expected, that the distribution narrows if 1/f- (the noisier) part of the spectra is excluded.

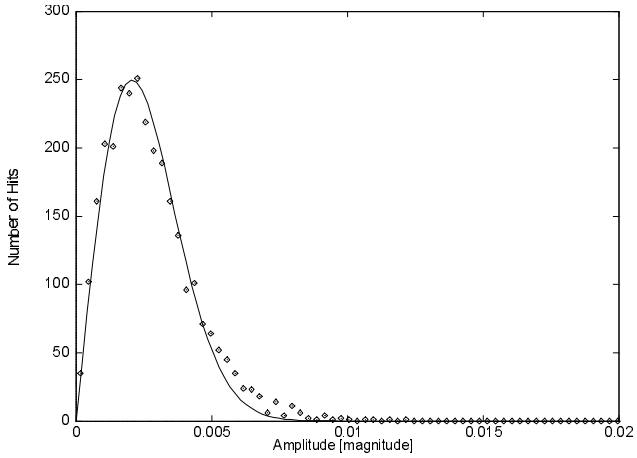

Figure 3.8: Distribution of spectral amplitudes for all spectra shown in Figures 3.4 and 3.5. Only spectral amplitudes at spectral frequencies $\geqq 0.003Hz$ were included in the measured distribution. The fitted curve (solid line) has $\sigma = 0.00205$ magnitude.

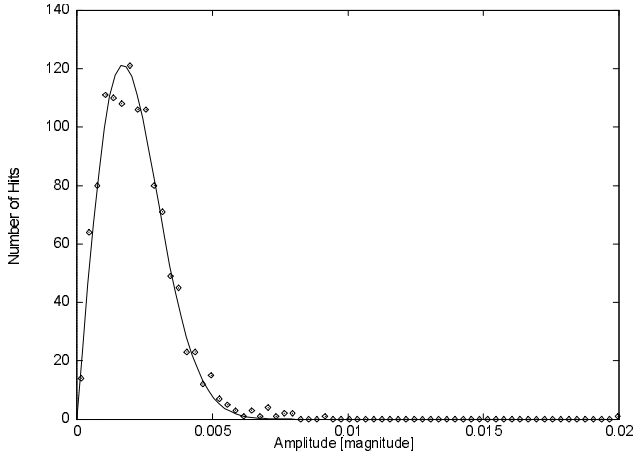

Figure 3.9: Distribution of spectral amplitudes for the lowest noise spectra (No. 1, 2, 3 and 5). All spectral amplitudes were included in the measured distribution. The fitted curve (solid line) has $\sigma = 0.0017$ magnitude.

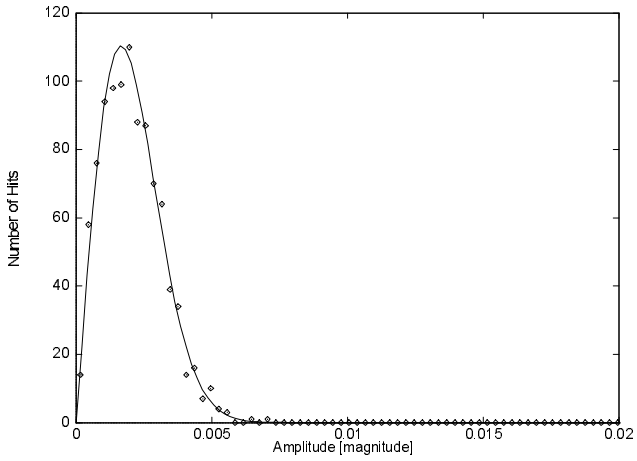

Figure 3.10: Distribution of spectral amplitudes for the lowest noise spectra (No. 1, 2, 3 and 5). Only spectral amplitudes at spectral frequencies $\geqq 0.003Hz$ were included in the measured distribution. The fitted curve (solid line) has $\sigma = 0.00165$ magnitude.

exactly normally distributed, which may hint to the presence of extra noise in the pulsar data. This question is further addressed in section 3.6.

We next build the distribution of spectral amplitudes for the star designated by number 7 in January 1998 observations, to compare it to the above considered distributions of spectral amplitudes corresponding to pulsar data sets. In this way we want to see if the pulsar's signal noise contents is different from the noise content of another star's signal. Star number 7's spectra from three observations, 22/23, 23/24, and 24/25 January 1998 (the same spectra as in the section 3.6) are used. The star number 7 is only 0.4 magnitude fainter than the pulsar, and is the second brightest star in January 1998 CCD images. Here we can see notably more excess in the tail in Figure 3.11 than in Figure 3.12, where spectral amplitudes at spectral frequencis $< 0.003Hz$ were excluded. This argues for the hypothesis that the 1/f-shape of spectra is due to atmospherically produced noise[7]. What remains also in Figure 3.12 is the excess which peaks at the amplitude 0.0077 magnitude. We can not note an excess at 0.005 magnitude as in Figure 3.10, but what we can learn here is that an excess in the probability distribution at some amplitude, particularly in the distribution tail where the number of amplitudes gets smaller, can happen by chance.

Finally, we wish to compare spectra presented in Figures 3.4, 3.5 and 3.1

[7]See also the discussion in Appendix A.

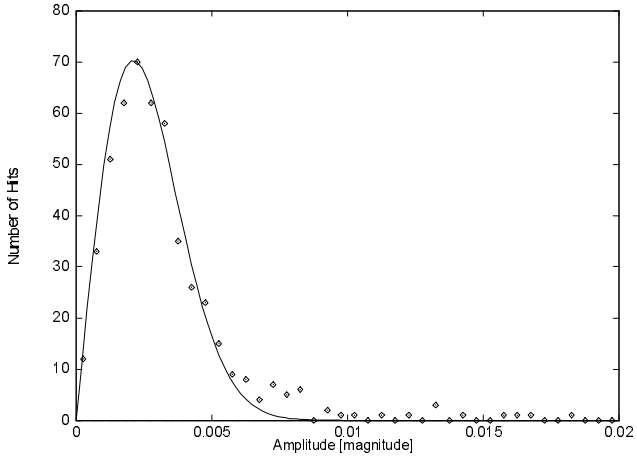

Figure 3.11: Distribution of spectral amplitudes for the star number 7, for three spectra (observations January 1998). All spectral amplitudes were included in the measured distribution. The fitted curve (solid line) has $\sigma = 0.0021$ magnitude.

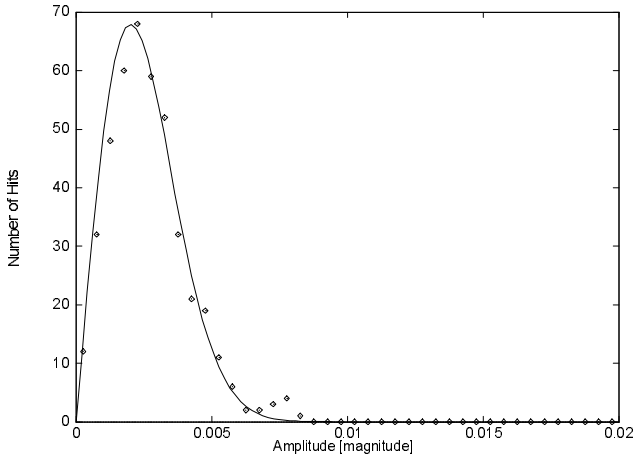

Figure 3.12: Distribution of spectral amplitudes for the star number 7, for three spectra (observations January 1998). Only spectral amplitudes at spectral frequencies $\geqq 0.003 Hz$ were included in the measured distribution. The fitted curve (solid line) has $\sigma = 0.002$ magnitude.

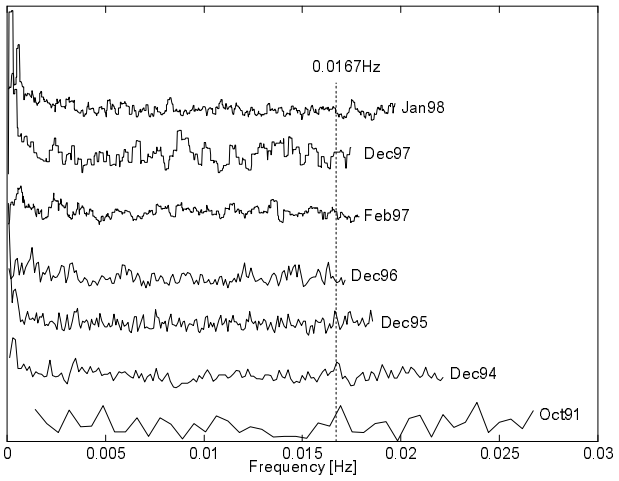

Figure 3.13: Spectra (or spectra sums for contemporate observations) of observations aligned upwards according to increasing date of observation. The labelling on the right side of each spectrum refers to the corresponding month and year of observation(s).

in chronological order. In Figure 3.13, these spectra are redrawn: the bottom spectrum corresponds to the oldest data, and the top spectrum to the latest data. Using this Figure, we can make two points. First, we can see that only spectra corresponding to the old data have a notable peak at 60s (follow the vertical line in the Figure), while this periodicity can not be noted in the new data spectra. Second, we wish to compare the position of the 1/60s peak, if present, according to the date of observation, to check for a possible temporal rule. Observations from the same season are summed together[8]. The dotted vertical line in Figure 3.13 is drawn at frequency $0.0167Hz$. If the 1/60s peak in pulsar data was due to a periodic small-amplitude oscillation connected to pulsar rotation as we have proposed in ([12]), then the peak's frequency would change with time as the pulsar slows down. In the frequency region around $1/60Hz$ in Figure 3.13, in direction upwards, we can follow the peak in the bottom three curves. There is also a peak on the left from the vertical line in the spectrum labelled by "Dec96", but its leftwards shift is about 3-times larger as it would have to be should it reflect the process manifested in the three spectra below it. (It is interesting to note that the amount of change of the exact 1/60s frequency value (ν_k) per year, $\delta\nu/1year = \frac{\nu_k - \nu_{94}}{k-94}$, where e.g. $k = 95$ for the observation No. 2, is the same if we compare "Oct91"

[8]Only Lomb periodograms of data sets with $\langle A_{FT} \rangle \leqq 0.004$ are included in sums labelled "Feb97", "Dec97", and "Jan98".

(HST) and "Asi95" data' 1/60s-frequency value to the "Asi94" data' 1/60s-frequency value. Correspondingly, for the two, $|\delta\nu/year|$ is $5 \cdot 10^{-5} Hz$ and $8 \cdot 10^{-5} Hz$. For "Asi96", it is $2 \cdot 10^{-4} Hz$. This shift does have the correct sign, but it is more than 3 times too large compared to the "Asi95" and "Oct91" shifts.) In the top three spectra, labelled "Feb97", "Dec97" and "Jan98", no significant peaks can be observed on the left side of the vertical line.

We may conclude that with the Lomb spectral analysis method applied on the previously analyzed data, and on the new data, the significance of previous results is not improved. Those results are also not disproved or contradicted. On average, the noise level is higher for the "new data" than it was for the "old data". It is not surprising that with the new noisier data, we can not improve the significance level of the modulation seen in the old data.

3.4 Cross-Correlations of Pairs of Lomb Periodograms

Pairs of Lomb peridograms which were shown in section 3.3, are cross-correlated to check whether the same periodicity is present in every pair of spectra examined.

The theory behind this procedure is as follows. We consider two series of a time-dependent signal, $x(t)$ and $y(t)$. We want to know whether they represent two statistically independent Gaussian noises, or if they maybe contain a common periodic component. For that purpose we build the cross-correlation function

$$K[x,y](\tau) = \frac{1}{T}\int_{\tau}^{T} x(t)y(t-\tau)dt \tag{3.7}$$

Signals $x(t)$ and $y(t)$ both contain a periodic signal with period p, if $K[x,y](\tau)$ is a periodic function with this period. The periodicity search uses Fourier transform of the cross-correlation function from eq. (3.7), symbolically written as $F[K[x,y](\tau)](\omega)$, which is equal to the product of Fourier transforms of functions $x(t)$ and $y(t)$, $F[x(t)](\omega)$ and $F[y(t)](\omega)$,

$$F[K[x,y](\tau)](\omega) \ = F[x(t)](\omega) \cdot F[y(t)](\omega)$$

In case the signals $x(t)$ and $y(t)$ are Gaussian noises, each of their Fourier spectral amplitudes $A_{x,y}(\omega)$ is a stohastic process for every spectral frequency $\omega_k = \frac{2\pi k}{T}$, and the spectral power (amplitude squared), $P_{x,y} = |A_{x,y}(\omega)|^2$, is

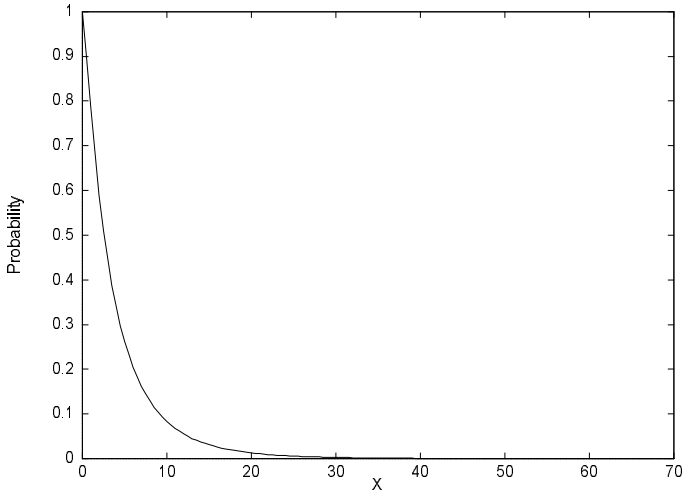

Figure 3.14: The probability (according to eq. (3.10)) that a value $\widetilde{\Pi}_0$ (labelled by "X" on the x-axis) appear by chance in the cross-correlation function.

randomly distributed according to

$$w(P_{x,y}) = \frac{4P_{x,y}}{\overline{P}^2_{x,y}} e^{-2P_{x,y}/\overline{P}_{x,y}} \tag{3.8}$$

where $\overline{P}_x$ and $\overline{P}_y$ are average values of P_x, P_y. Now the probability that the value of product $\Pi = P_x P_y$ is inside the interval $[\Pi, \Pi + d\Pi]$ can be calculated by

$$W(\widetilde{\Pi}) = \widetilde{\Pi} \int_{-\infty}^{\infty} e^{-2\sqrt{\widetilde{\Pi}} ch(z)} dz \tag{3.9}$$

where $\widetilde{\Pi} = \frac{4\Pi}{\overline{P}_x \overline{P}_y}$ and $e^z = \frac{P_x}{P_y}$. The probability that the value Π in the cross-correlation function of two processes happens to be greater than a value Π_0 by chance is, therefore

$$Prob(\widetilde{\Pi}_0) = \int_{\widetilde{\Pi}_0}^{\infty} d\widetilde{\Pi} W(\widetilde{\Pi}) \tag{3.10}$$

where the integral $W(\widetilde{\Pi})$ is written in eq. (3.9), and $\widetilde{\Pi}_0 = 4\Pi_0/(\overline{P}_x \overline{P}_y)$. The probability graph, calculated by eq. (3.10) is given in Figure 3.14.

Cross-correlation functions are constructed as products of corresponding squares of amplitudes $P_x(\omega)$, $P_y(\omega)$ (spectral power) of Lomb spectra shown in section 3.3; x and y here label two different Lomb spectra, corresponding to data sets $x(t)$ and $y(t)$. For every cross-correlation function

labelled here simply by P_xP_y, we can easily get the expected or average value $\langle P_xP_y\rangle = \frac{1}{N}\sum_i (P_xP_y)_i$, where i counts every of the N values of P_xP_y for spectral frequencies $\geqq 0.003Hz$, which is the same frequency limit as in section 3.3. We can then compare the cross-correlation function value at any chosen frequency (e.g. at 1/60s), to the average value $\langle P_xP_y\rangle$. We define the cross-correlation coefficient Ra as the ratio of the value of cross-correlation function at frequency 1/60s, $(P_xP_y)_{1/60}$, and the average cross-correlation function value, $\langle P_xP_y\rangle$,

$$Ra = \frac{(P_xP_y)_{1/60}}{\langle P_xP_y\rangle} \tag{3.11}$$

For every value Ra of eq. (3.11), the probability that such a value appears by chance can be estimated by eq. (3.10). We only have to take in account that the argument in eq. (3.10) is $\widetilde{\Pi}_0 = \frac{4\Pi_0}{\overline{P_x}\,\overline{P_y}}$, which is not exactly the same as Ra in eq. (3.11).

Spectra listed in Table 2 (see section 3.3) were included in cross-correlations, with exceptions of the noisiest data (6_3, 7_1, 7_2, 9_1, 9_3, 11_2, 11_3, 11_4, 13; the spectra labelling is the same as in section 3.3, see the first column of Table 2). The HST data spectrum (shown in Figure 3.1) which is not included in Table 2, is labelled by number 0 in this section. Thus the total number of spectra used is 17, and the corresponding number of cross-correlation functions is 136. Each cross-correlation function is labelled by the two spectra used, e.g. the cross-correlation function of HST data spectrum (0) and Asiago 1995 data spectrum (2) is labelled by (0, 2) in the corresponding Figure, in Tables 4, 5, and 6, 7, as well as later in the text if it is mentioned in particular. In Tables 4 and 5, the cross-correlation coefficient (Ra) values according to eq. (3.11) are given for those cross-correlation functions where the considered 1/60s peak is observed. Several values are flagged with an asterisk (*), which means that either the noted peak is not very prominent comparing to other peaks (there are several higher or comparably high peaks in the cross-correlation), or that the frequency value is most probably too much displaced from 1/60s. In Tables 6 and 7, probabilities that the observed peaks are **not** due to chance are given in %; these probabilities are therefore $1 - Prob(\widetilde{\Pi}_0)$, where $Prob(\widetilde{\Pi}_0)$ is calculated by eq. (3.10). Only probabilities for those Ra-s which are not flagged with asterisks (51 values) in Tables 4 and 5 are given in Tables 6 and 7. At the end of this section, plots of the first 15 out of 51 cross-correlation functions are shown in Figures 3.16 to 3.30. Plots of the remaining 36 cross-correlation functions are shown in Appendix C.

Figure 3.15 shows the Ra-s against corresponding frequency values, of 51 cross-correlation functions (those which have their Ra-values written in

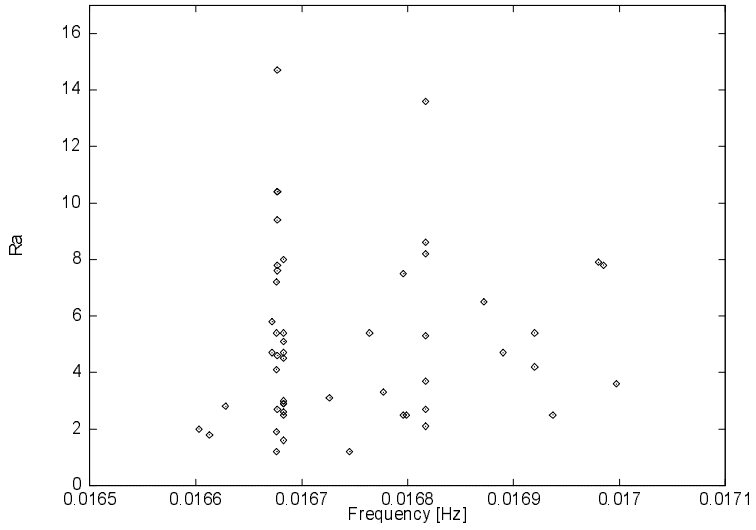

Figure 3.15: The values of cross-correlation coefficient Ra (see Tables 4 and 5) against frequency.

Tables 4 and 5, and are not flagged with asterisks). If we leave out the three points on the very left side, and the eight points on the very right side of Figure 3.15, there are 40 points gathered in a narrow frequency interval[9] between $0.01665Hz$ and $0.01685Hz$. Out of the total number of 136 cross-correlations functions, 40 represents 29.4%.

Again we can note that the most important contribution in terms of the highest probabilities at the same frequency comes from cross-correlations of spectra No. 0, 1, 2, which represent the old data. We can see in Table 6 that some probabilities corresponding to the 60s-peak are very high, allowing as little as a few thousandths or hundredths of a percent for the probability that this peak is due to chance. The new data spectra contribute particularly when correlated with the old data spectra. On average, the probability that the peak at 60s observed in 40 cross-correlation functions is not due to chance (the average value of probabilities given in Tables 6 and 7) is 97%.

[9]Its width 0.0002Hz is equal to 1/5000s, and 5000s is a reasonable estimate for a typical data set duration.

	0	1	2	3	5	6_1	6_2	7_3
1	13.7							
2	14.7	10.4						
3								
5	7.5	8.2						
6_1	5.4	5.3	7.8		2.5			
6_2	2.5	2.1						
7_3	7.8	3.1	4.5			2.5		
8_1	6.3*	3.3*		12.2*	9.5*	3.2*	4.3*	
8_2	7.1	4.7	7.6		2.0	4.1		2.6
9_2	6.5	4.7			2.1*			
10_1	3.3	3.7	4.6		7.8*			
10_2	3.6	1.3		7.0*			4.2*	
10_3	2.5	2.7	2.7					
11_1	7.9	8.6	9.4					3.0
12_1	5.4	4.2			3.6*			
12_2	8.0	5.8	10.4			4.7		2.9

Table 4: Cross-correlation: Ratios *Ra* (see the text above).

	8-1	8_2	9_2	10_1	10_2	10_3	11_1	12_1
1								
2								
3								
5								
6_1								
6_2								
7_3								
8_1								
8_2								
9_2								
10_1	5.1*	1.9						
10_2								
10_3		1.2						
11_1	8.8*	5.4		2.8	8.7*			
12_1								
12_2		5.1		2.9	1.8	1.6	5.4	

Table 5: Cross-correlation: Ratios *Ra* (see the text above).

	0	1	2	3	5	6_1	6_2	7_3
1	99.998							
2	99.997	99.99						
3								
5	99.7	99.95						
6_1	98.4	99.5	99.94		93.5			
6_2	85.9	87.1						
7_3	99.9	97.8	99.5			93.5		
8_1								
8_2	99.7	99.3	99.93		90.9	98.1		93.0
9_2	99.4	98.6						
10_1	94.9	97.9	99.1					
10_2	97.0	79.5						
10_3	92.9	96.8	96.5					
11_1	99.9	99.9	99.98					96.3
12_1	99.4	98.6						
12_2	99.9	99.8	99.99			99.3		96.8

Table 6: Cross-correlation: Probabilities (see the text above).

	8-1	8_2	9_2	10_1	10_2	10_3	11_1	12_1
1								
2								
3								
5								
6_1								
6_2								
7_3								
8_1								
8_2								
9_2								
10_1		90.9						
10_2								
10_3		81.4						
11_1		99.0		94.9				
12_1								
12_2		99.2		95.6	87.1	88.2	99.7	

Table 7: Cross-correlation: Probabilities (see the text above).

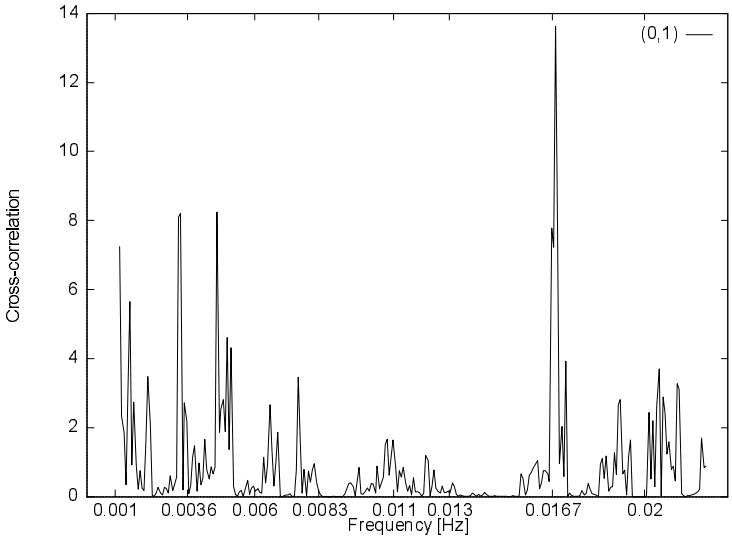

Figure 3.16: Cross-correlation: Data sets No. 0 and 1.

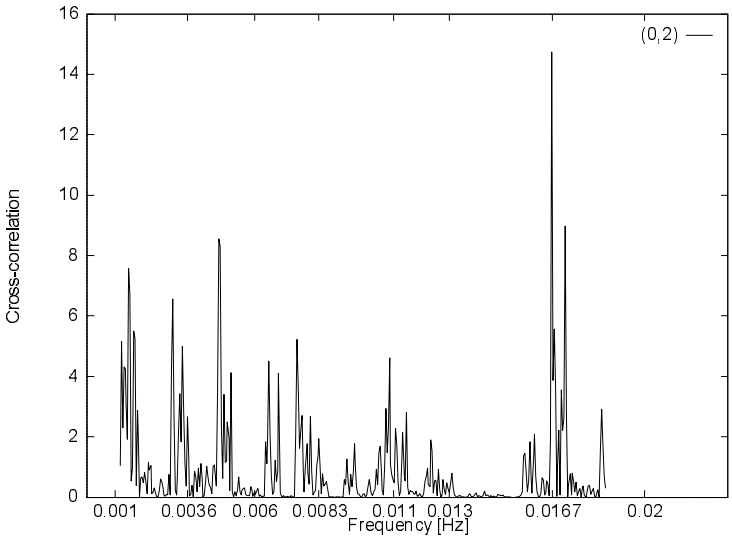

Figure 3.17: Cross-correlation: Data sets No. 0 and 2.

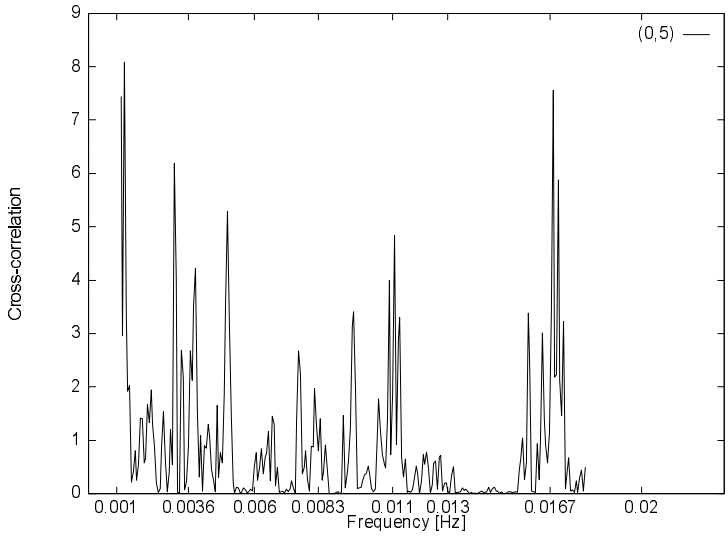

Figure 3.18: Cross-correlation: Data sets No. 0 and 5.

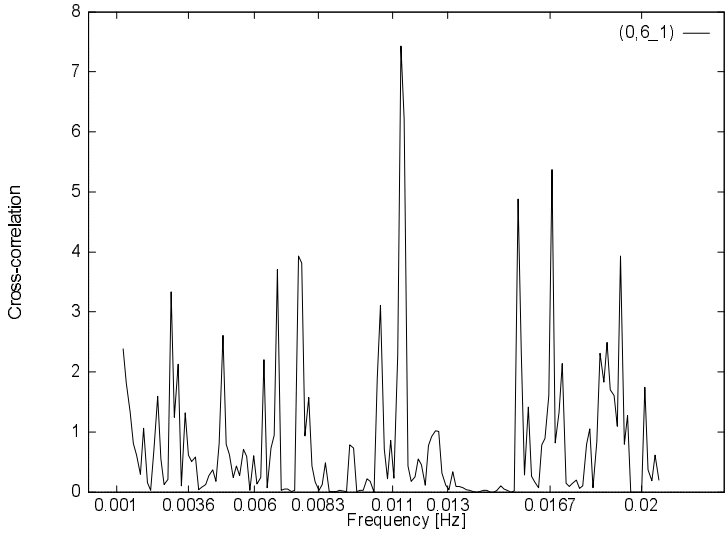

Figure 3.19: Cross-correlation: Data sets No. 0 and 6_1.

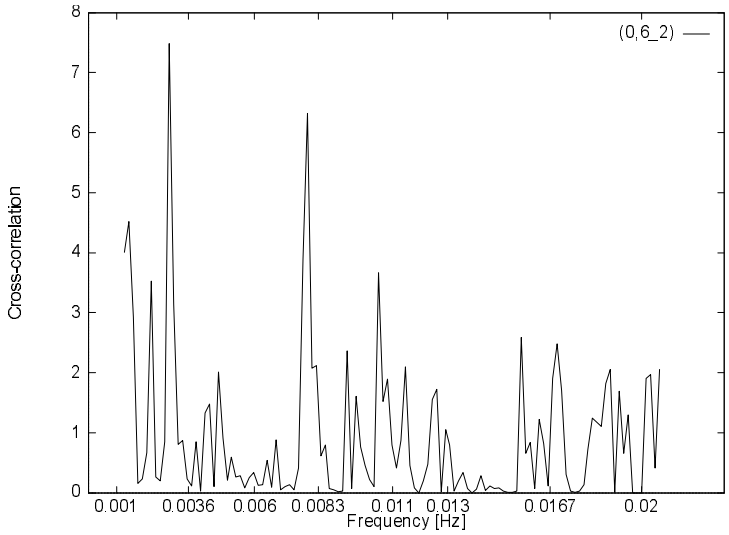

Figure 3.20: Cross-correlation: Data sets No. 0 and 6_2.

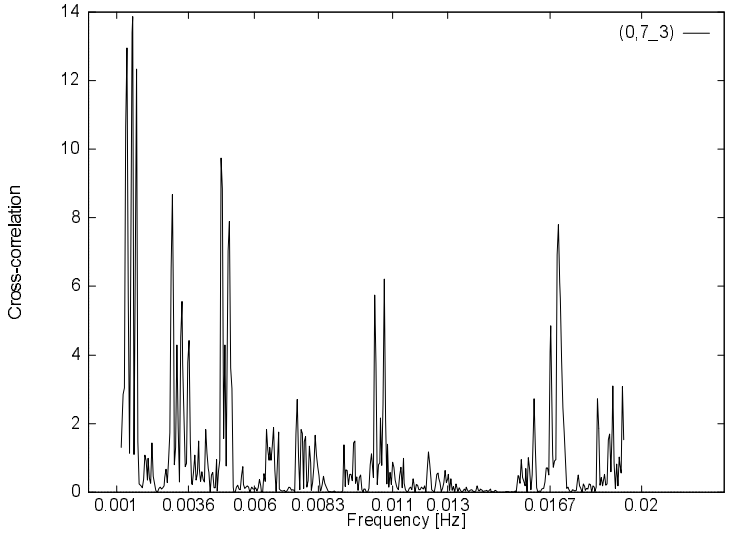

Figure 3.21: Cross-correlation: Data sets No. 0 and 7_3.

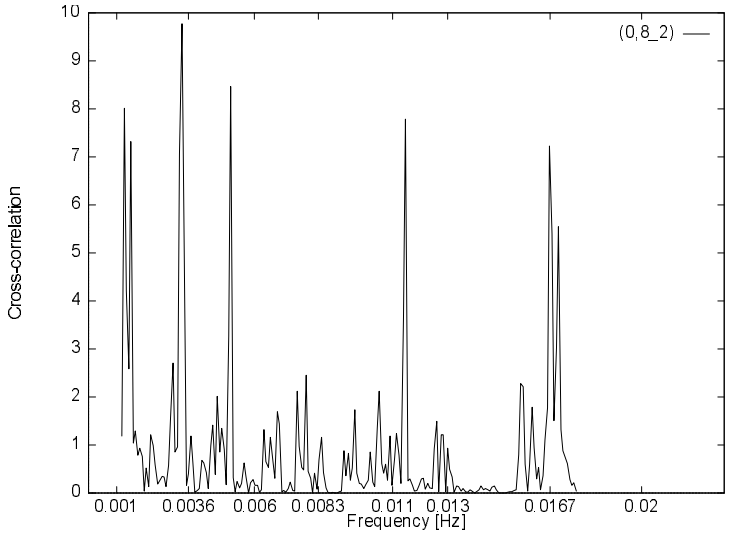

Figure 3.22: Cross-correlation: Data sets No. 0 and 8_2.

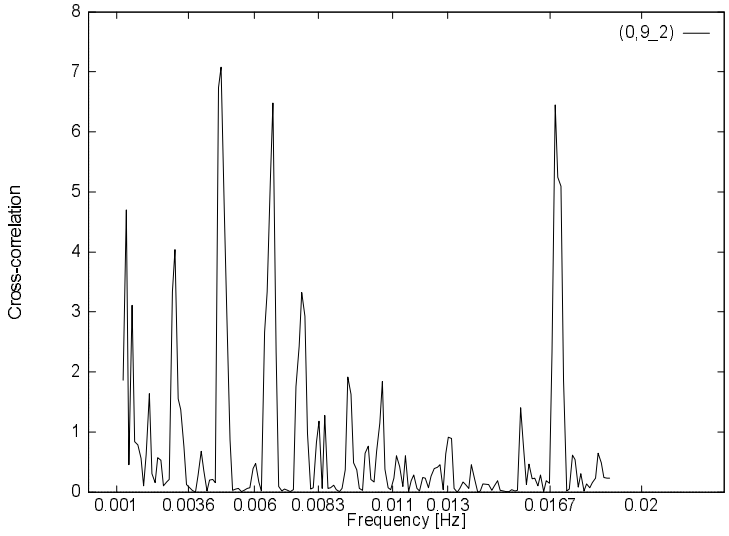

Figure 3.23: Cross-correlation: Data sets No. 0 and 9_2.

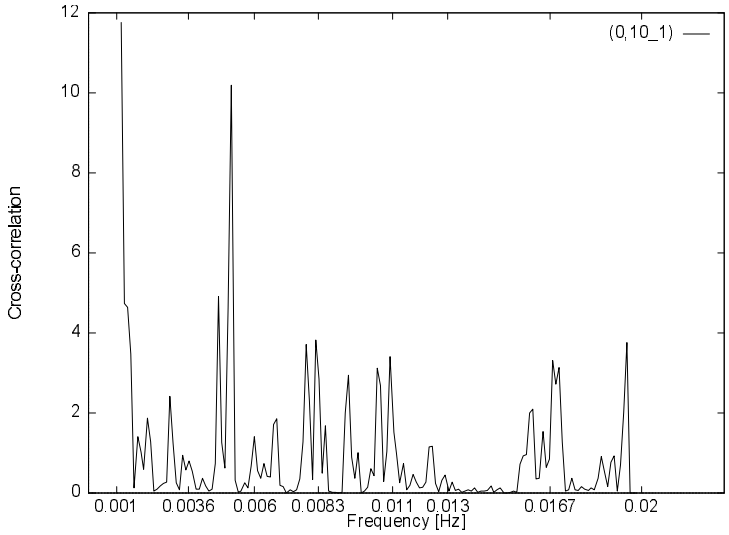

Figure 3.24: Cross-correlation: Data sets No. 0 and 10_1.

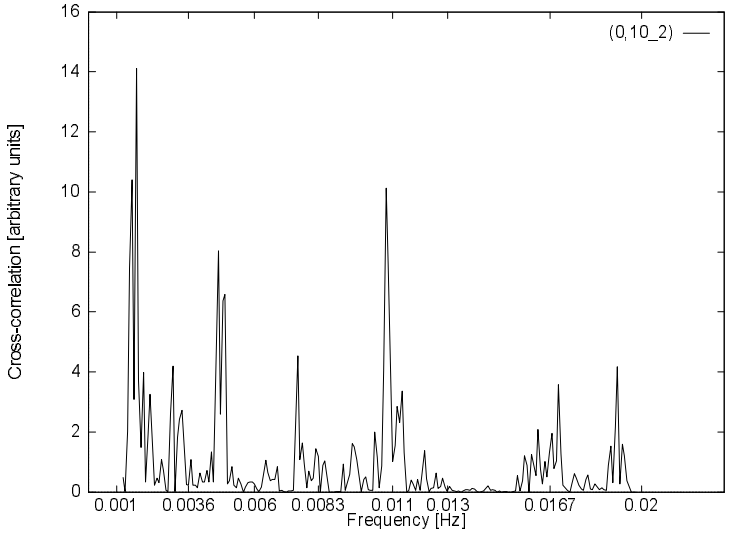

Figure 3.25: Cross-correlation: Data sets No. 0 and 10_2.

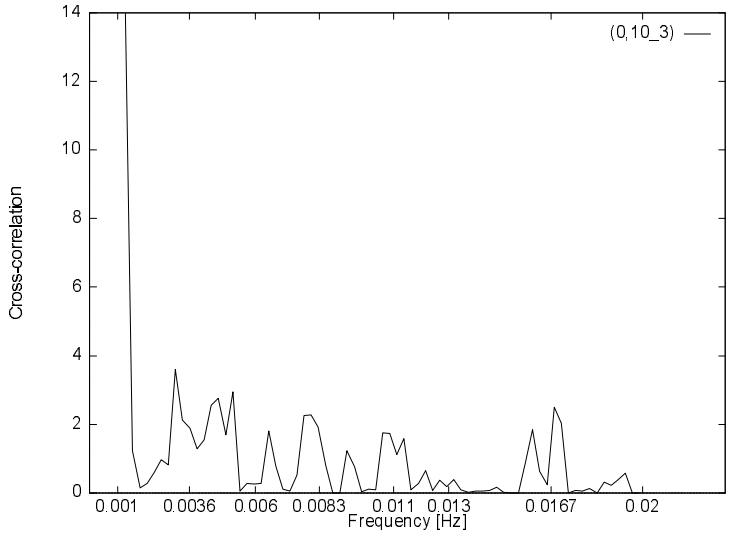

Figure 3.26: Cross-correlation: Data sets No. 0 and 10_3.

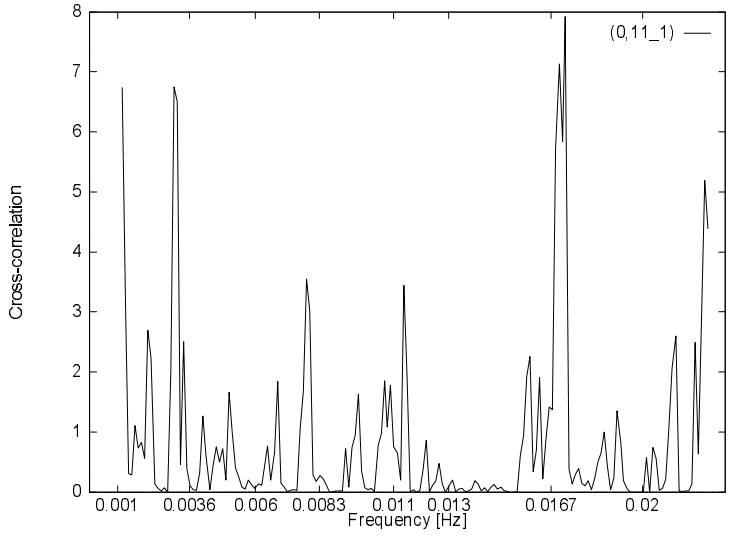

Figure 3.27: Cross-correlation: Data sets No. 0 and 11_1.

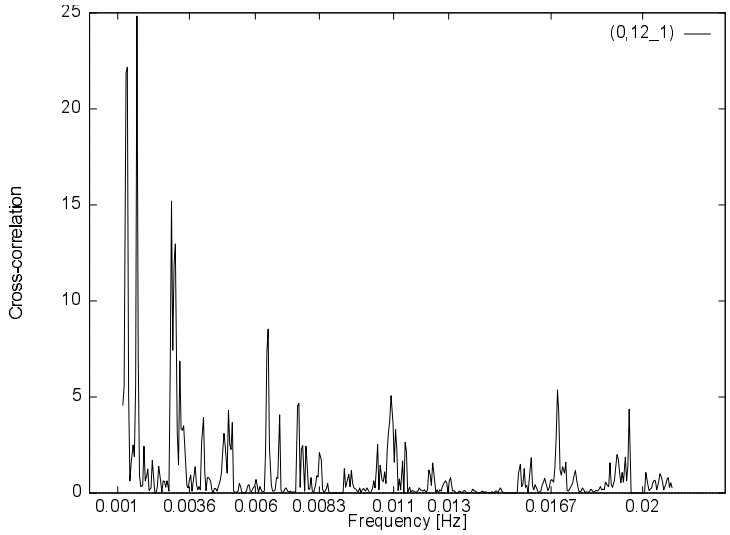

Figure 3.28: Cross-correlation: Data sets No. 0 and 12_1.

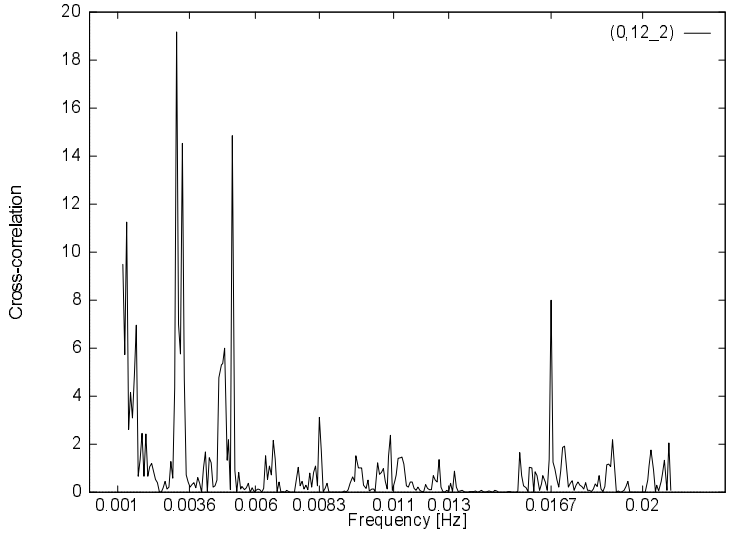

Figure 3.29: Cross-correlation: Data sets No. 0 and 12_2.

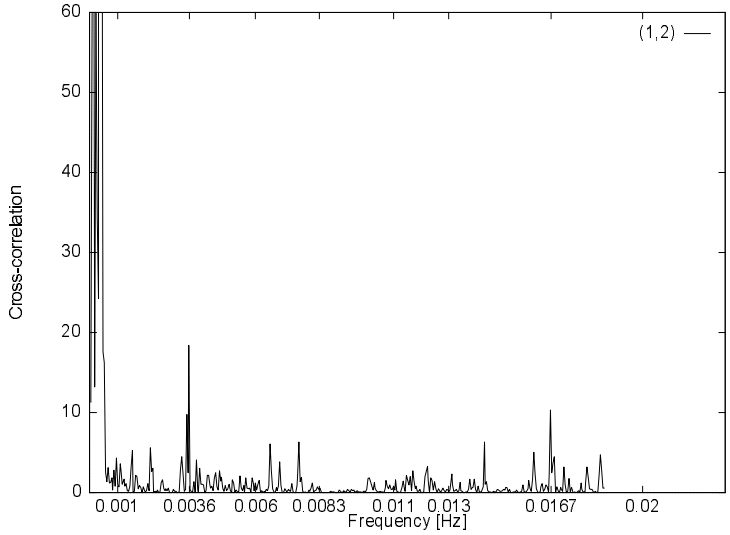

Figure 3.30: Cross-correlation: Data sets No. 1 and 2.

3.5 Periodicity Search by the Epoch-Folding Technique

A time series of N observations m_i is folded at a trial period. The folded data are then grouped into M phase bins. If a period P is tried, each phase bin is $\frac{P}{M}$ wide in time units. The sample mean is $\overline{m} = \frac{1}{N}\sum_{j=1}^{N} m_i$, and the sample variance $\sigma^2 = \frac{1}{N-1}\sum_{i=1}^{N} (m_i - \overline{m})^2$. The uniformity of phase bin means is tested with the assumption that a datum m_{kj} in the j^{th} data bin can be written as a sum of the true bin mean μ_j and the measurement error ϵ_{kj}, $m_{kj} = \mu_j + \epsilon_{kj}$, where ϵ_{kj} are assumed to be independent random variables with identical mean and variance, and have a Gaussian distribution. The null hypothesis of uniformity across the space, $\mathcal{H}_o$, states that all the phase bin means are identical, while rejection of $\mathcal{H}_o$ usually implies that the scatter of bin means is too great to be consistent with the uniformity of phase bin means. The varying of phase bin mean with phase is taken as a strong evidence for periodicity in the data. The method is often used for periodicity search in data dominated by counting statistic (Leahy 1987 [35]), or to search for a coherent signal in large amounts of data with low or moderate signal-to-noise ratio (Larsson 1996 [34]). Our Crab data are noisy, therefore we hoped that this method of periodicity search may prove useful in our case.

To decide on the presence of a periodicity in the data considered, the epoch-folding statistic Q^2 is defined as

$$Q^2 = \sum_{j=1}^{M} \frac{(\overline{m_j} - \overline{m})^2}{\sigma_j^2} \tag{3.12}$$

where $\overline{m_j}$ is the j^{th} bin average value, and σ_j is the population variance in the j^{th} phase bin. Assuming that the conditions for the null hypothesis are met, σ_j^2 can be estimated by $\sigma_j^2 \approx \frac{\sigma^2}{n_j}$, and equation (3.12) can be written as

$$Q^2 = \frac{1}{\sigma^2} \sum_{j=1}^{M} n_j (\overline{m_j} - \overline{m})^2 \tag{3.13}$$

where n_j is the number of sample points in the j^{th} phase bin. If the scatter of the bin points is as expected for Gaussian noise with variance σ_j, the expected value of Q^2 is $\sim M - 1$. A high value of Q^2 ($> M - 1$) would thus point to the presence of a periodicity which significance can be estimated with the χ^2 distribution function with $M - 1$ degrees of freedom ([34]). An improved test statistic L which is statistically sound for all sample sizes (the number of data points enters in L and in the probability assessment function), and is claimed to be more sensitive to periodicity than Q^2 and other test statistics previously used in epoch-folding, has been proposed by Davis in 1990 ([15]). It is defined as

$$L = \frac{(N - M) \sum_{j=1}^{M} n_j (\overline{m_j} - \overline{m})^2}{(M - 1) \sum_{j=1}^{M} \sum_{k=1}^{n_j} n_j (m_{kj} - \overline{m_j})^2} \tag{3.14}$$

and is connected to Q^2 by the relation

$$L = \frac{(N - M) Q^2}{(M - 1)(N - 1 - Q^2)} \tag{3.15}$$

The L-statistic is distributed according to the so-called F-distribution with $M - 1$ and $N - M$ degrees of freedom ([15]). In the case of Gaussian noise, the expected value of L is

$$L \sim 1 \tag{3.16}$$

F-distribution probability function occurs in statistical tests of whether two observed samples have the same variance. Quantity F (in our case the statistic L) is the ratio of the observed variance of the first sample to that of the second sample (Press et al. 1992 [45]). (In our case, this is the ratio of the variation of bins means, and variations in individual bins, see eq. (3.14)). Let $\mathcal{P}'(F|\nu_1, \nu_2)$ denote the probability that F would be as large as it is if the first sample's underlying distribution has smaller variance than the second sample's underlying distribution. Parameters ν_1 and ν_2 are F-distribution's

degrees of freedom. The probability $\mathcal{P}'(F|\nu_1,\nu_2)$ is calculated using the incomplete Beta function I ([45])

$$\mathcal{P}'(F|\nu_1,\nu_2) = I_{\frac{\nu_2}{\nu_2+\nu_1 F}}(\frac{\nu_2}{2},\frac{\nu_1}{2}) \tag{3.17}$$

For a trial period in the phase folding method, a larger L implies a more probable rejection of the hypothesis $\mathcal{H}_o$. While $\mathcal{P}'$ measures the probability that the nonvariability accross all phase bins can be attributed to the normal distribution of data points, $1-\mathcal{P}' \equiv \mathcal{P}$ can be interpreted as the probability that the periodicity is present in the data. For our case, $\mathcal{P}$ can be calculated as

$$\mathcal{P} = 1-\mathcal{P}'(L|M-1,N-M) = 1-I_{\frac{N-M}{N-M+(M-1)L}}(\frac{N-M}{2},\frac{M-1}{2}) \tag{3.18}$$

In practice, one may want to build one's own distribution function for the L-statistic. The probability for the presence of the tested period can then be estimated as the ratio of the appropriate area determined by a certain value of L, to the total area under the measured distribution function. For that purpose, white noise[10] was generated at times of pulsar data points, and the folding procedure was done for the period 60s (other tested periods gave the same results on average) so that the L value was obtained in exactly the same way as it was obtained for the pulsar data analysis. The procedure was repeated 20000 times with data points times of sets No. 2 and 12, and 6000 times for data points times of data set No. 1. The three distribution functions coincide remarkably well, therefore one of them[11] was chosen as the probability assessment measure. The distribution of L values, and a measured relation "Probability against L", are given in Appendix B. The probability assessed to any L using the method described in this paragraph coincides very well, within $\leq 0.5\%$, with the one obtained with eq. (3.18).

For all the observations listed in the first column of Table 8, data were folded into 4 phase bins, and trial periods from $55s$ to $65s$ were tested. The period increment

$$\Delta P = \frac{P^2}{T} \tag{3.19}$$

was determined with the condition $\frac{2\pi}{P} - \frac{2\pi}{P+\Delta P} = \frac{2\pi}{T}$, where T is duration of the data set in seconds (the third column of Table 8). It varies with P, but for the considered short period interval, ΔP as obtained with the interval middle

[10]The Turbo Pascal 6.0 random generator was used.

[11]The one generated at times of data set No. 12 which is the largest data stretch (953 points).

value $P = 60s$ was taken for the whole interval. The period increments were calculated for each data set in particular[12], and they range from 1.12s for the shortest data set, to 0.15s for the longest data set.

To compare the values of L for different periods in the chosen period range, we calculated the average value of the L-statistic on the considered period range, $\langle L \rangle$, and its variance σ_L. We decided to consider further only those peaks in each data set which had probabilities $L \geqq \langle L \rangle + 2\sigma_L$. In the third column of Table 8, the period of the highest L peak in the searched period range is written, and its probability according to eq. (3.18) in the fifth column. Several values are flagged with an asterisk (*), which means that there is one (or more) other peak(s) which have $L \geqq \langle L \rangle + 2\sigma_L$ in the examined period interval, too. One might guess whether those peaks arise from some non-white noise component in the data. This statement may be supported by the observation that this particularly often happens in data sets which were obtained at the 1.22m telescope[13]. The period uncertainty in the third column of Table 8 is $\Delta P/2$ with ΔP from eq. (3.19).

Data set No.	$T[s]$	P_{Max_Peak}	L	prob.[%]
1	6868	$(60.0 \pm 0.26)s$	2.7	95.4
2	11423	$(60.0 \pm 0.16)s$	4.2	99.4
3	4684	$(56.2 \pm 0.38)s$	2.9	96.2
5	7770	$(56.3 \pm 0.23)s$*	4.2	99.3
6	9494	$(55.5 \pm 0.19)s$	2.5	94.4
7	18875	$(64.2 \pm 0.09)s$*	2.5	94.4
8	23509	$(57.1 \pm 0.07)s$*	3.7	98.8
9	17448	$(56.3 \pm 0.10)s$*	2.0	88.6
10	15540	$(63.0 \pm 0.11)s$	3.8	98.99
11	12583	$(55.4 \pm 0.14)s$	3.7	98.8
12	22878	$(64.6 \pm 0.08)s$*	2.9	96.6
13	3203	$(60.0 \pm 0.56)s$	1.9	87.4

Table 8: Epoch-folding results: Peaks on the period interval 55s to 65s.

The probabilities in the last column of Table 8 are rather high. To decide if they do reflect real phenomena, or they might be only statistical fluctuations, one may first want to compare them, or the values of the corresponding L's, on a broder range of periods. Figures 3.31 and 3.32 show values of the L-statistic for data obtained at the 1.82m telescope (data sets No. 1 to 3)

[12]Testing with artificially generated signals, and with the data, showed that a too fine period resolution may produce spurious very high values of L, while with a too rough resolution, one would miss certain periodicities.

[13]See footnote number 3 on page 34.

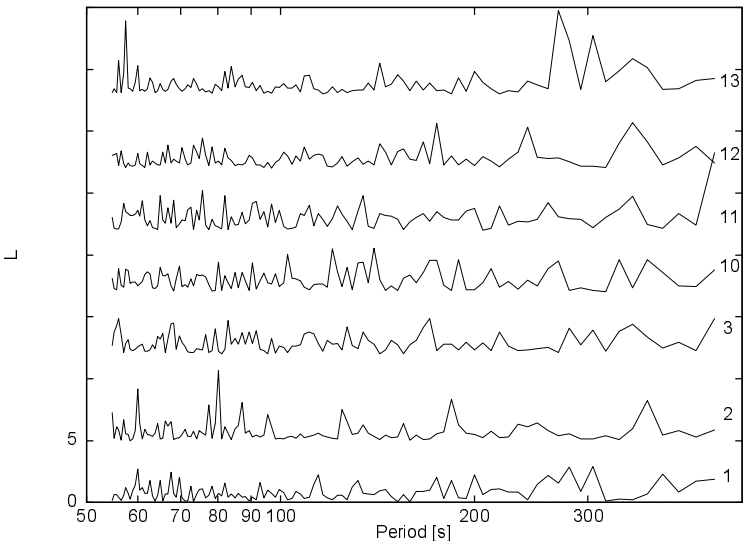

Figure 3.31: L statistic for data sets No. 1 to 3, and 10 to 13, on the period range 55s to 500s. The scale on the x-axis is logarithmic. Consecutive curves are shifted upwards to show them all in one Figure, and labels "0" and "5" on the y-axis indicate the scale.

and 2.12m telescope (data sets No. 10 to 13), and at the 1.22m telescope (data sets No. 5 to 9), respectively. Note that the curves in both Figures are shifted upwards for around +5 each, therefore the L values "0" and "5" on the y-axis can only serve to estimate the height of any L knowing that tics on the y-axis are separated by 5. For each data set, the period range 55s to 500s was searched. A constant frequency increment $\Delta\nu = 0.000144Hz$ is taken instead of a constant period increment, so that a trial period P_1 is calculated from the preceding period P as

$$P_1 = \frac{1}{1/P - \Delta\nu}$$

At $P = 60s$, the chosen $\Delta\nu$ gives $\Delta P \approx 0.5s$. Average values of L's for all data sets are about 1, as expected from the theory (eq. (3.16)). In Figure 3.31, peaks at the period 60s can be observed clearly in curves labelled 1 and 2. Yet, there are also a few other comparably high or higher peaks at different, but not the same, periods in both curves. The L-statistic curves shown in Figures 3.31 and 3.32 were all obtained with the periodicity search on the same period range and with the same value of $\Delta\nu$ in order to simplify a comparison among them. For this comparison, the L values (shown in Figures 3.31 and 3.32), and probabilities assessed to them, were

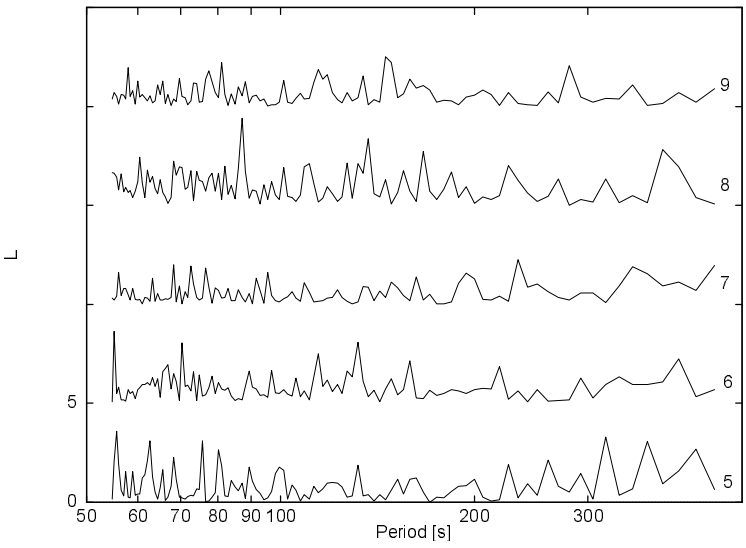

Figure 3.32: L statistic for data sets No. 5 to 9, on the period range 55s to 500s. The scale on the x-axis is logarithmic. Consecutive curves are shifted upwards to show them all in one Figure, and labels "0" and "5" on the y-axis indicate the scale.

multiplied. The resulting L- and probability-product graphs are shown in Figures 3.33, 3.34 and 3.35. Multiplication should only test the persistence of a periodicity. One can believe that if a certain periodicity is present in all, or at least in some, data sets, then there should be a maximum in the L-statistic product at this period. We can note a strong peak at the period 60s in the upper curve of Figure 3.33. We attribute the large product values at larger periods (>300s[14]) to chance enhancements due to the quasiperiodic changing of seeing (compare the 1/f-shape of the Lomb periodograms). In the middle curve of Figure 3.33, where only data obtained at 1.82m and 2.12m telescopes participate, there is a maximum at 60s, and another notable peak at 82s. The lower curve has the highest peak at almost 70s. Due to the doubts we have on the data obtained with 1.22m telescope (see footnote number 3 on page 34), we do not want to consider this peak too seriousely. Figures 3.34 and 3.35 are counterparts to Figure 3.33. Here, probabilities assesed to L statistics for data obtained at telescopes 1.82m&2.12m, and 1.22m, and for all data together, are multiplied. The absolute values of these probabilities as labelled on the y-axis of Figures 3.34 and 3.35 have no real meaning—they

[14]They appear at different periods >300s in all three curves shown in Figure 3.33, while the 60s peak appears at the same period in the upper and in the middle curve.

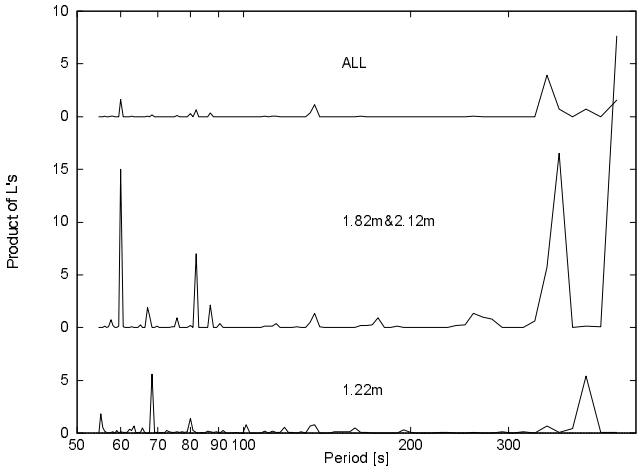

Figure 3.33: Product of L statistic for data obtained on 1.82m and 2.12m telescope (middle curve), and on 1.22m telescope (lower curve). The upper curve shows the product of L statistics for all the data together.

are naturally smaller if more spectra are included in multiplication. Again, we can note a peak at 60s in curves which are labelled by "ALL" and by "1.82m&2.12m". Here, the 82s peak has a comparable product probability as the 60s peak in the upper curve of Figure 3.34. In the curve labelled "ALL", the highest peak is at 134s, the peak at 82s is slightly lower than the 60s peak.

We now want to compare the results we have obtained by the epoch-folding of Crab data, to the results obtained in the same way, but with some other stars' data. For that purpose, we take seven data sets from the January 1998 observations, to make a comparison to the "1.82&2.12m" Crab pulsar results (see Figures 3.34 and 3.33), where seven L- or probability-curves were multiplied as well. We chose the following three brightest field stars after pulsar (stars designated by numbers 7, 2, and 3 in the photometry reduction files), and took data sets from three nights for stars 7 and 2, and from one night for star 3, to have seven data sets together. Figure 3.36 shows the L-statistic curves for these seven stars. The same period interval was searched (50s to 500s), and the same frequency increment was taken as for the pulsar data epoch-folding described before. If we compare Figure 3.36 to Figure 3.31, we can see that at different periods, peaks with relatively large value of L can appear randomly in any stars' signal. In particular, we can see a strong peak at about 70 seconds in the first and the fourth curve from bottom to top. These two curves are signals of stars number 7 and 2, from the same

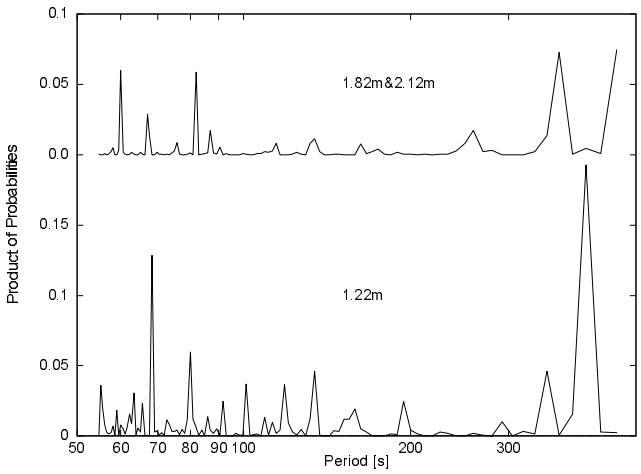

Figure 3.34: Product of probabilities for data obtained on 1.82m&2.12m telescope (upper curve), and on 1.22m telescope (lower curve).

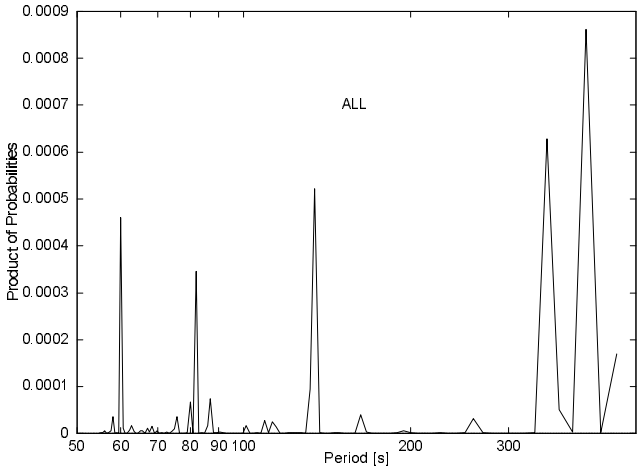

Figure 3.35: Product of probabilities for all pulsar data.

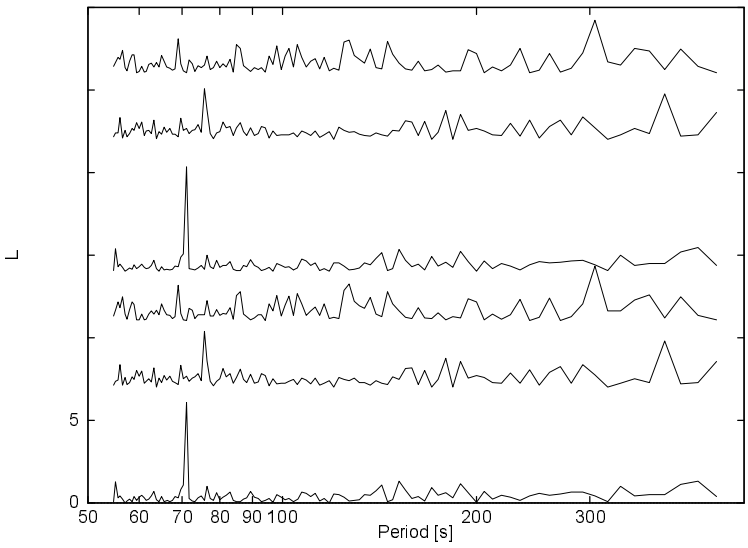

Figure 3.36: L statistic for data sets of seven field stars, on the period range 55s to 500s. The scale on the x-axis is logarithmic. Consecutive curves are shifted upwards to show them all in one Figure, and labels "0" and "5" on the y-axis indicate the scale.

night. The product of L's and of probabilities of these seven stars is shown in Figures 3.37 and 3.38. In these two Figures, corresponding products of seven pulsar signals (obtained on 1.82m and 2.12m telescopes) are shown again as well. We can see that the 60s peak in pulsar data is far stronger than any randomly enhanced peak in the seven field stars' data. Even at 70s, where a very high peak is present in two L-curves (see Figure 3.36), the product value is still more than ten times smaller than the corresponding value at 60s in pulsar L-product curve. This comparison shows that the epoch-folding of randomly selected data sets of other field stars do not show any periodicities whose significances could be compared to the significances of periodicities revealed by the epoch-folding of pulsar data.

Now we further consider the pulsar data epoch-folding results which are listed in Table 8. All of the peaks whose periods are cited in Table 8, except the one belonging to data set No. 13, have L's which satisfy the condition $L > \langle L \rangle + 2\sigma_L$. Their probabilities depending on the period value (the third column of Table 8) are shown in Figure 3.39. Each point is labelled by the same number as the corresponding observation in the first column of Table 8. The larger number means that the observation was obtained at a later time. We can see that there is no ordered temporal distribution of periods

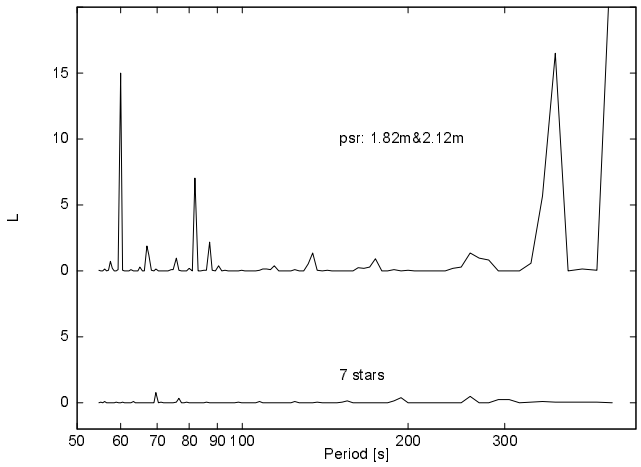

Figure 3.37: Product of L's for the seven field stars data sets (lower curve), and for seven pulsar signals, obtained by 1.82m and 2.12m telescopes (upper curve).

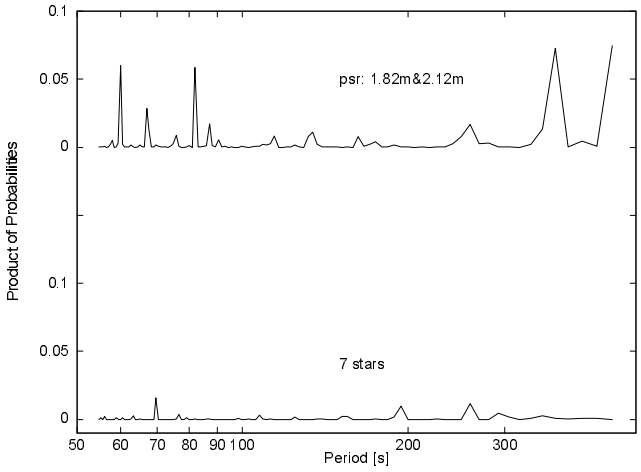

Figure 3.38: Product of probabilities for the seven field stars (lower curve) data sets, and for seven pulsar signals, obtained by 1.82m and 2.12m telescopes (upper curve).

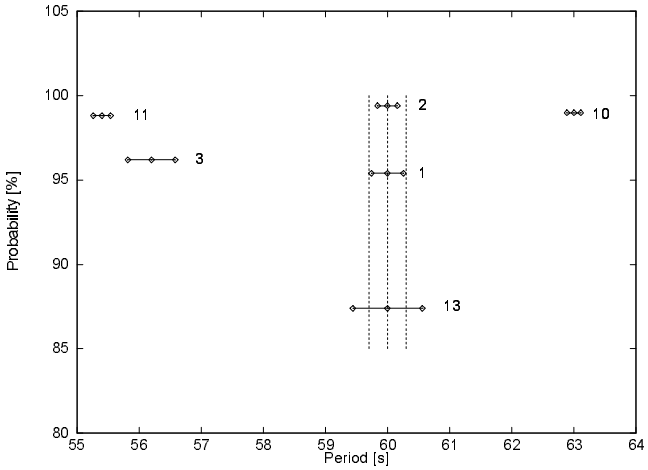

Figure 3.39: Peaks probabilities and periods from Table 4. The dotted vertical lines show the average period (of data sets No. 1, 2, and 13) and its errorbars.

in the sense that a period would e.g. increase with time. The results which are marked by an asterisk (*) in Table 8 are not shown in Figure 3.39. We can see in Figure 3.39 that three values (data sets No. 1, 2, and 13) show the same period inside their errorbars. With these three overlapping results, the resulting modulation period is obtained

$$P'_r = (60.0 \pm 0.3)s$$

or expressed as frequency

$$\nu'_r = (0.01667 \pm 0.00009)s^{-1} \tag{3.20}$$

The average resulting frequency value and its accuracy were calculated with data from Table 8, in the same way as it was done in the Lomb periodogram analysis in section 3.3.

Next we concentrate on these three sets (No. 1, 2 and 13) of data which have, inside errorbars, the same periodicity revealed by the epoch-folding technique. We want to fold them all together, because we expect that the 60s peak height will be increased in this way. We do not have information on the absolute phase of the 60s-periodicity in an individual data set, so we can only glue data sets together with an appropriate time lags between them. Therefore, we do phase-folding of the composed data set so that we take data set No. 1 and glue to it data set No. 2 with a time lag of 0 bins, 1 bin, 2 bins and 3 bins. For the trial period 60s folded into 4 bins, one bin means a 15 seconds time lag. Of these four phase-folding procedure results,

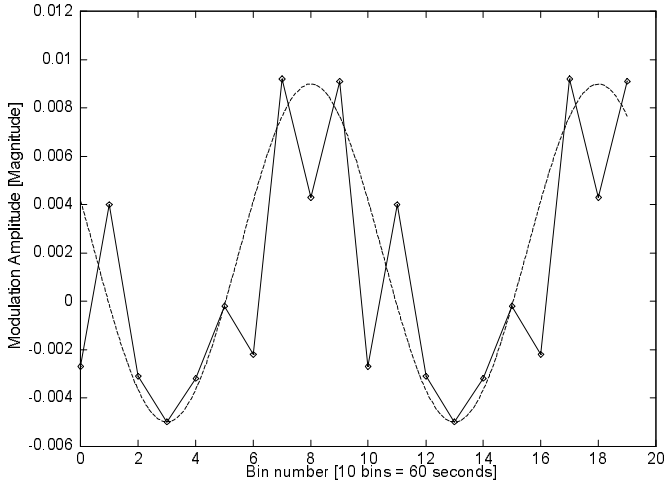

Figure 3.40: The shape of the 60s-periodicity modulation, obtained with phase-folding of data sets No. 1, 2, and 13 glued together. The amplitude of the fitted sine curve is 0.007 magnitude.

we select the one giving the maximal value of L at the period 60s. With data sets No. 1 and 2, we obtain the maximum with the time lag 30s. The corresponding L is 4.76, and the probability 99.73%. Next we glue to this composition (data set No. 1 plus data set No. 2, glued together with the time lag 30s) the data set No. 13, and again check all four possibilities for time lags. We obtain the maximal value of L, 6.39, with the time lag 45s. The corresponding upper limit for the probability is 99.97%. We can clearly see that if we phase-fold together all data sets which show periodicity at the same period, the probability that the periodicity is present in the data is, as expected, correspondingly enhanced.

With the phase-folding of three data sets glued together with appropriate time lags, as described in the previous paragraph, we can also try to obtain the shape of modulation at 60s. It is shown in Figure 3.40. To obtain the shape in more details, the phase-folding of the glued data set was done with 10 bins. In Figure 3.40, two periods are shown for clarity, which means that the value at x=10 on the x-axis is equal to the value at x=0, and so on. A sine curve $y = y_0 + Y sin\frac{2\pi(x-x_0)}{P}$ is fitted to the modulation shape (broken line in the Figure) with parameters $P = 10$, $Y = 0.007$ magnitude, $y_0 = 0.002$ magnitude, $x_0 = 4.5$. The amplitude of modulation at 60s is

$$A'_{\mathrm{mod}} = (0.007 \pm 0.0015)\ magnitude \tag{3.21}$$

where its accuracy is the statistical variation of all data points included in

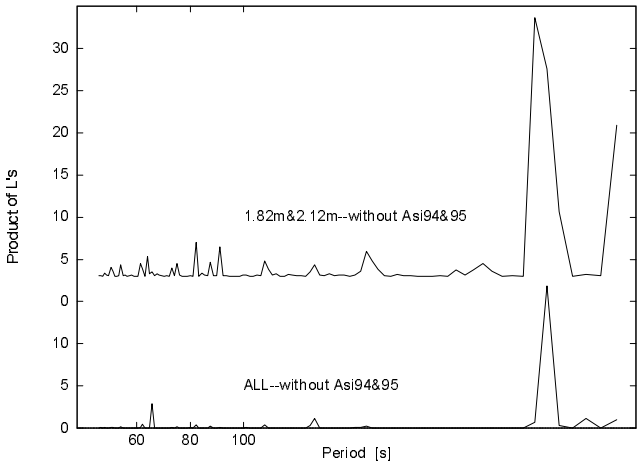

Figure 3.41: Product of L's for data obtained at 1.82m and 2.12m telescope, and for all data, but without data sets No. 1 and 2.

the phase-folding.

It is obvious from Table 8 and Figures 3.31 and 3.32 that except for data sets No. 1 and 2, no other data set has a notable peak at 60s. To check whether only these two peaks make the high peak at 60s in products of either L's or probabilites (see Figures 3.33, 3.34 and 3.35), we make another multiplication without data sets No. 1 and 2. The results are shown in Figures 3.41 and 3.42. Here, no more maxima, or at least notable peaks, can be observed at 60s. We may therefore conclude that the new data do not contribute significantly to the periodicity at 60s which was observed in data obtained in 1994 and 1995, and in the HST data from 1991. This conclusion agrees with the conclusion of section 3.3.

3.6 Does the Pulsar Magnitude Contain Enhanced Noise?

For statistical purposes, the noise content in pulsar magnitude is compared to the noise content of other field stars' magnitudes. We have already observed in Asiago 1994 data (Čadež and Galičič 1996 [11]) that pulsar's magnitude contains more noise than it should as compared to other field stars' magnitudes. An analysis is presented here for three of the latest (1998) observations. In particular, we compare the pulsar Fourier spectra to spectra of other four field stars, the statistical variance of pulsar's magnitude to sta-

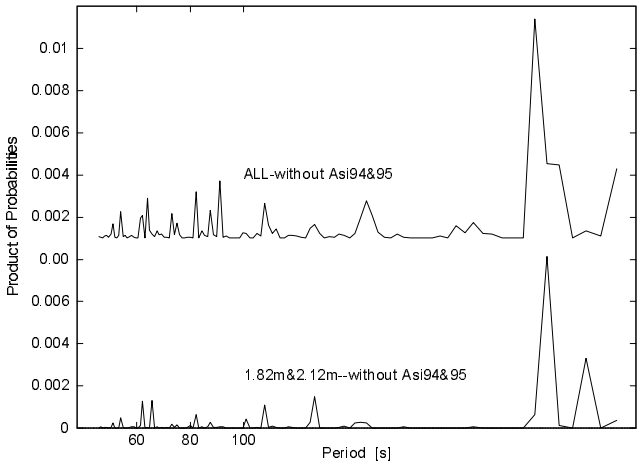

Figure 3.42: Product of probabilities for data obtained at 1.82m and 2.12m telescope, and for all data, but without data sets No. 1 and 2.

tistical variances of other field stars' magnitudes, and the spectral power of pulsar's signal to the spectral power of the field star number 7. This star is the second brightest star in the image, it is only 0.4 magnitude fainter than the pulsar when pulsar is brightest (see section 2.2). Since it is fainter, its magnitude should be slightly noisier than pulsar's. We have no equally bright star to compare, therefore we make an "upper limit" estimate for pulsar if we claim that the two should show comparable noise levels.

Figure 3.43 shows Fourier spectra (spectral amplitude against spectral frequency) of five field stars observed on 24/25 January 1998. Horizontal lines over each spectrum show the average Fourier amplitude $\langle A_{FT} \rangle$, and the two following $+1\sigma$ amplitude levels. The statistical variance of spectral amplitudes σ_A is defined as $\sigma_A = \sqrt{\langle A_{FT}^2 \rangle - \langle A_{FT} \rangle^2}$, where only spectral amplitudes at frequencies $\geqq 0.003Hz$ are included. We can see that the majority of peaks in all spectra falls into the range $\lessapprox \langle A_{FT} \rangle + 2\sigma_A$. The order of spectra from bottom to the top of Figure 3.43 agrees with the order of stellar brightnesses: star number 1 (pulsar) is the brightest, and star number 6 is the faintest one[15] in the image. We can immediately notice that although the pulsar is brighter than the star number 7, its spectrum has a higher noise level and a wider $1\sigma_A$ band.

Next we compare the Daophot magnitude error, and the actual statistical

[15]The numbers of stars (labelling on the right side of Figure 4.3) refer to the order of stars in the photometry reduction files and have no other meaning than the naming of stars.

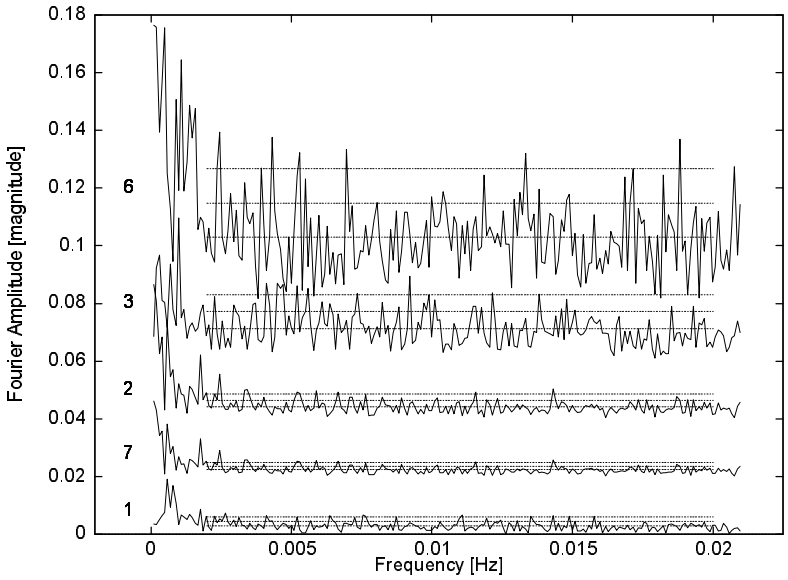

Figure 3.43: Observation 24/25 January 1998: Fourier spectra (Fourier amplitude in magnitudes against frequency in Hz) of 5 field stars. Images number 54 to 483 (430 consecutive images) are included in the analysis for all five stars. Pulsar's spectrum is labelled by number 1 on the left side of the Figure.

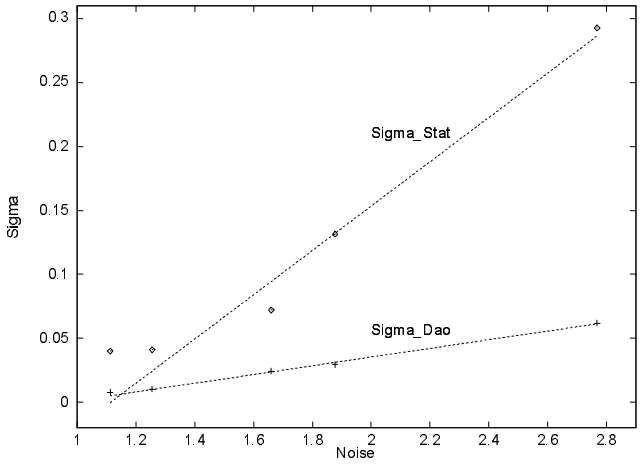

Figure 3.44: Average magnitude accuracy (Sigma_Dao), and magnitude statistical variance (Sigma_Stat), against the expected magnitude variance estimated on the basis of the average magnitude, for five field stars (observation 24/25 January 1998). The left-most two points (diamond and cross) belong to the pulsar.

variance of pulsar's and other field stars' magnitudes, to the expected value of their noise. By "noise" we mean the accuracy at photon counting according to Poisson statistics (Galičič 1995 [20]). For each star, we determine it with the average (calibrated Daophot) magnitude value $\overline{m} = \frac{1}{N}\sum_{i=1}^{N} m_i$, so that "Noise" $\propto \frac{\sqrt{N_{Phot}}}{N_{Phot}} \propto \frac{\sqrt{j}}{j} = \frac{1}{\sqrt{j}} = 10^{0.2\overline{m}}$, where N_{Phot} is the number of counted photons. This is shown on the x-axis ("Noise") of Figure 3.44 for five field stars observed on 24/25 January 1998. On its y-axis, labelled "Sigma", the average magnitude accuracy as given by the Daophot, Sigma_Dao (crosses), and the statistical variance of magnitudes, Sigma_Stat $= \frac{1}{N-1}\sum_{i=1}^{N}(m_i - \overline{m})^2$(diamond dots), are given. The average stellar magnitudes as well as their Sigma_Dao and Sigma_Stat are calculated for the same set of consecutive N images that were Fourier analyzed (Figure 3.43 and corresponding Figures for other data sets). Two lines are drawn through diamond dots and crosses, respectively, but points corresponding to the pulsar (the most left points) were not included in the line fits.The accurate alignment of all crosses on the fitted line, of course, only proves that Daophot gives the right values for magnitude errors, which is not surprising since it calculates the errors from the counted number of photons[16], according to eq. (2.1). It is shown here only as a comparison for the upper line (Sigma_Stat). In the upper line, we can see that the pulsar's point (the most left diamond) significantly deviate from the line fit.

Figures 3.45 and 3.46 show the Fourier spectra of magnitudes of five filed stars, and the above described "Sigma" curves, correspondingly, for the observation from 22/23 January 1998, and Figures 3.47 and 3.48, correspondingly, for the observation from 23/24 January 1998. The same 5 stars as for the observation from 24/25 January 1998 were examined in both cases.

We can see that all three groups of Fourier spectra, and all three "Sigma" graphs, are very similar, respectively. In Sigma_Stat lines, the two points on the left side deviate more from the line than the points on the right side. Of the two leftwards points, the one that belongs to pulsar deviates from the line fit even notably more than the other point, which belongs to the second brightest star (number 7).

We want to know how much does pulsar's Sigma_Stat deviate from the fitted line (the fitted value is labelled by Sigma_Stat_Fitted) as compared

[16]The average magnitudes are normalized magnitudes m, which means that the flux density calculated from them, j=$10^{-0.4m}$, is the absolute flux density (in J/m^{2}s) divided by a constant C$10^{0.4M}$, where M is the magnitude corresponding to the normalizing flux, and C takes care for physical units. This explains why the line Sigma_Dao does not have a unit slope.

Besides the photon counting statistics (of stellar and sky photons), also the contribution of read-out-noise is taken into account in calculation of Sigma_Dao, see eq. (2.1).

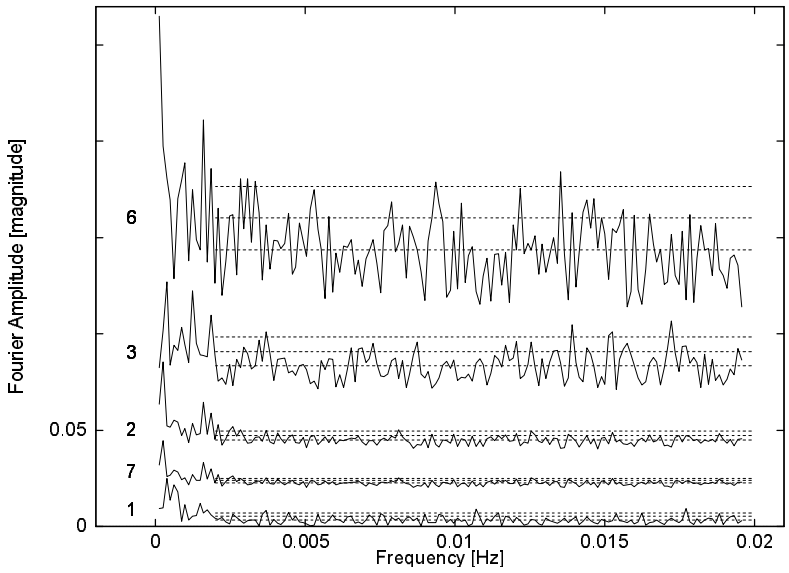

Figure 3.45: Observation 22/23 January 1998: Fourier spectra (Fourier amplitude in magnitudes against frequency in Hz) of 5 field stars. Images number 200 to 520 (321 consecutive images) are included in the analysis for all five stars.

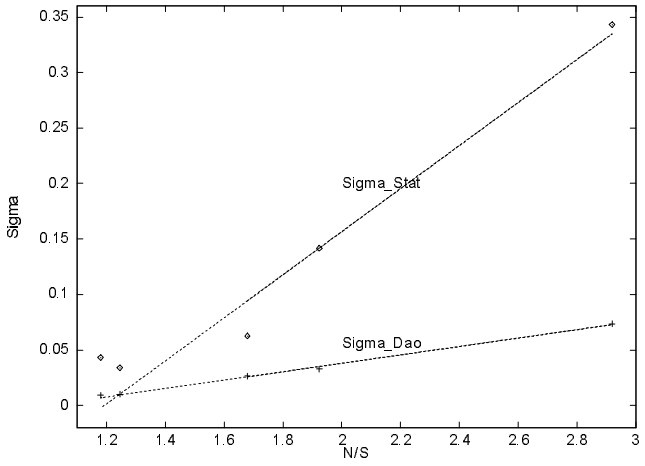

Figure 3.46: Average magnitude accuracy (Sigma_Dao), and magnitude statistical variance (Sigma_Stat), against the expected magnitude variance estimated on the basis of the average magnitude, for five field stars (observation 22/23 January 1998). The left-most two points (diamond and cross) belong to the pulsar.

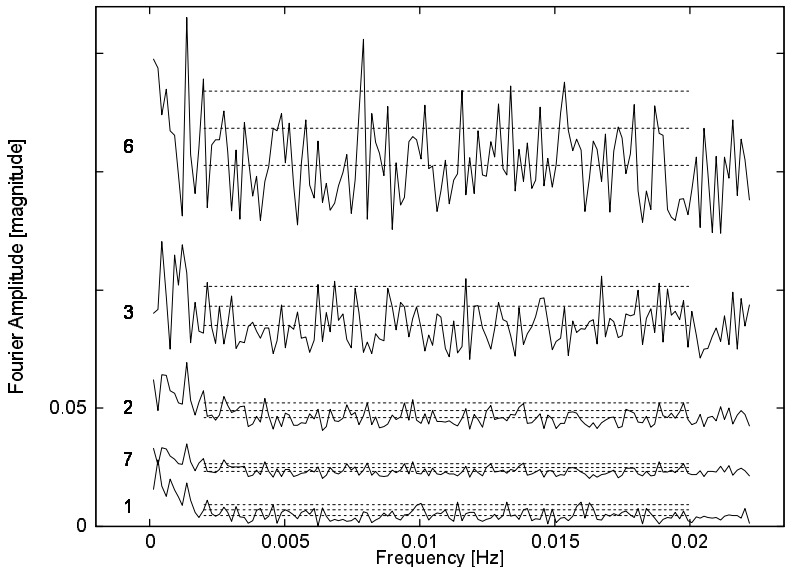

Figure 3.47: Observation 23/24 January 1998: Fourier spectra (Fourier amplitude in magnitudes against frequency in Hz) of 5 field stars. Images number 1 to 295 (294 consecutive images) are included in the analysis for all five stars.

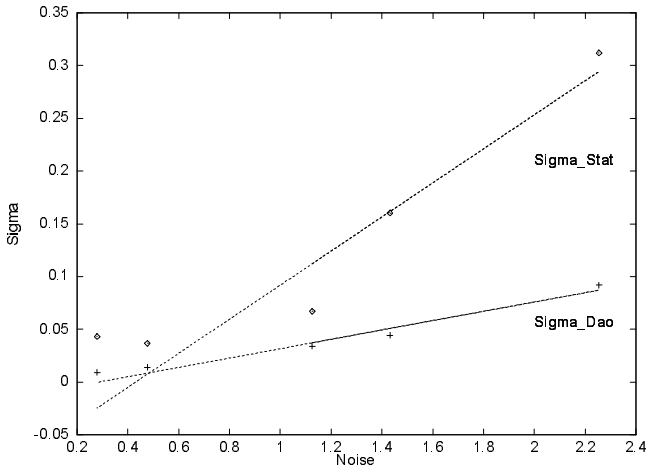

Figure 3.48: Average magnitude accuracy (Sigma_Dao), and magnitude statistical variance (Sigma_Stat), against the expected magnitude variance estimated on the basis of the average magnitude, for five field stars (observation 23/24 January 1998). The left-most two points (diamond and cross) belong to the pulsar.

to the deviation of star number 7's Sigma_Stat. The values of the ratio

$$\frac{(\text{Sigma_Stat} - \text{Sigma_Stat_Fitted})_{psr}}{(\text{Sigma_Stat} - \text{Sigma_Stat_Fitted})_7}$$

are 1.9, 2.3 and 2.5 for observations from 22/23, 23/24, and 24/25 January 1998, respectively.

We may conclude that pulsar's magnitude contains more noise than magnitudes of other field stars, on the basis of the hypothesis that the noise of a non-variable star brightness is predominantely white, and that its origin is the same for all field stars. There may be a phenomenon that we are not aware of, either connected to pulsar's optical pulsations, or to our observational method, for this higher than expected noise. One possiblity to explain it is the presence of a (periodic) modulation of pulsar's optical pulsations.

We will now estimate the excess noise in pulsar's signal as compared to the signal of the star number 7, so that we will compare their spectral powers. We define the spectral power P as a sum of spectral amplitudes squared[17]. Only amplitudes at spectral frequencies $\geqq 0.003Hz$ will be taken in account, which is the same frequency limit we used for calculations of Fourier spectra statistics all along Chapter 3. The results of the comparison are shown in Table 9 below. In the first column, the observation is labelled by its double date. In the second column, the ratio of pulsar's spectral power to the ratio of the star number 7's spectral power, P_p/P_7, and in the third column the difference of the two, $P_p - P_7$, are given, respectively. In the fourth column, the difference written in the third column is compared to the power of the sine signal Fourier spectrum, P_{sin}, $R = (P_p - P_7)/P_{\text{sin}}$. The sine signal was generated at the data points times, its amplitude is 0.0065 magnitude. We can see that the excess power in the pulsar signal as compared to the signal of star number 7, is more than an order of size larger as it would have been if it was due to a single periodic modulation with the amplitude 0.0065 magnitude. On the other hand, we want to know what would need to be the sine signal amplitude A_{sin} if the power $P_1 - P_7$ was due to a single sine signal. The result is written in the last column of Table 9. On average, we can see that this amplitude would be about 5 times more than 0.0065 magnitude, or about 0.03 magnitude.

[17]Since spectral amplitudes are given in magnitudes, the power "unit" is magnitude squared. But since magnitude is not a physical unit, P's given in Table 9 have no units.

Observation	P_p/P_7	$P_1 - P_7$	R	$A_{sin}[magnitude]$
24/25 Jan. 98	1.5	$6{\cdot}10^{-4}$	14.2	0.024
23/24 Jan. 98	2.2	$21{\cdot}10^{-4}$	49.8	0.046
22/23 Jan. 98	1.9	$9{\cdot}10^{-4}$	21.6	0.030

Table 9: Comparison of pulsar's and star number 7's spectral powers.

In pulsar data, we do not see such a strong periodic signal. We therefore conclude that the excess power is contained in the pulsar's signal if we compare its spectral power to the spectral power of star number 7, but this excess is not due to a single periodic signal that we would clearly extract from noise with the methods of analysis we applied in sections 3.3. and 3.5.

Chapter 4

Conclusion

Several years long efforts devoted to precise optical stroboscopic observations of Crab pulsar were described above. The stroboscopic set-up was developed in our laboratory. Observations were carried at our small telescope of AGO first, then at the Italian 1.22m and 1.82m telescopes in Asiago and atop Cima Ekar, respectively, in the years from 1993 to 1997. In 1998, we observed at the Mexican 2.12m telescope atop Mariquita mountain in the Cananea region.

We have analyzed Crab pulsar data with two different methods, to search for possible periodicities in period interval from about 40s to a few minutes. Both methods, Lomb periodogram (Fourier) method, and phase-folding technique, give—within errorbars—the same result: the modulation period is 60s, and the modulation amplitude is 0.006 magnitude. Mostly, the old data contribute to the obtained result, but the new data do not contradict it. In Figures 4.1 and 4.2, the 60s-periodicity frequencies and amplitudes as obtained with the two methods of analysis are shown graphically. With solid lines, the resulting frequency (amplitude) is shown for both methods of analysis, and its errorbar belts are indicated by dotted lines. We can see that both methods results do overlap. Additionally, we cross-correlated Lomb periodograms and estimated probabilities that the peak at frequency 1/60s in obtained cross-correlation functions is not due to chance enhancements. Altogether, we estimate that the probability that the peak at 1/60s is due to chance enhancement is not larger than 3%, which is the upper limit, while analysis of some individual data sets (see section 3.5) and cross-correlations of some pairs of spectra (see section 3.4) give an even much smaller probability that the peak would appear by chance, of (much) less than one percent.

We have to stress again that strong peaks at 60s are detected only in 1994 and 1995 stoboscopic data, and in 1991 HST data, which all belong to the old data group. Other stroboscopic data (new data), which have higher noise levels, do not contribute significantly to the result. The epoch-folding

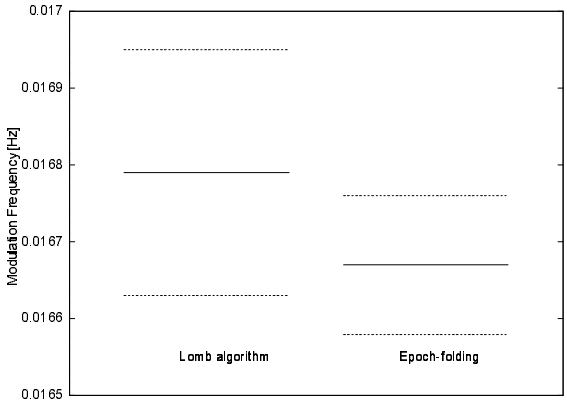

Figure 4.1: Modulation frequency: Comparison of results of Lomb algorithm and phase-folding.

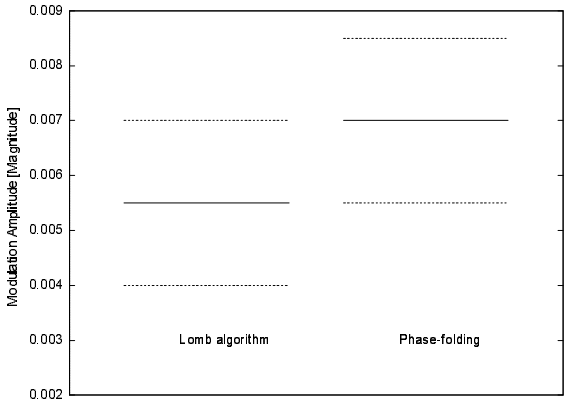

Figure 4.2: Modulation amplitude: Comparison of results of Lomb algorithm and phase-folding.

method has pointed to the possibility of presence of two other periodicities in pulsar's data, the periods are about 82s and 134s. Also the persistent presence of peaks at periods $\gtrsim 300s$ in L-product of pulsar data which we have explained as possibly due to seeing in section 3.3, is put under question here, since it was not observed in the L-product of other field stars data. These periodicities were not considered in detail here because they were not confirmed by the Lomb spectra and by the cross-correlations of Lomb spectra.

There are a few possible explanations why we do not observe the 60s-modulation in all data sets. First, the periodicity was present and is still there, but was not confidently detected with the new noisier data. Second, the 60s-periodicity was present in 1991, and in 1994–1995 observations, but is not present any more in the new observations. Third, there is a small probability that the weak 60s-periodicity measured with "old data", is a statistical fluctuation. The most difficult argument to refute here is the fact that different analyses of different data obtained in different ways and at different times (HST high speed photometer data from 1991, stroboscopic data from 1994/95) consistently reveal the periodicity. It is clear that the presence of the 60s-periodicity in Crab pulsar optical pulsations requires one of the world's largest mirrors to look at.

The 60s-periodicity could be explained as the free-precession of a flattened rotating neutron star. Unlike the majority of pulsar observers who try to explain very long (quasi)periodicities in pulsar signals by free-precession, we estimate that the free-precessional frequency of Crab pulsar should be about one minute. A rotating polytropic model which explains both the 60s-periodicity of Crab, and the Her X-1 35-day cycle, as the free-precession of a neutron star, is described in (Čadež et al. 1997 [12]). For both systems, we find that the same equation of state (of neutron star matter) can describe the observed periodicities.

Besides the significant probability that the 60s-periodicity is present in Crab pulsar optical pulsations, one of the major achievements of five years of stroboscopic observations is that we had considerably lowered the upper limits of Crab pulsar optical (non)variability on short time-scales. If we consider all the data together, and exclude the weak 60s-periodicity which we did not manage to confirm beyond any doubts, we may conclude that there is no permanent significant variability at the level $\lesssim 0.003$ magnitude (or about 0.3%) on time scales 40s to a few minutes. This sensitivity is at least 10 times better than the previously reported short time-scales limit of 5% (Kristian 1971 [31]), and was achieved by $\sim 2m$ telescopes at non-optimal observing conditions. The sensitivity might be considerably improved if the stroboscopic system was used with a larger telescope and at favorable observing conditions.

The stroboscopic observational set-up, or briefly the chopper system, offers plenty future possibilities in pulsar astronomy. It is a unique device which could successfully be used for the following future projects:

• Crab pulsar. With a larger telescope and a longer continuous observing run, the Crab pulsar optical pulsations stability, or possibile periodicities, particularly the 60s-periodicity, could be examined with better accuracy.

• Vela and other (high-energy) pulsars. Other optically (high-energy) detected pulsars, preferably Vela pulsar, could be observed in the same way as Crab.

• Spectral analysis of pulsed optical light output. Chopper offers a unique possibility to observe only a selected part of the pulsar's pulse, e.g. its main pulse, or its subpulse at once. With the chopper and a spectroscope, spectra of both pulse components, which supposedly originate from the opposite pulsar poles in the case of Crab, can be observed separately. Due to our knowledge, such spectra have not been obtained before. A few trial spectra of Crab's main pulse were taken in Cananea in January 1998, and some more of both pulse components in December 1998 by A. Čadež, A. Carramiñana and T. Zwitter.

• Optical pulsar timing. The chopper system could be used for optical timing which would be of a special importance as a comparison for pulsars which are regularly timed in radio or in X-rays, and to provide (reference) ephemeris for the radio quiet pulsars (e.g. Geminga).

• Optical pulsars survey. With the appropriate selection of pulsars with known pulsation (rotation) frequencies (in the accessible chopper's angular velocity range), a search for optical pulsars could be run with a middle-size ($\approx$2m) telescope (A. Carramiñana, private communication, 1998).

• Pulsar thermal emission. Chopper is also an excellent device to cut out the pulsed emission, and measure the pulsar's black body emission. No need to stress that a very large telescope and excellent observing conditions would be needed for that.

Bibliography

[1] Agrinier, B. et al, ApJ, **355**, 645-650, 1990

[2] Alpar et al., ApJ, 276, **325**, 1984

[3] Alpar, A., Ögelman, H., A&A, **185**, 196-202, 1987

[4] Alpar, A., in *Timing Neutron Stars*, Kluwer Ac. Publishers, Dordrecht, 1989

[5] Bell, J. F., Radio Pulsar Timing, COSPAR, 1997

[6] Boxenberg, A. et al. *Astronomical Almanac 1998*, Washington: US Government Printing Office; London, HMSO, 1998

[7] Bronštejn, J. N. Semendljajev, K. A. *Matematični priročnik*, Tehnična založba Slovenije, Ljubljana, 1980

[8] Burnham, R. *Burnham's Celestial Handbook*, Dover Publications, New York, 1987

[9] Carramiñana, A. et al. A&A, **290**, 487-495, 1993

[10] *CCD Camera Manual*, Wright Instruments Ltd, August 1990

[11] Čadež, A. and Galičič, M., A&A, **306**, 443-448, 1996

[12] Čadež, A., Galičič, M., Calvani, M. A&A, **324**,1005-1009, 1997

[13] Čadež, A. and Galičič, M., Poster at the conference *Science with the Hubble Space Telescope*, Paris, 1995

[14] Čadež, A. and Galičič, M., in *Pulsars: Problems and Progress*, IAU Colloquium 160, Astron. Soc. of the Pacific, San Francisco, 1996

[15] Davies, S. R., MNRAS, **244**, 93-95, 1990

[16] Eikenberry, S. et al, ApJ, **477**, 465, 1997

[17] Lyne, A. G. et al., Crab Pulsar Timing Results, Monthly Ephemeris, 1994-1997

[18] Foster, R. S., in *Pulsars: Problems and Progress*, ASP Conf. Series, Vol. 105, 1996

[19] Galičič, M. *Merjenje frekvence pulzarja PSR0531+21*, graduation thesis, Univerza v Ljubljani, Ljubljana, 1991

[20] Galičič, M. *Opazovanje spreminjanja optičnega izseva pulzarja PSR0531+21 na kratkih časovnih skalah*, MSc thesis, Univerza v Ljubljani, Ljubljana, 1995

[21] Goldstein, H., *Classical Mechanics*, Addison-Wesley Pub. Company, Reading, Massachusetts, 1980

[22] Goldreich, P., ApJ, **160**, L11-L15, 1970

[23] Guidoboni, C. et al., *The supernova of 1054 in two contemporary European chronicles*, XXIII ICRC. Calgary, Alberta, July 19-30 1993

[24] Glendenning, N. K. *Compact Stars*, Springer-Verlag New York, New York, 1997

[25] Gupta, Y. et al., ApJ, **403**, 183-201, 1993

[26] Hegyi, D., in *The Crab Nebula*, IAU Sym. No. 46, p129, 1971

[27] Helfand, D. J., Fowler, L. A., Astron. J., **82**, 701-705, 1977

[28] Huguenin, G. R., Taylor, J. H., ApJ, **181**, L139-L142, 1973

[29] Jones, P. B. et al., Nature, 1980

[30] Jones, P. B., MNRAS, **235**, 545-550, 1988

[31] Kristian, J., in *The Crab Nebula*, IAU Sym. No. 46, p87,1971

[32] LaBrecque, D. R., Astron. J., **198**, 1854-1859, 1994

[33] Lang, K. R., *Astrophysical Formulae*, Springer Verlag, Berlin, 1978

[34] Larsson, S., A&A Supp. Ser., **117**, 197-201, 1996

[35] Leahy, D. A., A&A, **180**, 275-277, 1987

[36] Leahy, D. A. et al., ApJ, **266**, 160-170, 1983

[37] Lipunov, V. M., *Astrophysics of Neutron Stars*, Springer Verlag, Berlin, 1992

[38] Lyne, A. G. et al., MNRAS, **265**, 1003-1012, 1993

[39] Lyne, A. G. and Graham-Smith, F. *Pulsar astronomy*, Cambridge University Press, Cambridge, 1998

[40] Nelson, J. et al., ApJ, **161**, L235-L244, 1970

[41] Percival et al. ApJ, **407**, 276-283, 1993

[42] Pines, D., Shaham, J., Nature, **245**, 77-81, 1973

[43] Pines, D., Shaham, J., Nature, **248**, 483-486, 1974

[44] Press, W. H., ApJ, **338**, 277-280, 1989

[45] Press, W. H. et al., *Numerical Recipes in C,* Cambridge University Press, Cambridge, 1992

[46] Press, W. H., *Numerical Recipes in Pascal,* Cambridge University Press, Cambridge, 1989

[47] Richards, D. W., Astrophy. J., **160**, L1-L6, 1970

[48] Rickett, B. J., Lyne, A. G., MNRAS, **244**, 68-75, 1990

[49] Shaham, J., ApJ, **310**, 780-785, 1986

[50] Smith, F. G., *Pulsars*, Cambridge University Press, Cambridge, 1977

[51] Smith, F. G. et al., MNRAS, **184**, 39-43, 1978

[52] Stetson, P. B., *User's Manual for Daophot II*, 1994

[53] Stetson, P. B., PASP, **99**, 191-222, 1987

[54] Stinebring, D. R., Condon, J. J., ApJ, **352**, 207-221, 1990

[55] Thompson, D. J. et al., in *Isolated Pulsars*, Cambridge Univ. Press, Cambridge, 1993

[56] Thorne, K. S., Gürsel, Y., MNRAS, **205**, 809-817, 1983

[57] *TrueTime Model XL-DC 151-600-110 Manual*, Serial Number 1750, September 25, 1995

[58] Ulmer, M. P., ApJ, **432**, 228-238, 1994

Appendix A

Variation of Seeing Over a Night

The average seeing over each night of observations was estimated in the following way. The photometry program Daophot lists the parameters of the modelled stellar profile (the *point spread function*). In our case, these are the Gaussian curve parameters, σ_x and σ_y. (In photometry practice, one rather thinks in terms of *FWHM, full width at half maximum*, or half of it, FWHM/2, than in terms of σ_x and σ_y, which are connected by the relation $FWHM/2 = \sqrt{2\ln 2}\ \sigma_{x(y)} = 1.18\sigma_{x(y)}$.) Here we will strictly use $\sigma_{x(y)}$ as a measure for the seeing disk semidiameter. Seeing given in Table 1 is the seeing disk diameter $2\sigma_x \approx 2\sigma_y$.

During the photometry reduction, we observed that FWHM/2 did vary considerably during a single night. As an example, the temporal variation of values σ_x and σ_y are drawn in Figure A.1 for the night 24/25 January 1998. We can see that both parameters vary a lot during the night, and that in general they vary in correlation while locally (on shorter intervals, particularly from one image to another), they may be anticorrelated. (Note that the upper curve which shows σ_y is shifted for 4 pixels so that the value 8 for the lower curve means 4 for the upper one.) The lowest curve in the picture shows the ratio of both Gaussain curve widths, σ_x/σ_y, so it is dimensionless, but shown in the same Figure for brevity. The average value of this ratio over all images is 1.00 while there seem to be a slight (linear) trend from the evening to the morning since the average value over images $<$280 is 1.10 while it is 0.84 for images $>$800. Except of this slight trend we can conclude that stellar profiles are approximately round on average.

Examination of individual images shows that usually σ_x and σ_y do differ, i.e. a typical Gaussian curve's overcut is an ellipse and not a circle. For Cananea observations, this difference is typically 0.5 to $\gtrapprox$1 pixel at $\sigma_{x(y)} \approx 6$

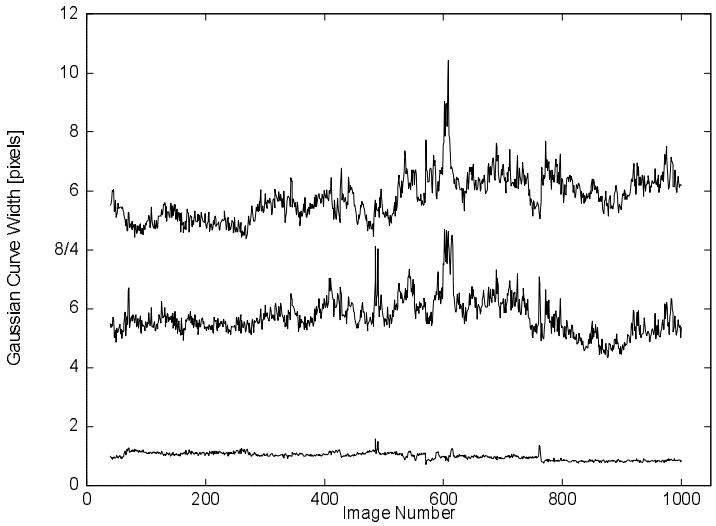

Figure A.1: Parameters of Gaussian curves fitted to the stellar profile of every image over the night 24/25 January 1998. The middle curve: σ_x, the upper curve: σ_y, in pixels. The lower curve shows the ratio σ_x/σ_y.

pixels. For Asiago 1994 observations, the difference is smaller, ≈ 0.5 pixel at $\sigma_{x(y)} \approx 4.3$ pixels. The main advantage in terms of more stable image-to-image values of σ_x and σ_y in Asiago images may be due to the fact that there are a few stars on every image that are brighter than pulsar, and more stars that can be used as PSF stars as well. The principal PSF star in Cananea images is the pulsar, while the remaining few field stars are fainter than the pulsar. The latest (Cananea) seeing observations were analyzed in more detail because the relatively strong varying of FWHM/2 led us to speculate whether this changing might have contributed to the higher than expected noise level in pulsar's magnitude curve. One would expect that in normal observing conditions, both σ_x and σ_y would change approximately in the same manner since the atmosphere cells should not show strong anisotropy. To test the expectation, the Pearson's correlation coefficient r (Press 1989 [45])

$$r = \frac{\sum_i (x_i - \overline{x})(y_i - \overline{y})}{\sqrt{\sum_i (x_i - \overline{x})^2}\sqrt{\sum_i (y_i - \overline{y})^2}}$$

was calculated with $x = \sigma_x$, $y = \sigma_y$, $\overline{x} = \overline{\sigma}_x$, and $\overline{y} = \overline{\sigma}_y$. In Table 10, the average, minimal and maximal values of σ_x and σ_y, as well as their variances are given for all four Cananea observations. In the last column of Table 10, the value of r is given. The number in the first column is

the observation's label[1] (the same as in Chapter 3). For each observation, there are two lines in Table 10 of which the first one gives the values in pixels while the second one gives them in arcseconds. For conversion, the separation between pulsar and next-to-pulsar star was calculated in pixels by using both stars' rectangular coordinates from the Daophot photometry file, and the value for this separation in arcseconds is $5.7''$ (Burnham 1987 [8]).

No.	$\overline{\sigma_x}$	$Vari_{\overline{\sigma_x}}$	$\sigma_{x\,\max}$	$\sigma_{x\,\min}$	$\overline{\sigma_y}$	$Vari_{\overline{\sigma_y}}$	$\sigma_{y\,\max}$	$\sigma_{y\,\min}$	r
10	5.9	0.5	8.2	4.6	6.0	0.7	9.4	4.6	0.68
	1.20	0.1	1.7	0.9	1.21	0.15	1.9	0.9	
11	5.5	0.8	9.0	3.9	5.9	0.6	8.2	4.5	0.5
	1.1	0.2	1.8	0.8	1.2	0.12	1.7	0.9	
12	5.7	0.6	8.7	4.3	5.8	0.7	10.4	4.4	0.49
	1.16	0.16	1.8	0.9	1.18	0.15	2.1	0.9	
13	5.3	0.9	12.8	3.8	5.3	0.7	7.9	3.9	0.66
	1.07	0.19	2.6	0.8	1.08	0.14	1.6	0.8	

Table 10: Stellar profile parameters for Cananea observations.

There are a few interesting points to be noted in Table 10. First, although the values of σ_x and σ_y, as mentioned before, notably differ in every single image, their average values are the same for every night. This can at simplest be understood in the following way. Both values are the same, but some phenomenon changes them stohastically, with the same amplitude of change. The image-to-image differences may be explained when one takes in account that although a typical exposure time of these images is $\sim$15 seconds, the effective exposure time—chopper effectively allows CCD chip to be exposed for 1/10 of the time—is only $\sim$1.5s. In this short time, the stellar profile may not be well averaged as far as the changing of diffraction pattern due to the moving of atmospheric cells is concerned. Therefore, we may believe that on short time scales, the variations of σ_x and σ_y as Daophot sees them are real, while their influence on photometry quality could not be easily eliminated, or even estimated. To worsen the problem, there are very few stars in the small field of view on Cananea images.

[1]Data No. 11 were considered in two parts since there is a notable difference in the average values of σ_x and σ_y in the first part of the night comparing to the second part of the night. The corresponding values in Table 10 are the averaged values of both data parts.

Second, the two parameters are correlated, as expected (see Figure A.1 and Table 10). The correlation coefficient r is about 0.6 which does tell that the considered quantities are surely not uncorrelated, but the values of r are maybe less than expected. A comparison to the Asiago 1996 data' σ_x and σ_y shows that $Vari_{\overline{\sigma}_{x(y)}}/\overline{\sigma}_{x(y)}$ is less than 0.1 for Asiago 96 while it is up to 0.2 for Cananea observations. Also the ratio $\sigma_{x(y)\,\max}/\sigma_{x(y)\,\min}$ is about 1.5 for Asiago 96 while it is 2 to 3 for Cananea observations. This comparison tells that the quantitative differences as measured with changing of σ_x and σ_y, though they do exist, do not differ substantially for Asiago and Cananea observations. The difference in photometry quality can then be explained predominantly with the fact that due to a smaller field of view at Cananea images, there were less PSF (and calibration) stars for Cananea than for Asiago images. We can therefore conclude that in order to obtain better photometric results, a focal reducer should be applied for further observations in Cananea.

Appendix B

L-Statistic Probability Estimation

To assess the probability to any value of L-statistic obtained in the epoch-folding analysis, random numbers were generated at times of points of data set No. 12, which means that artificial 'magnitudes' were generated in 953 points so that the time interval between two points is equal to the corresponding value in the real data. The generated data were analyzed with the phase-folding software with the same number of bins (4) as the pulsar data were analyzed, to test for the presence of a 60s-periodicity in them[1]. The procedure was repeated 20000 times. With the resulting 20000 values of L, a histogram showing their number distribution was built. The histogram is shown in Figure B.1. The L-step in the histogram is 0.1. We can see that the larger the value of L, the smaller is the probability that this value would randomly appear. The ratio of the area of the histogram on the right of the chosen value L_0, A_{L_0}, to the total histogram area, A, $\frac{A_{L_0}}{A}$, is taken as the probability that a value $L \geqq L_0$ would appear randomly. Therefore, $\mathcal{P}_{MC} = 1 - \frac{A_{L_0}}{A}$ is taken as an estimation for the probability that the tested periodicity is present in the data if the value L_0 was obtained for phase-folding at the corresponding period. $\mathcal{P}_{MC}$ can be directly compared to $\mathcal{P}$ in eq. (3.18). Both values, $\mathcal{P}_{MC}$ and $\mathcal{P}$ are the same for any L within $\leq 0.5\%$. Apart from numerical errors, these differences may be due to the fact that eq. (3.18) takes in account also the number of data points. With the histogram in Figure B.1, probabilities $\mathcal{P}_{MC}$ for a few values of L were calculated and are written below.

[1] Testing with other trial periods gave the same results on average.

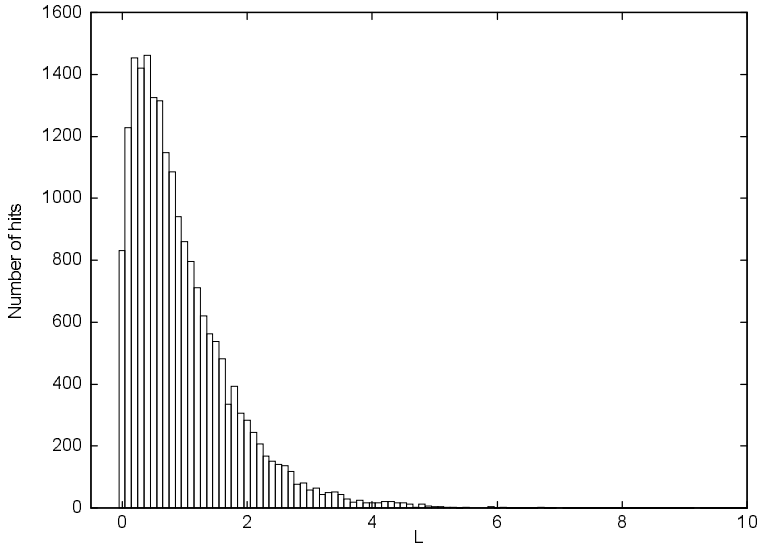

Figure B.1: Distribution of L values as obtained with the phase-folding method software, on 20000 randomly generated data sets. The same trial period (60s) was tested for every of the 20000 data sets.

L	$\mathcal{P}_{MC}$
1.0	0.65
1.5	0.81
2.0	0.90
2.5	0.95
3.0	0.97
3.5	0.987
4.0	0.992
4.5	0.997
5.0	0.9988
5.5	0.9993

Appendix C

Cross-Correlation Functions

In this Appendix, the remaining 36 cross-correlation functions are shown, which together with the 15 shown in section 3.4 make the 51 cross-correlation functions which have notable peaks around frequency 1/60s.

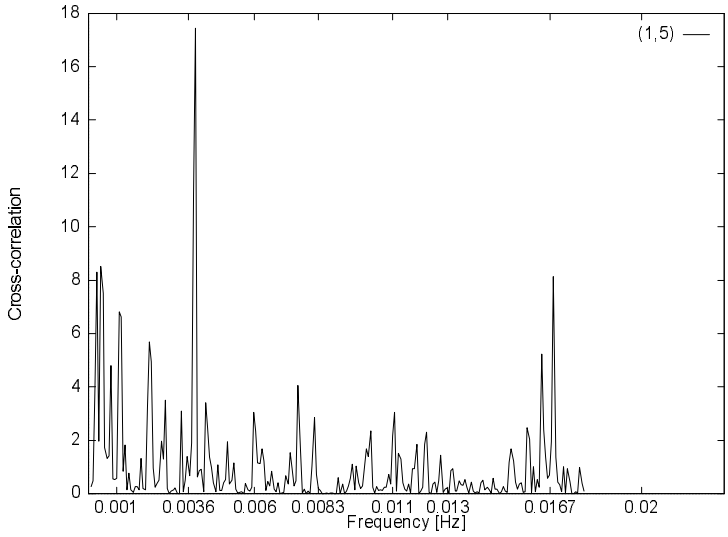

Figure C.1: Cross-correlation: Data sets No. 1 and 5.

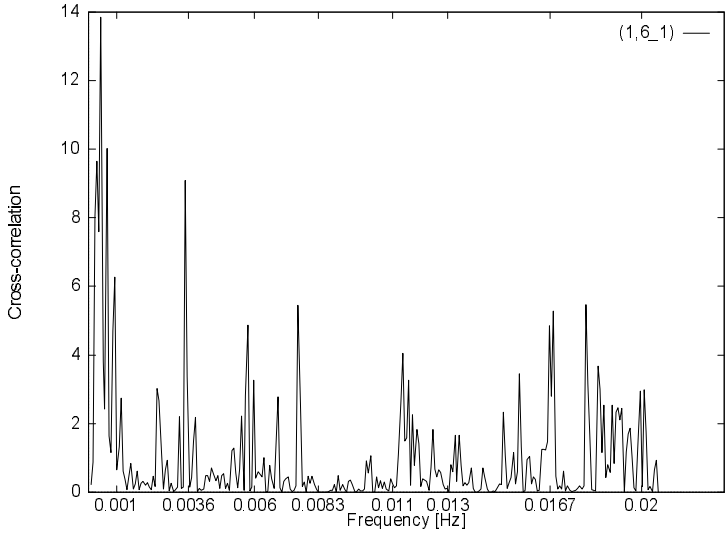

Figure C.2: Cross-correlation: Data sets No. 1 and 6_1.

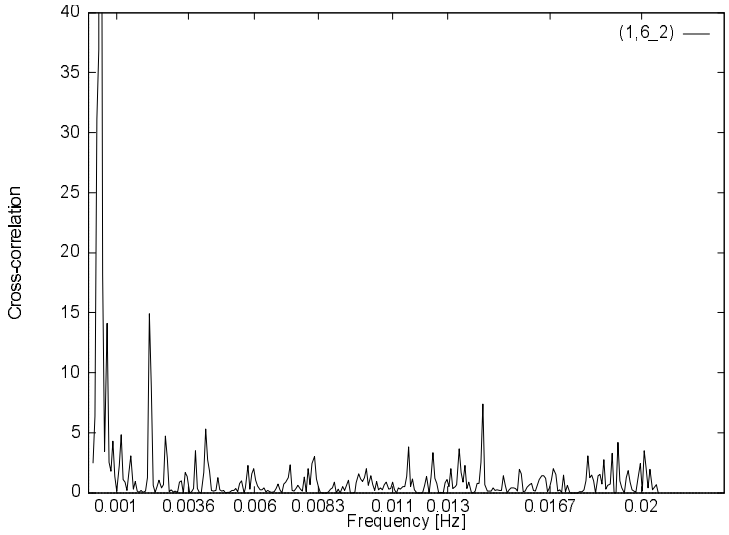

Figure C.3: Cross-correlation: Data sets No. 1 and 6_2.

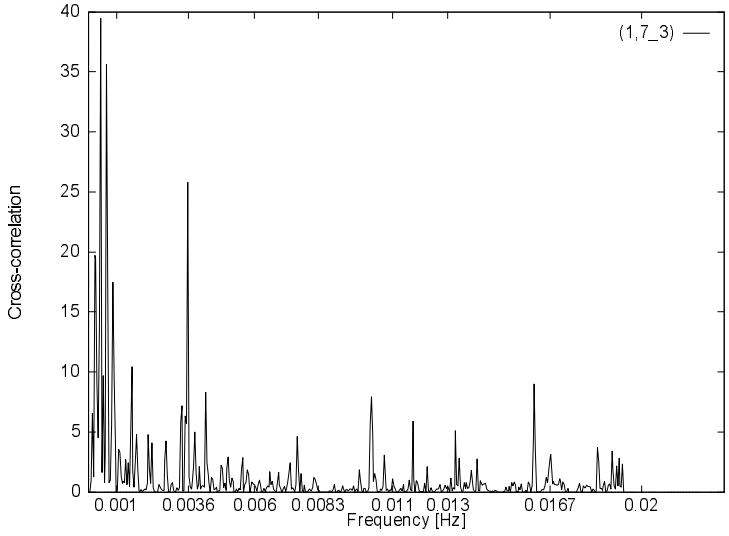

Figure C.4: Cross-correlation: Data sets No. 1 and 7_3.

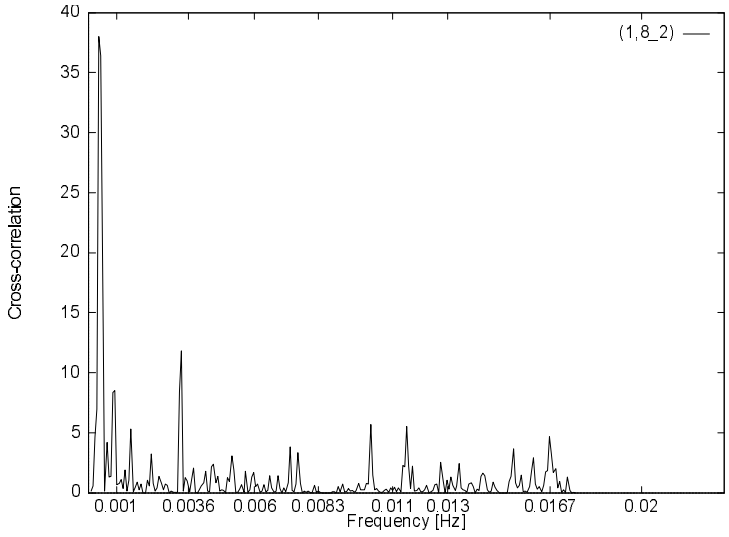

Figure C.5: Cross-correlation: Data sets No. 1 and 8_2.

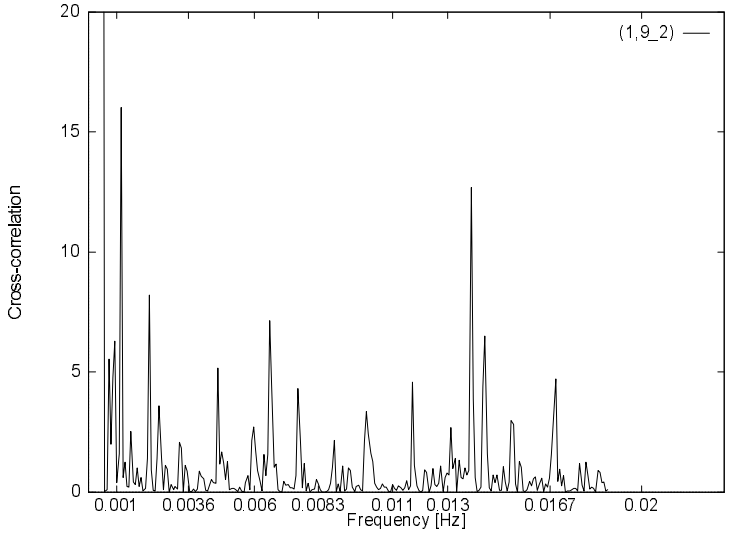

Figure C.6: Cross-correlation: Data sets No. 1and 9_2.

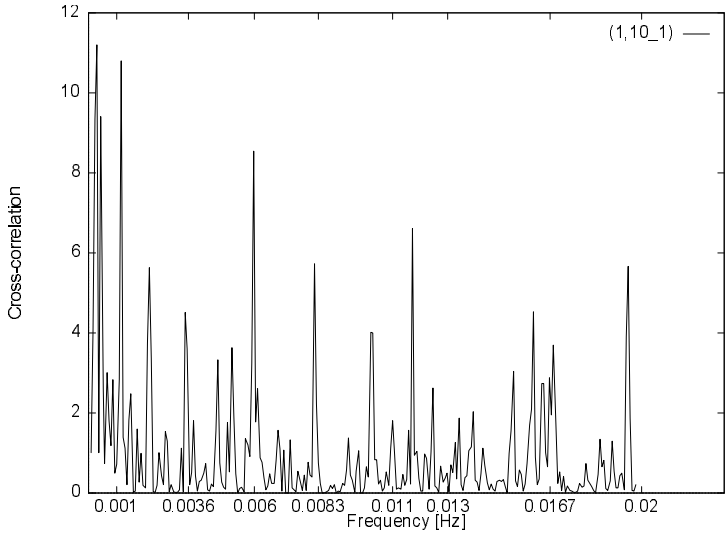

Figure C.7: Cross-correlation: Data sets No. 1 and 10_1.

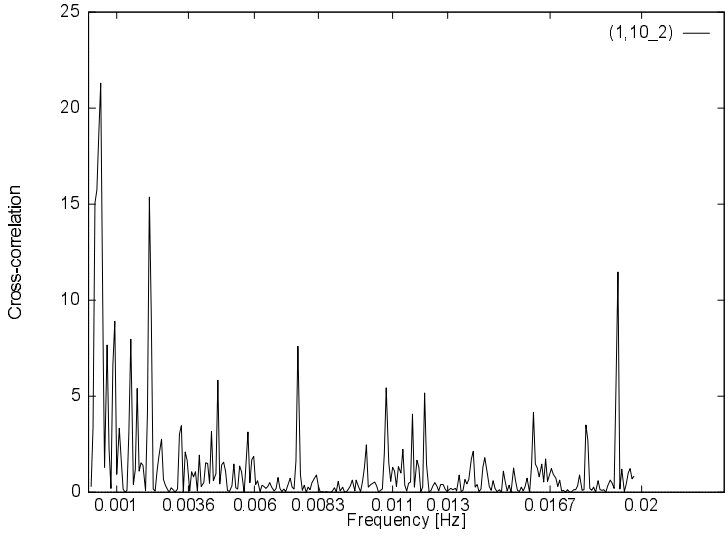

Figure C.8: Cross-correlation: Data sets No. 1 and 10_2.

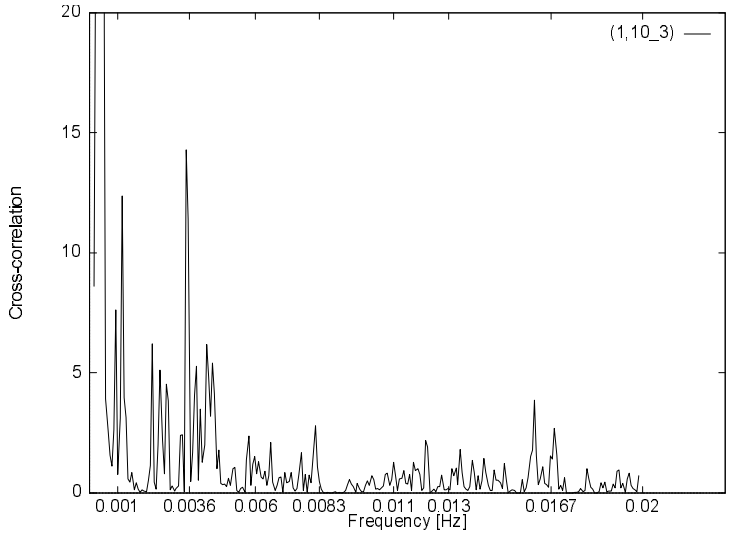

Figure C.9: Cross-correlation: Data sets No. 1 and 10_3.

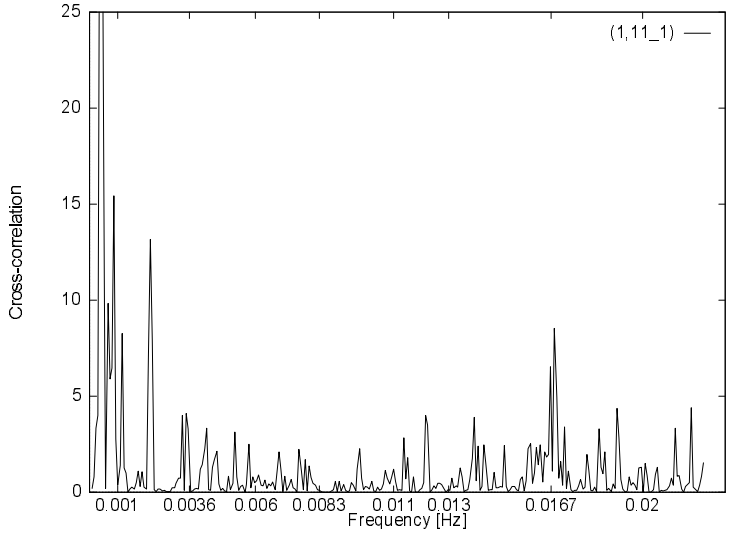

Figure C.10: Cross-correlation: Data sets No. 1 and 11_1.

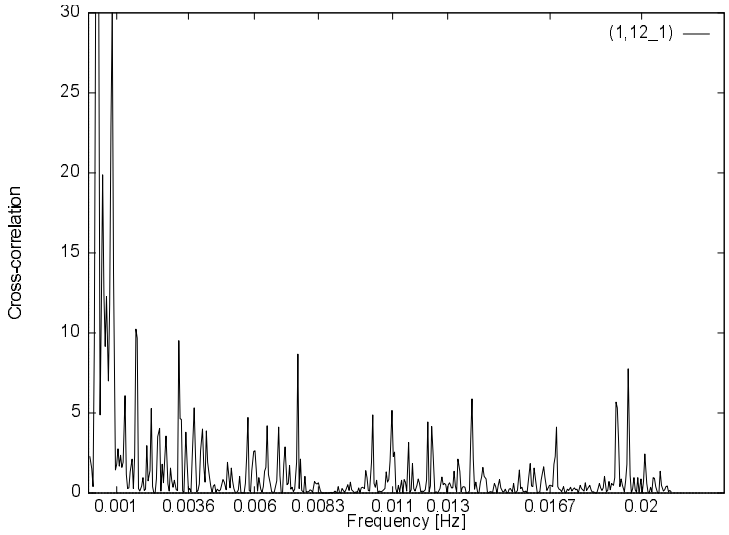

Figure C.11: Cross-correlation: Data sets No. 1 and 12_1.

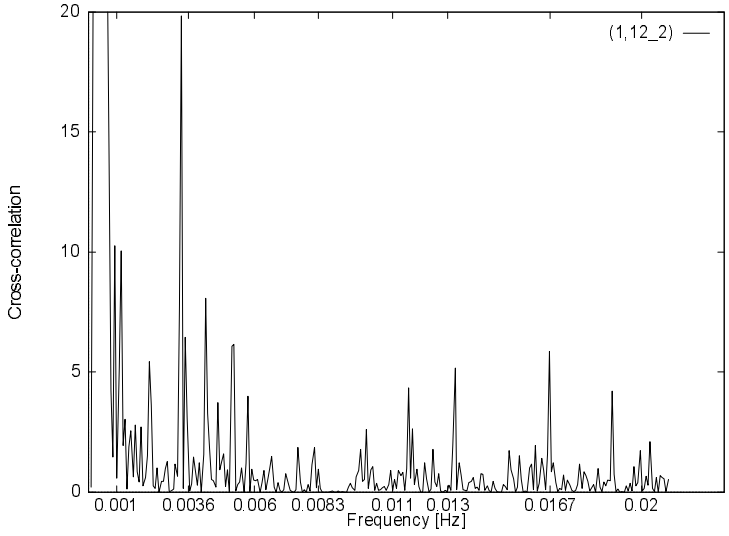

Figure C.12: Cross-correlation: Data sets No. 1 and 12_2.

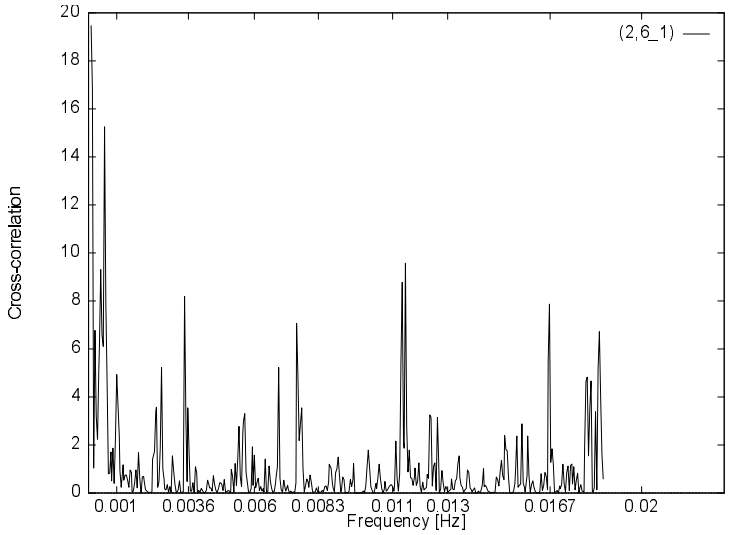

Figure C.13: Cross-correlation: Data sets No. 2 and 6_1.

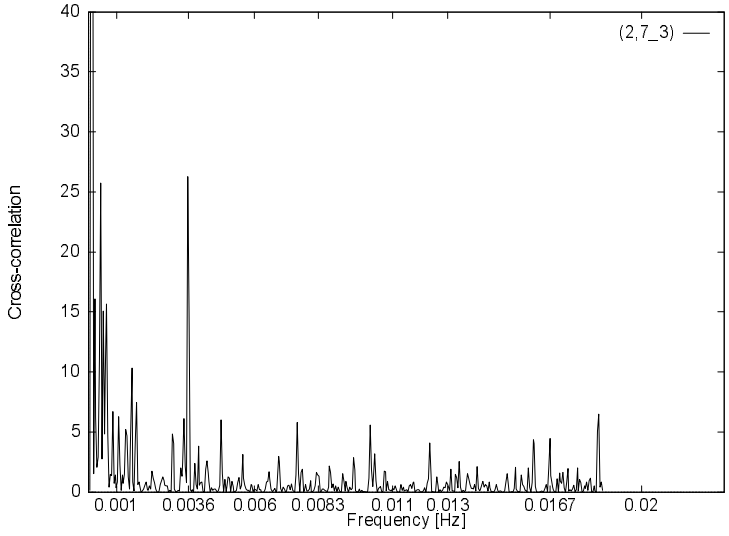

Figure C.14: Cross-correlation: Data sets No. 2 and 7_3.

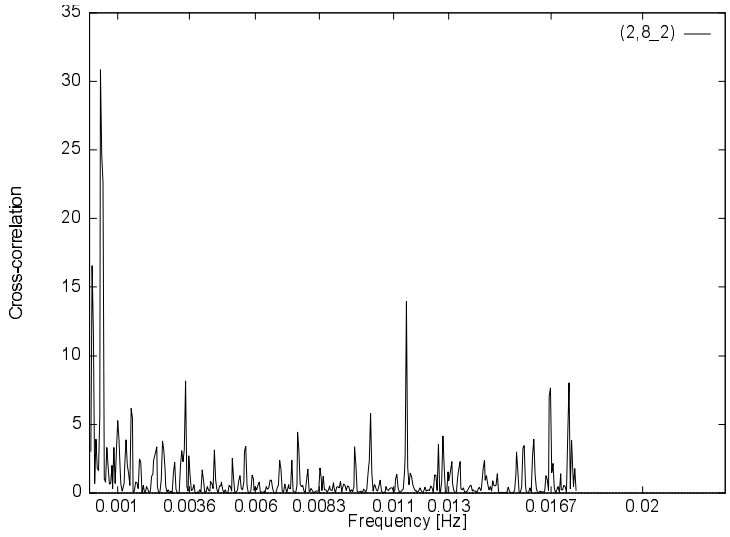

Figure C.15: Cross-correlation: Data sets No. 2 and 8_2.

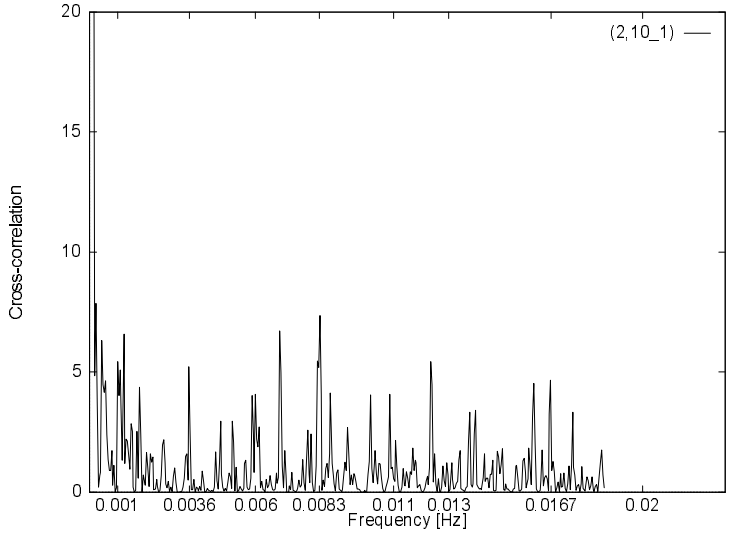

Figure C.16: Cross-correlation: Data sets No. 2 and 10_1.

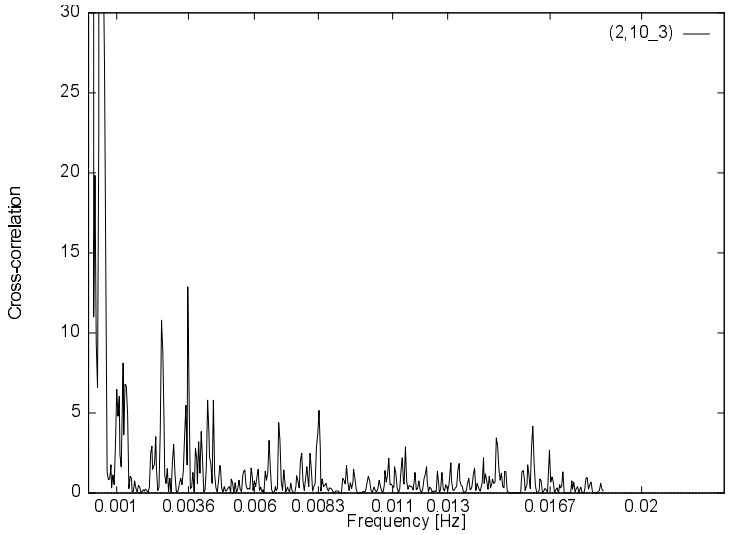

Figure C.17: Cross-correlation: Data sets No. 2 and 10_3.

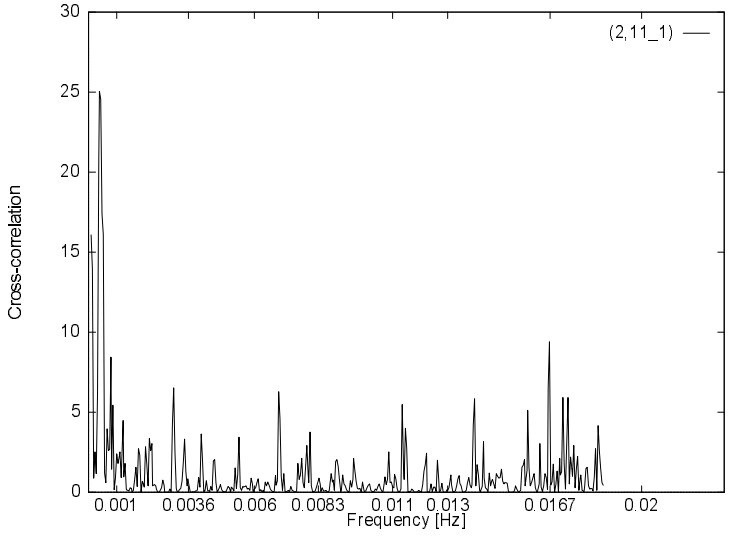

Figure C.18: Cross-correlation: Data sets No. 2 and 11_1.

Appendix D

Extended abstract in Slovene (Razširjeni povzetek v slovenščini)

D.1 Uvod

Pulzar v meglici Rakovici (kataloški oznaki objekta: PSR(B)0531+21, J0534+2200) je kompaktni ostanek zvezde po eksploziji supernove, ki se je zgodila leta 1054. Leta 1942 je Baade povezal zvezdo v sredini meglice (pulzar) z meglico. Kmalu po odkritju pulzarjev leta 1967 so ugotovili, da le-ti sodijo med nevtronske zvezde. Pulzar v meglici Rakovici je mlad pulzar s kratko periodo pulzacij (33 milisekund). Njegove optične pulze so odkrili leta 1969 v Cambridgu, leto prej pa je bil pulzar detektiran v radijskih valovih na observatoriju Jodrell Bank v Veliki Britaniji (Glendenning 1997 [24] in tam navedene reference). Kasneje so na ameriškem observatoriju Lick s posebno televizijsko (stroboskopsko) metodo in 3-metrskim teleskopom posneli maksimum in minimum pulzacij, vendar pa kasneje ni zaslediti poročil o stroboskopskih opazovanjih. Obravnavani pulzar sodi med tiste maloštevilne pulzarje, ki jih lahko opazujemo na širokem pasu valovnih dolžin od nizkofrekvenčnih radijskih valov do visokoenergijskega sevanja γ (Smith 1977 [50]).

Astronomi so pulzarju v meglici Rakovici od njegovega odkritja naprej namenjali zelo veliko opazovalnega časa, posebej še natančnemu merjenju časov prihodov posameznih pulzov (v radijskem), ter opazovanju stabilnosti (ali možne modulacije) njegovega energijskega fluksa (v različnih delih elektromagnetnega spektra). Razloge za možno modulacijo pulzacij lahko razdelimo na *zunanje* in *notranje*. Prvi so posledica fizikalnih procesov, katerim so pulzi

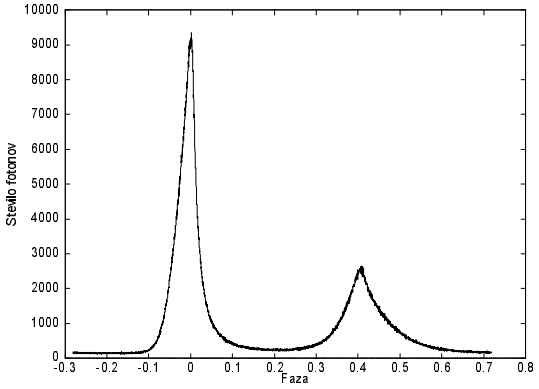

Slika D.1: Optični pulz pulzarja v meglici Rakovici, izmerjen s Hubblovim vesoljskim teleskopom (Percival et al. 1993 [41]). Na abscisni osi je faza (1=2π), na ordinatni pa število detektiranih fotonov. Pulz je sestavljen iz glavnega pulza in nižjega subpulza.

vzpostavljeni na svoji poti od emisijskega področja do opazovalca. Drugi so povezani s fizikalnimi procesi na samem emisijskem področju ali s značilnostmi nevtronske zvezde. Med slednje sodi tudi prosta precesija. Pričakovali bi namreč, da bo vrteča se sploščena nevtronska zvezda, podobno kot Zemlja, prosto precedirala. Oba objekta imata v grobem podobno strukturo: trdno sredico, raztopljen plašč, ter trdno skorjo. Prosta precesija nevtronske zvezde naj bi se zadušila v približno tisoč letih (Alpar et al. 1984 [2]), zato so za detekcijo pojava posebej primerni mladi pulzarji, kakršen je pulzar v meglici Rakovici. Za počasi rotirajoče nevtronske zvezde lahko prosto precesijo obravnavamo nerelativistično (Thorne&Gürsel 1983 [56]). Tako s klasično zvezo za kotno hitrost precesije (Goldstein 1980 [21]) s pomočjo Maclaurinove formule (Lang 1978 [33]) dobimo oceno okrog 100 sekund za periodo proste precesije pulzarja v meglici Rakovici (Galičič 1995 [20]). Meritev prosto-precesijske periode bi bila posebnega pomena za teorijo notranjosti nevtronskih zvezd, saj bi iz nabora modelov snovi v notranjosti nevtronske zvezde (enačba stanja snovi) izločila najverjetnejšega. Zato astronomi vse od odkritja pulzarjev obravnavajo vprašanje proste precesije nevtronskih zvezd ter pogosto poskušajo kot prosto-precesijske razložiti opažene različne (kvazi)periodičnosti v energijskem fluksu pulzarja v meglici Rakovici, predvsem na daljših časovnih skalah.

Sistem za stroboskopsko opazovanje pulzarja v meglici Rakovici, ki smo ga razvili, je primeren za opazovanje variabilnosti pulzarjevih optičnih pulzacij na časovnih skalah od približno 40 sekund do nekaj minut. Z njim smo

nameravali preiskati omenjeni časovni interval in ugotoviti, ali so pulzacije periodično modulirane, in ali perioda modulacije, če le-ta obstaja, ustreza zgoraj omenjeni oceni za periodo proste precesije.

Prva opazovanja pulzarja v meglici Rakovici s stroboskopskim sistemom smo pridobili leta 1994 in 1995 na italijanskem 1.82m teleskopu (Osservatorio Astronomico di Padova e Asiago). Ta opazovanja in opazovanja pulzarja v meglici Rakovici, ki so jih leta 1991 opravili s hitrim fotometrom Hubblovega vesoljskega teleskopa, so pokazala modulacijo pulzarjevih optičnih pulzacij s periodo 60 sekund in amplitudo 0,0065 magnitude. Analiza opazovanj je podrobno obdelana v magistrskem delu (Galičič 1995 [20]), rezultati so objavljeni v članku (Čadež and Galičič 1996 [11]). Z opazovanji v letih 1996 do 1998 smo želeli pridobiti podatke z boljšim razmerjem signala proti šumu, potrditi obstoj 60-sekundne modulacije z večjo signifikantnostjo, ter spremljati periodo te modulacije preko več let. Če je modulacija posledica proste precesije, katere perioda je odvisna od rotacijske periode pulzarja, bi namreč morali opaziti časovno spreminjanje prosto-precesijske periode, odvisno od časovnega spreminjanja rotacijske periode.

V osrednjem delu tega teksta so nekoliko podrobneje predstavljeni stroboskopska opazovalna metoda in stroboskopski podatki, analiza podatkov, ki obsega Fourierovo metodo z Lombovim periodogramom, navzkrižne korelacije Fourierovih spektrov, ter metodo zlaganja po epohah. Zanimalo nas je tudi, če je nivo šuma v pulzarjevem signalu večji kot nivoji šuma v signalih drugih zvezd na posnetkih. V zaključku so povzeti rezultati in dosežki doktorskega dela, ter nakazane možnosti za prihodnjo uporabo stroboskopske metode opazovanja v pulzarski astronomiji.

D.2 Opazovanja in rezultati

V osrednjem delu tega teksta bo na kratko opisana stroboskopska metoda opazovanja, predstavljeni bodo podatki in njihova analiza. Na koncu bodo podani rezultati analize.

D.2.1 Stroboskopska opazovalna metoda

Začetki izdelave stroboskopske opreme za opazovanje pulzarja v meglici Rakovici segajo v leto 1991, ko smo s prvim preprostim stroboskopom in 25-cm teleskopom Astronomsko-geofizikalnega observatorija Golovec izmerili rotacijsko frekvenco pulzarja (Galičič 1991 [19]). Opazovalni sistem smo v sledečih letih dogradili in izboljšali. Sedaj je sestavljen iz sledečih komponent: vetrnica z elektromotorčkom in pripadajočo elektroniko, funkcijski generator

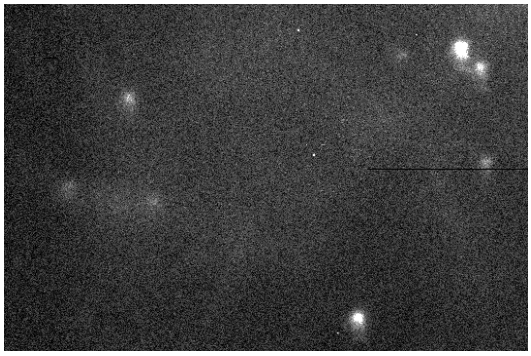

Slika D.2: Pulzar je "prižgan" (najsvetlejša zvezda v zgornjem desnem vogalu slike). Posnetek je bil narejen v noči 23/24 januar 1998 v Cananei. Ekspozicijski čas je bil 30 sekund.

(Hewlett-Packardov Function Generator HP3325A), časovna referenca (GPS sprejemnik podjetja TrueTime, model XL-DC 151-600-110), osebni računalnik. Kot detektor svetlobe služi kamera CCD (Wright Instruments, model EEVP86231, 385x578 slikovnih elementov), pri kateri za shranjevanje posnetkov rabimo osebni računalnik. Pri stroboskopskem opazovanju svetloba s teleskopa ne pade direktno na čip kamere CCD, pač pa je med teleskopom in kamero vetrnica, ki se vrti s frekvenco, enako frekvenci prihajanja pulzarjevih pulzov. Vetrnica je tenek kovinski krog z radialnimi izrezi. Razmerje središčnih kotov izrezanega proti neizrezanemu delu je 1:9, tako da izrezani del predstavlja 10% periode. To razmerje je izbrano v skladu z dolžino glavnega pulza opazovanega pulzarja, saj svetlobe ne želimo zbirati v času izven glavnega pulza, ker je tedaj intenziteta pulzirane svetlobe manjša ali celo enaka nič. Ker se pulzarjeva frekvenca s časom spreminja, moramo med samim opazovanjem to upoštevati, če želimo, da bo na vseh posnetkih pulzar enako svetel. Ustrezne popravke frekvence pretvorimo v popravke faze, ki jih naračunamo pred opazovanjem, med opazovanjem pa jih v enakomernih časovnih intervalih preko računalnika pošiljamo funkcijskemu generatorju.

Glavne prednosti stroboskopske opazovalne metode v primerjavi z direktnim opazovanjem pulzarja so sledeče:

1. Na ta način pulzacije zares *vidimo*, saj s spreminjanjem faze vrtenja vetrnice lahko pulzar "prižgemo" ali "ugasnemo", kot to kažeta sliki D.2 in D.3.

2. S pomočjo stroboskopa lahko opazujemo amplitudno in fazno modulacijo pulzacij.

3. Signal pulzarjevih pulzacij je ojačan glede na obdajajoče ga ozadje.

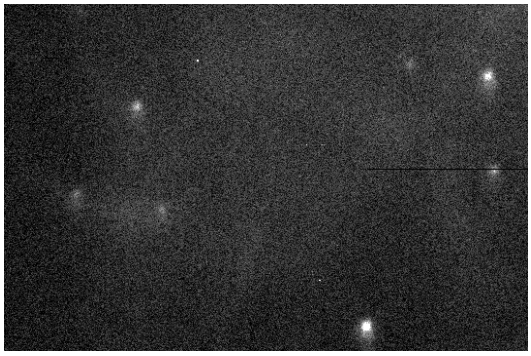

Slika D.3: Pulzar je "ugasnjen" (primerjaj zgornji desni vogal slike s prejšnjo sliko). Posnetek je bil narejen v noči 23/24 januar 1998 v Cananei. Ekspozicijski čas je bil 30 sekund.

Na osnovi stroboskopskega posnetka lahko ocenimo, da je razmerje signala proti šumu na posnetku CCD za pulzar dobrih dvakrat večje, če opazujemo s stroboskopom, kot če bi opazovali brez njega.

Pri stroboskopskem opazovanju pulzarjev moramo imeti zelo natančno uro, s katero sledimo natančni pulzarjevi notranji uri, ki temelji na njegovem vrtenju. Da s frekvenco vetrnice sledimo pulzarjevi frekvenci (ker spremembe frekvence pretvorimo v spremembe faze, smo za označitev tega postopka izbrali izraz *popravljanje faze*), moramo upoštevati naslednje glavne dejavnike, ki vplivajo na pulzarjevo frekvenco, kakršno izmerimo v observatoriju: Dopplerjev efekt zaradi kroženja Zemlje okrog Sonca in zaradi njenega vrtenja okrog lastne osi; upočasnjevanje pulzarjevega vrtenja s časom; relativistično zakasnitev svetlobe v gravitacijskem polju Sonca (Bell 1997 [5]). Merjenje časov prihodov pulzov (angl. *pulsar timing*) upošteva naštete dejavnike. V glavnem čase prihodov pulzov merijo z radijskimi teleskopi. Za pulzar v meglici Rakovici to počnejo na angleškem observatoriju Jodrell Bank, od koder pulzarski astronomi dobivamo efemeride tega objekta (Lyne et al. 1994-1997 [17]), to je vrednosti pulzarjeve frekvence in njenega časovnega odvoda za določene trenutke, ter nekatere druge podatke. Te vrednosti so izhodišče pri računanju faznih popravkov (s pomočjo računalniški program Bartim, ki izvira z ameriške univerze MIT).

Fazni profil pulza smo definirali kot krivuljo, ki kaže spreminjanje pulzarjeve magnitude glede na fazno razliko med pulzarjem in vetrnico, ko se vrtita z enako frekvenco. Pri fazni razliki nič je pulzar najsvetlejši. Fazni profil pulza lahko simuliramo, če poznamo funkcijo, ki opisuje intenziteto svetlobe preko pulzarjeve periode (obliko pulza), ter funkcijo, ki opisuje,

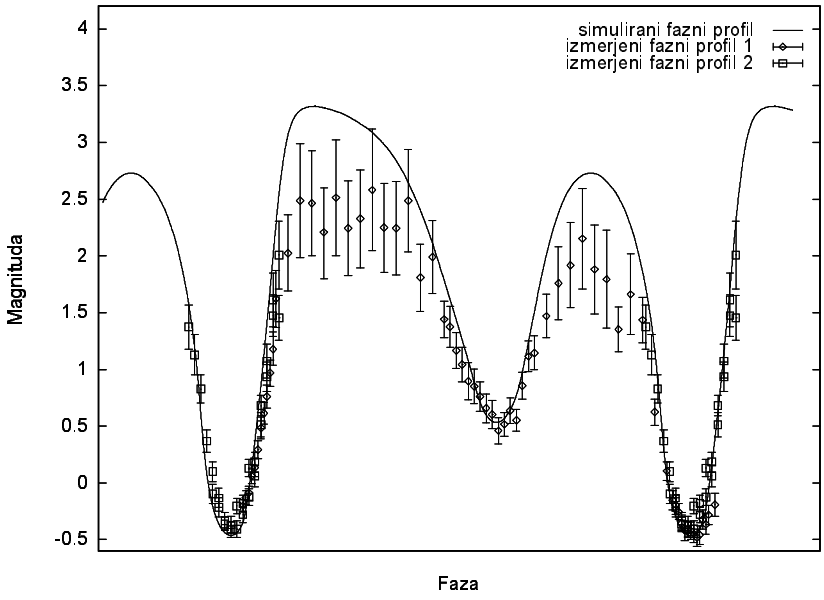

Slika D.4: Simulirani (zvezna krivulja) in izmerjeni (točke) fazni profil pulzarja v meglici Rakovici. Fazni profil je bil izmerjen v noči 23/24 januar 1998 in njegov del (preko glavnega pulza) še dvakrat v noči 24/25 januar 1998. Ti dve meritvi (točke-kvadratki) sta narisani preko obeh minimumov na sliki. (Ker je na ordinatni osi označena magnituda, minimum na sliki ustreza maksimumu energijskega fluksa, torej glavnemu vrhu pulza.) Fazna razlika med obema minimumoma ustreza eni periodi (2π).

kolikšen del periode vetrnica odpira pot svetlobe do kamere CCD (oblika okna). Izmerimo pa fazni profil tako, da posnamemo serijo slik, pri čemer med dvema zaporednima posnetkoma spremenimo fazno razliko za izbrano vrednost. Slika D.4 prikazuje simulirani (zvezna krivulja) in izmerjeni (točke z merskimi napakami) fazni profil pulzarja v meglici Rakovici. Narisana je magnituda pulzarja v odvisnosti od fazne razlike. Najglobja minimuma na sliki ustrezata glavnemu pulzu (pulzar je najsvetlejši), med njima je razlika v fazi 2π, vmesni lokalni minimum pa subpulzu.

Stroboskopsko opremo smo v petih letih opazovanj trikrat testirali. Namen pri tem je bilo ugotoviti časovno natančnost sistema, ter preiskati, ali znotraj sistema morda ne prihaja do generiranja sporadičnih periodičnih signalov. Nekatere teste smo opravili v merilnem laboratoriju Hermes Plus v Ljubljani (podjetje, ki v Sloveniji zastopa ameriško podjetje Hewlett-Packard), preostale pa v našem laboratoriju. Noben od testov ni odkril pomanjkljivosti opreme, ki bi lahko vplivale na stroboskopska merjenja.

D.2.2 Predstavitev in analiza podatkov

V tabeli 11 so zbrana stroboskopska opazovanja, ki smo jih v letih 1994 do 1998 pridobili na 1.22m (postavljen nad Asiagom) in 1.82m (postavljen na hribu Cima Ekar (CE v tabeli), nekaj kilometrov stran od Asiaga) teleskopih italijanskega observatorija Asiago (Osservatorio Astronomico di Padova e Asiago), ter v letu 1998 na 2.12m teleskopu mehiškega observatorija Guillermo Haro v Cananei. Zaporedni stolpci v tabeli 11 (od leve proti desni) vsebujejo: zaporedno številko opazovanja, dvojni datum opazovalne noči, observatorij, premer teleskopovega zrcala v metrih, ekspozicijski čas posnetkov v sekundah, ter "seeing"[1] v ločnih sekundah.

Št.	Datum opazovanja	Observatorij	$D[m]$	$T_{eksp}[s]$	Seeing["]
1	12/13 December 1994	Asiago(CE)	1.82	12	2.8
2	19/20 December 1995	Asiago(CE)	1.82	15	3.0
3	17/18 December 1996	Asiago(CE)	1.82	14.5	3.1
4	21/22 February 1997	Asiago	1.22	30	
5	22/23 February 1997	Asiago	1.22	15	
6	26/27 February 1997	Asiago	1.22	14.5	
7	27/28 February 1997	Asiago	1.22	14.5	
8	6/7 December 1997	Asiago	1.22	15	
9	7/8 December 1997	Asiago	1.22	15	
10	22/23 January 1998	Cananea	2.12	15.5	2.4
11	23/24 January 1998	Cananea	2.12	12.5	2.3
12	24/25 January 1998	Cananea	2.12	13.9	2.3
13	25/26 January 1998	Cananea	2.12	16.1	2.2

Tabela 11. Pregled podatkov.

Na sliki D.5 so podatki prikazani grafično, kot krivulje, ki prikazujejo magnitudo pulzarja preko noči, pri čemer je na abscisni osi označena zaporedna številka posnetka. Krivulje so označene s številkami, ki ustrezajo številkam v prvem stolpcu tabele 11. Vsaka višja krivulja je premaknjena za konstantno vrednost, tako da so lahko vse prikazane na isti sliki. Za skalo pa služita oznaki "0" in "5" magnitud na ordinatni osi. Na sliki lahko vidimo, da so spodnje tri krivulje, od katerih prvi dve sodita v skupino t.i. starih podatkov, izrazito mirnejše od preostalih krivulj, kjer je šum večji.

Podatke smo analizirali na dva načina, pri čemer je bil namen analize poiskati periodičnosti v izmerjenih krivuljah "magnituda (m) v odvisnosti od časa". Prvi način sodi v Fourierovo analizo, posebnost uporabljenega

[1]Uporabljen je angleški izraz, ker še nimamo kratkega slovenskega izraza, ki bi enakovredno opisal to, kar pove angleški izraz. Slovensko bi lahko seeing opisali kot "razmazanost slike zvezde zaradi atmosfere".

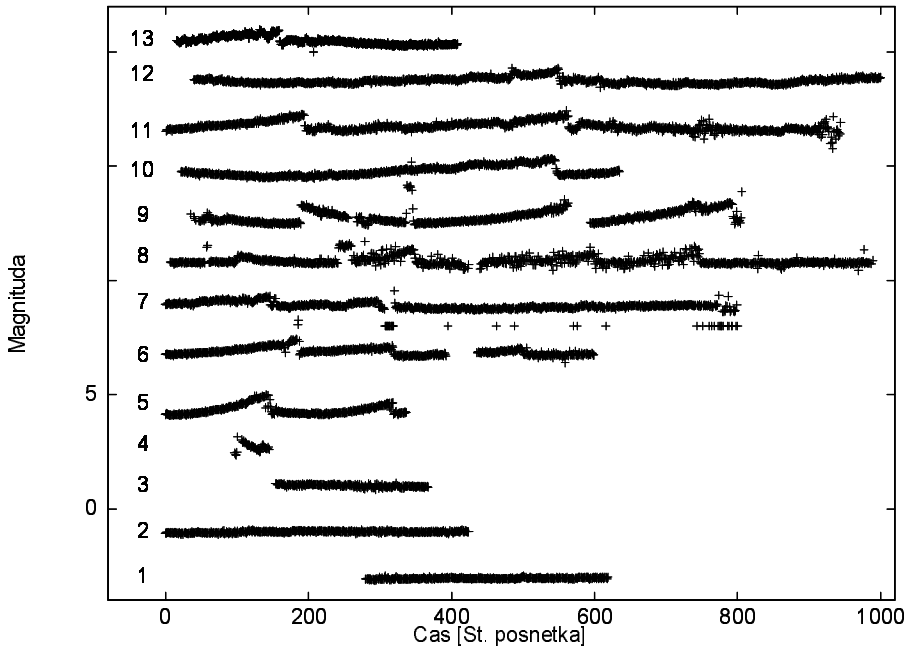

Slika D.5: Potek pulzarjeve magnitude za opazovanja, označena s številkami od 1 do 13 v tabeli 11. Da so vse krivulje narisane na eni sliki, so premaknjene za ustrezne konstantne vrednosti. Vrednosti "0" in "5" na ordinatni skali služita kot skala. Čas je merjen z zaporedno številka posnetka, zato posamezna opazovanja lahko primerjamo po številu posnetkov, po trajanju pa jih natančno ne moremo. (Tipično pa kakih dvesto zaporednih slik ustreza okrog uri in pol opazovanj.) Ekspozicijski časi so zapisani v tabeli 11.

Lombovega algoritma (Press et al. 1992 [45]) pa je v tem, da je izdelan posebej za primer, ko časovni razmiki med zaporednimi podatki niso enaki. Pri opazovanjih s kamero CCD je to neizogibno. Vsako meritev predstavimo kot N merskih točk m_i, $i = 1...N$ (podanih ob časih t_i), katerih povprečna vrednost in standardna deviacija sta $\overline{m} = \frac{1}{N}\sum_i m_i$ in $\sigma^2 = \frac{1}{N-1}\sum_i (m_i - \overline{m})^2$. Rezultat spektralne analize je periodogram, tj. spektralna moč $P_N(\omega)$ v odvisnosti od frekvence $\omega = 2\pi\nu, \nu > 0$,

$$P_N(\omega) \equiv \frac{1}{2}\left(\frac{[\sum_i (m_i - \overline{m})\cos\omega(t_i - \tau)]^2}{\sum_i \cos^2\omega(t_i - \tau)} + \frac{[\sum_i (m_i - \overline{m})\sin\omega(t_i - \tau)]^2}{\sum_i \sin^2\omega(t_i - \tau)}\right)$$

Konstanta τ je definirana kot

$$\tan(2\omega\tau) = \frac{\sum_i \sin(2\omega t_i)}{\sum_i \cos(2\omega t_i)}$$

S tako izbranim τ je $P_N(\omega)$ popolnoma neodvisen od tega, če katerikoli t_i premaknemo za poljubno konstantno vrednost (Press et al. 1992 [45]). Na ordinatni osi spektrov, ki so prikazani spodaj, je podana spektralna amplituda

$$A(\omega) = \sqrt{P_N(\omega)}$$

v magnitudah. Ker so meritve posamezne noči, kot lahko vidimo na sliki D.5, po večkrat prekinjene, ali pa mestoma še posebej spremenljive, smo za analizo izbrali dele vsake od meritev. To so nizi zaporednih slik, znotraj katerih ni večjih skokov v magnitudi in jih je skupaj 28. Od teh je na slikah D.6 in D.7 prikazanih le 13 spektrov, kateri imajo povprečni šum pod 0.004 magnitude. Ta meja je bila izbrana glede na amplitudo 60-sekundne modulacije, katero je pokazala analiza t.i. starih podatkov.

Za vsakega od teh spektrov smo pogledali, če ima vrh pri frekvenci 1/60s ter določili signifikantnost vrha s pomočjo Gaussovega verjetnostnega integrala (Bronštejn in Semendljajev 1980 [7]). Izraziti vrhovi so opazni predvsem v spektrih starih stroboskopskih podatkov, označenih s številkama 1 in 2 v tabeli 11 (enako sta označena tudi ustrezna spektra na sliki D.6), ter v spektru podatkov, pridobljenih s Hubblovim vesoljskim teleskopom. Verjetnosti, da ti trije vrhovi niso naključni, so zaporedoma 96%, 97% in 83%. Na njihovi osnovi smo določili frekvenco in amplitudo modulacije: $\nu_r = (0.01679 \pm 0.00016)Hz$, $A_{mod} = (0.0055 \pm 0.0015)$ *magnitude*.

Zanimalo nas je tudi, ali so amplitude v spektrih v povprečju porazdeljene Gaussovo. Opazili smo rahla odstopanja od Gaussove porazdelitve, predvsem v repih (pri večjih amplitudah), kar pa je povezano tudi z manjšim številom večjih amplitud. Pokazalo pa se je, da se porazdelitev točk v repih nekoliko umiri, če izločimo amplitude pri nizkih frekvencah <0.003Hz. To je

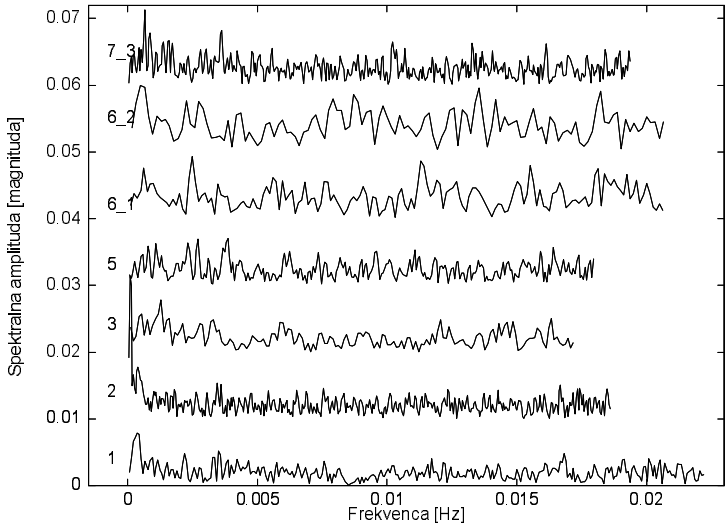

Slika D.6: Lombovi periodogrami sedmih nizov podatkov (od trinajstih, ki imajo nivo šuma pod 0.004 magnitude). Na levi strani vsake krivulje je oznaka ustreznega niza podatkov. Fourierova amplituda je prikazana v magnitudah. Da so vsi spektri lahko prikazani na eni sliki, je vsak premaknjen za ustrezno konstanto. Vrednosti "0" in "0.01" na ordinati služita kot skala.

potrdilo našo staro domnevo, da je prevelik (večji, kot bi pričakovali) šum v pulzarjevi magnitudi morda povezan z atmosferskimi scintilacijami, ki najverjetneje sodijo v skupino pojavov, ki jih lahko opišemo kot šum oblike "1/f", kjer f označuje frekvenco v spektru. Žal imamo premalo meritev, da bi lahko primerjali porazdelitev amplitud pri izbrani frekvenci (npr. 1/60s) s porazdelitvami amplitud pri drugih posameznih frekvencah.

Nazadnje smo spektre narisali še enkrat tako, da so si sledili glede na zaporedni datum, ob katerem je bilo opazovanje opravljeno. Na ta način smo želeli primerjati natančno lego vrha pri frekvenci 1/60s ter njegovo eventualno pomikanje v odvisnosti od časa. Vrhovi v spektrih starih podatkov so razvrščeni tako, da je vrh, ki ustreza kasnejšemu opazovanju, pri nižji frekvenci. Žal pa v preostalih (kasnejših) opazovanjih ni izrazitih vrhov pri tej frekvenci.

Spektre smo nato paroma navzkrižno korelirali. S tem smo želeli preveriti, ali signala, katerima pripadata spektra v paru, predstavljata dva statistično neodvisna Gaussova šuma, ali pa morda vsebujeta skupno periodično komponento. S primerjavo vrednosti navzkrižno-korelacijske funkcije pri izbrani frekvenci (1/60s) s povprečno vrednostjo navzkrižno-korelacijske funkcije, lahko izračunamo verjetnost, da se je tako visok vrh pojavil slučajno. V

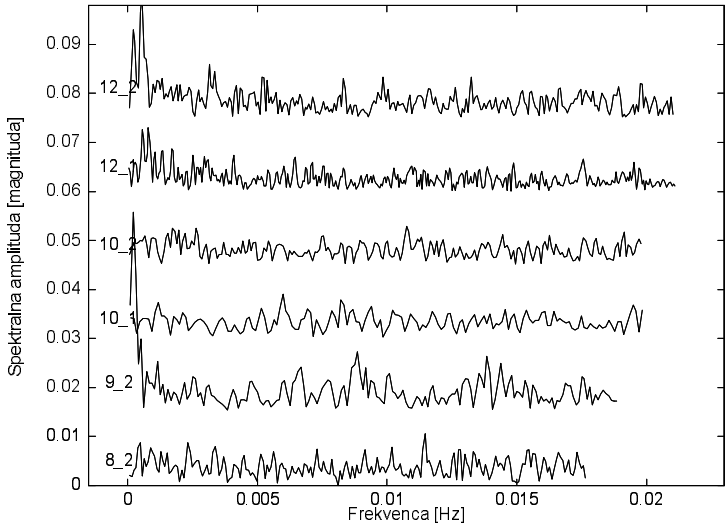

Slika D.7: Lombovi periodogrami naslednjih šestih nizov podatkov (od trinajstih, ki imajo nivo šuma pod 0.004 magnitude). Na levi strani vsake krivulje je oznaka ustreznega niza podatkov. Fourierova amplituda je prikazana v magnitudah. Da so vsi spektri lahko prikazani na eni sliki, je vsak premaknjen za ustrezno konstanto. Vrednosti "0" in "0.01" na ordinati služita kot skala.

navzkrižno koreliranje smo vključili skupaj 17 spektrov, tako da je vseh korelacijskih funkcij 136. Kot primer navzkrižno-korelacijske funkcije je na sliki D.8 prikazana korelacija med spektroma, ki pripadata nizoma podatkov 1 in 0, kjer smo z "0" označili podatke, pridobljene s Hubblovim vesoljskim teleskopom. Pri 40 (29,4%) od 136 navzkrižno-korelacijskih funkcij smo opazili vrh pri frekvenci 1/60s. Pri posameznih korelacijah je verjetnost, da je vrh slučajen, precej pod odstotkom.

Druga metoda za iskanje periodičnosti v podatkih je metoda *zlaganja podatkov po epohah*. Ta metoda se posebej uporablja v primerih podatkov s slabim razmerjem signala proti šumu (Larsson 1996 [34]). Tu zaporednje N meritev m_i zložimo po izbrani testni periodi. Zložene podatke nato razvrstimo v M faznih razdelkov. Vsak fazni razdelek je tako širok $\frac{P}{M}$, če je P perioda, ki jo testiramo. Nato testiramo enakomernost faznih razdelkov, pri čemer predpostavimo, da podatek m_{kj} v j-tem faznem razdelku lahko zapišemo kot vsoto povprečja podatkov v tem razdelku μ_j in merske napake ϵ_{kj}, $m_{kj} = \mu_j + \epsilon_{kj}$. Pri tem predpostavimo, da so ϵ_{kj} Gaussovo porazdeljene neodvisne slučajne spremenljivke z identičnimi povprečnimi vrednostmi in standardnimi deviacijami. Ničelna hipoteza enakomernosti po prostoru $\mathcal{H}_o$ pravi, da so povprečne vrednosti v faznih razdelkih identične. Hipotezo

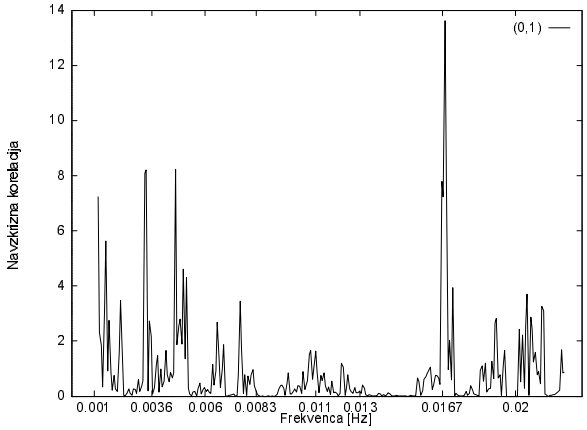

Slika D.8: Navzkrižno-korelacijska funkcija za spektra nizov podatkov "0" in "1".

zavrnemo, če so povprečja preveč razsuta, da bi jih jih lahko uskladili s privzetkom o enakomernosti. Spreminjanje povprečne vrednosti v faznih razdelkih torej razumemo kot močan dokaz, da je v podatkih skrita periodičnost. Kot merilo za verjetnost, da je v podatkih prisotna periodičnost, smo vzeli testno statistiko L, ki upošteva velikost vzorca (število točk N). Leta 1990 jo je predlagal Davis ([15]), ki trdi, da je ta statistika bolj občutljiva za periodičnosti kot pred tem predlagane testne statistike v metodi zlaganja po epohah. Definirana je kot

$$L = \frac{(N-M)\sum_{j=1}^{M} n_j(\overline{m_j} - \overline{m})^2}{(M-1)\sum_{j=1}^{M}\sum_{k=1}^{n_j} n_j(m_{kj} - \overline{m_j})^2}$$

kjer je n_j število točk v j-tem faznem binu. Statistika L je porazdeljena v skladu s porazdelitvijo F s prostostnima stopnjama $M-1$ in $N-M$ ([15]). Za primer podatkov, ki predstavljajo Gaussov šum, je pričakovana vrednost L enaka 1. Verjetnost, da je določena vrednost L v skladu s hipotezo $\mathcal{H}_o$, izračunamo s pomočjo nepopolne funkcije Beta.

Za vse nize podatkov smo testirali interval period od 55s do 65s z ustreznim razmakom med zaporednima testiranima periodama, ter interval period od 55s do 500s. Z izbiro prvega intervala smo podrobno pregledali okolico periode 60s. Z izbiro drugega intervala smo želeli primerjati vrednosti statistike L pri periodi 60s z ustreznimi vrednostmi na širokem intervalu period. Tako dobljene grafe "L v odvisnosti od testirane periode" smo med seboj zmnožili. Pričakovali smo, da se bo v zmnožku periodičnost, ki je morda prisotna v vseh ali v nekaj podatkihovnih nizih, pokazala kot izrazit vrh. Na sliki D.9 so prikazani produkti vrednosti L za vse podatke skupaj, samo za

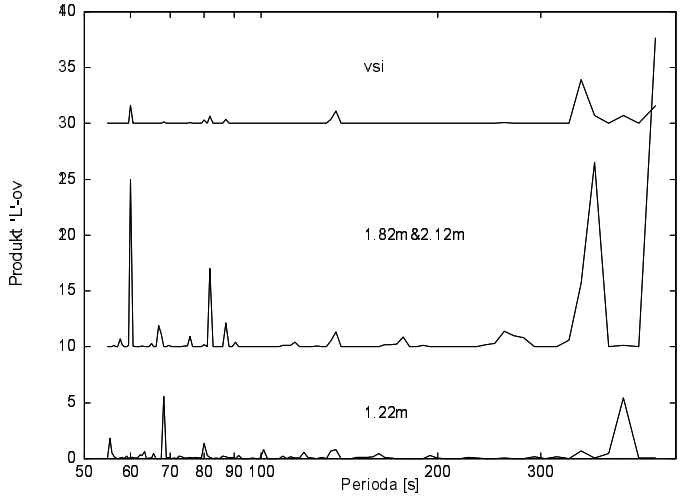

Slika D.9: Produkt statistik L posebej za podatke, pridobljene na 1.82m in 2.12m teleskopih (srednja krivulja), ter posebej za podatke, pridobljene na 1.22m teleskopu (spodnja krivulja). Zgornja krivulja prikazuje produkt statistik L za vse podatke skupaj.

podatke, pridobljene na 1.82m in 2.12m teleskopih, ter samo za podatke, pridobljene na 1.22m teleskopu. Slednji so obravnavani posebej, ker smo med opazovanjem imeli težave s teleskopovim zrcalom, kar je verjetno vplivalo na kredibilnost teh podatkov.

Na srednji krivulji lahko opazimo posebej izrazit vrh pri 60s. Na osnovi preiskovanja intervala period od 55s do 65s smo rezultate za vrednosti statistike L in pripadajoče verjetnosti za obstoj periodičnosti v podatkih, v okolici periode 60s, zbrali v tabelo in narisali na grafu. Pokazalo se je, da se prekrivajo vrednosti treh nizov podatkov, starih podatkov označenih z 1 in 2 ter novih podatkov s številko 13. Po metodi zlaganja po periodah dobljena modulacija ima torej periodo $P'_r = (60.0 \pm 0.3)s$ in amplitudo $\nu'_r = (0.01667 \pm 0.00009)s^{-1}$.

Vrednosti statistike L na intervalu period 55s do 500s smo primerjali tudi z vrednostmi statistike L (na istem intervalu) za magnitude sedmih drugih (naključno izbranih) zvezd na posnetkih. Tudi te vrednosti smo med seboj zmnožili ter s tem dobili primerjavo za srednjo krivuljo na sliki D.9, kjer je prav tako zmnoženih sedem funkcij. V produktu L-jev za sedem drugih zvezd pri nobeni periodi ni primerljivo tako visokega vrha, kot je na srednji krivulji slike D.9 vrh pri 60s.

Na koncu smo naredili še krajšo analizo primerjave nivoja šuma pulzarjeve magnitude v primerjavi z nivoji šuma magnitude po štirih drugih zvezd

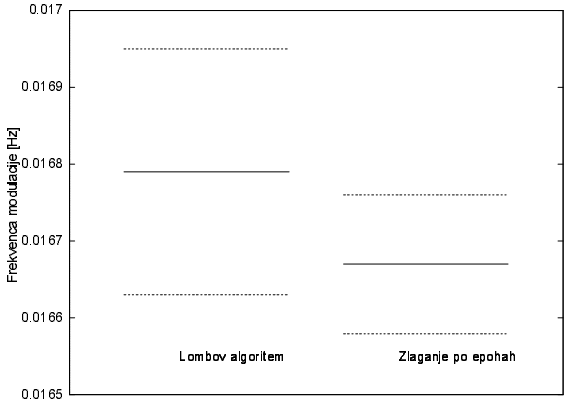

Slika D.10: Frekvenca modulacije: primerjava rezultatov metode Lombovega algoritma in metode zlaganja po epohah.

na posnetkih, za štiri opazovalne noči. Za vsako noč smo vzeli za pulzar in za primerjalne štiri zvezde enako dolg kos podatkov, jih Fourierovo transformirali ter za vsako zvezdo primerjali njen pričakovani šum (izračunan iz njene povprečne magnitude) z dejanskim šumom. Pokazalo se je, da je šum v pulzarjevi magnitudi vedno primerjalno večji od šuma v magnitudah drugih zvezd. Ocenili smo, da bi periodični signal, ki bi bil enako močan, kot je presežek šuma v pulzarjevem signalu glede na šum zvezde, ki je le 0,4 magnitude temnejša od pulazarja, imel amplitudo okrog 0,03 magnitude. Povzamemo lahko, da je pulzarjev signal tipično bolj zašumljen, kot bi pričakovali. To bi lahko pomenilo tudi, da modulacija pulzacij, če obstaja, nima ene diskretne frekvence. Jasnega odgovora o izvoru dodatnega šuma v pulzarjevem signalu še ne poznamo.

D.2.3 Rezultati

Rezultate obeh metod analize periodičnosti optičnih pulzacij pulzarja v meglici Rakovici lahko strnemo v dva grafa, ki sta prikazana na slikah D.10 in D.11.

Vidimo, da se frekvenci 60-s modulacije (slika D.10), dobljeni z obema metodama, ujemata v okviru napak. Enako velja za amplitudi modulacije (slika D.11). Pri tem pa moramo poudariti, da k rezultatu bistveno prispevajo predvsem t.i. stari podatki.

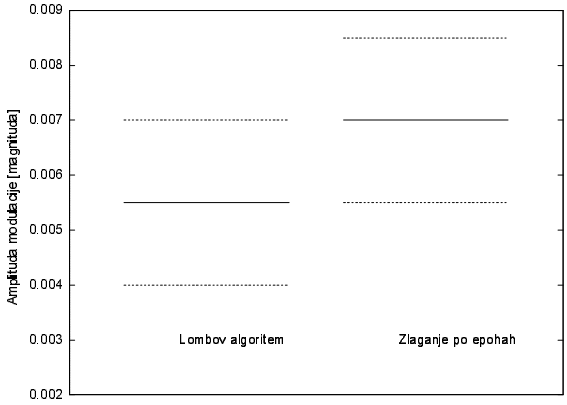

Slika D.11: Amplituda modulacije: primerjava rezultatov metode Lombovega algoritma in metode zlaganja po epohah.

D.3 Zaključek

Opisali smo večletno delo pri razvoju stroboskopskega opazovalnega sistema ter z njim pridobljena opazovanja pulzarja v meglici Rakovici na teleskopih v Italiji in v Mehiki. Podatke smo analizirali z dvema različnima metodama, Lombovim periodogramom (Fourierova analiza) ter metodo zlaganja po epohah. Znotraj napak dajeta obe metodi za iskanje periodičnosti v podatkih enake rezultate: Opazili smo modulacijo s periodo 60 sekund in amplitudo 0,006 magnitude. Fourierove spektre smo tudi paroma navzkrižno korelirali ter določili višino vrha pri frekvenci 1/60s v primerjavi s povprečno vrednostjo navzkrižno-korelacijske funkcije. Vrh pri frekvenci 1/60s smo opazili pri znatnem delu (29%) navzkrižno-korelacijskih funkcij. Ocenjujemo, da je zgornja meja za verjetnost, da je opažena 60-sekundna modulacija posledica slučajnih procesov, manjša od 3%, medtem ko analiza posameznih podatkovnih nizov (gl. poglavje 3.5 angleškega teksta) in navzkrižna korelacija parov spektrov (gl. poglavje 3.4 angleškega teksta) dajeta še dosti manjše verjetnosti (precej pod odstotek), da se je vrh pri 60 sekundah pojavil slučajno.

Metoda zlaganja po epohah je nakazala tudi možnost obstoja treh drugih periodičnosti (periode 82s, 134s, okrog 300s) v pulzarjevih podatkih, vendar pa le-teh nismo podrobneje obravnavali, saj jih Fourierova analiza ali navzkrižna korelacija spektrov nista potrdili.

Poudariti je treba, da so posebej izraziti vrhovi pri 60 sekundah opazni pri t.i. starih podatkih, tj. stroboskopskih podatkih iz let 1994 in 1995, ter podatkih Hubblovega vesoljskega teleskopa iz leta 1991. Drugi (novi) stro-

boskopski podatki iz let 1996 do 1998, ki imajo žal višji nivo šuma, k rezultatu ne prispevajo bistveno, vendar pa mu tudi ne nasprotujejo. Za nedvomno potrditev obstoja 60-sekundne modulacije optičnih pulzov pulzarja v meglici Rakovici bi bilo treba opazovanja ponoviti na katerem od največjih svetovnih teleskopov.

Opaženo 60-sekundno periodičnost smo poskusili razložiti s prosto precesijo rotirajoče sploščene nevtronske zvezde. Za razliko od večine pulzarskih astronomov, ki s prosto precesijo povezujejo dolge (kvazi)periodičnosti v energijskih fluksih pulzarjev pri različnih valovnih dolžinah, menimo, da bi morala biti perioda proste precesije pulzarja v meglici Rakovici, če ta pulazr prosto precedira, okrog ene minute. Model rotirajočih politrop, ki razloži tako 60-sekundno periodičnost pri obravnavanem pulzarju, kot 35-dnevni cikel objekta Her X-1, s prosto precesijo nevtronske zvezde, je opisan v članku (Čadež, Galičič and Calvani 1997 [12]).

Metoda stroboskopskega opazovanja nudi obilo novih možnosti za prihodnje delo na področju pulzarske astronomije. Tako bi lahko z večjim teleskopom v optimalnih opazovalnih razmerah dokončno potrdili obstoj 60-sekundne modulacije optičnih pulzov pulzarja v meglici Rakovici ter izvedli podobna opazovanja za nekatere druge pulzarje. S stroboskopom in spektroskopom se da posebej posneti spekter posameznih komponent pulza. Stroboskop nudi tudi možnost za (neodvisno) merjenje časov prihodov pulzov pri optičnih valovnih dolžinah. S pomočjo tega opazovalnega sistema bi bilo tudi možno izvesti pregled poznanih radijskih pulzarjev z namenom njihove detekcije v optičnem.